Development and Characterization of CuCr Composite Coatings & Thin Films as Contact Materials for Vacuum Interrupters

by

Animesh Koneru

A dissertation submitted in partial fulfillment
of the requirements for the degree of
Doctor Of Philosophy
(Mechanical Sciences and Engineering)
in the University of Michigan-Dearborn
2023

Doctoral Dissertation Committee:

Professor Ben Q Li, Chair
Professor Dewey Dohoy Jung
Associate Professor German Reyes-Villanueva
Professor Alex Yasha Yi

Animesh Koneru

akoneru@umich.edu

ORCID# 0000-0001-6159-6678

Dedication

I would like to dedicate my work to my late grandmother, the first doctorate in our family, a true inspiration and who played a significant role in shaping me as an individual. I wish that my late grandparents, whom I couldn't bid a final farewell to, were here to share the joy of this accomplishment. I would also like to dedicate my work to my family, whose encouragement helped me to the finish line

Acknowledgements

I would like to express my deepest gratitude to my advisor, Dr Ben Li, for his support, and mentorship throughout the course of my research. I extend my thanks to the committee members Dr German Reyes, Dr Yasha Yi and Dr Dohoy Jung for their valuable feedback, and availability.

I would like to express my heartfelt gratitude to Somnio Global LLC for generously funding my research work and providing me the opportunity to explore my academic interests beyond my work responsibilities. Working with several accomplished colleagues at the company has been a great source of inspiration. I am thankful to Dr. Vladimir Golota, Dr Alex Kuprin and Dr. Yaping Wang for their invaluable expertise and advice, which was pivotal in shaping my research work. I am very grateful to Dr. Pravansu Mohanty, who not only encouraged me to pursue my PhD but also guided me, to enhance my knowledge and skills. His support has been instrumental in my academic and career growth.

To my family and friends, I am appreciative for their love and encouragement which kept me moving during any challenging times, and I feel truly blessed to have them on my side. I am forever indebted to my mother and father, who have always prioritized my success over their desires. Their belief in my abilities has been a driving force thought this journey. Thank you, both, for coping through the 4 long years of separation, with a resilient smile. A special thank you goes to my wife, whose patience, sacrifices and picking up most of my responsibilities, have not only eased my efforts but also have been a source of strength for past few years.

I strongly believe any success cannot be an individual's accomplishment, and I would like to thank everyone from the bottom of my heart who have directly or indirectly helped me to get through with this journey.

Table of Contents

List of Figures

List of Tables

Abstract

CuCr composites are widely used as high-performance contact materials in medium voltage Vacuum Interrupters, especially in switching applications up to 145kV. These composites exhibit exceptional properties, including high conductivity, excellent hardness, and superior arc-erosion resistance compared to other solid solution copper alloys. To enhance the manufacturing efficiency of traditional composite manufacturing methods, this study explores two coating techniques: 1) CuCr cold spray, which produces coatings with lower Cr content, and 2) Vacuum Arc Plasma Deposition (VAPD), which produces films with high Cr content. While recent research has shown promising results in arc-erosion behavior and overall breakdown performance with nanostructured composites, conventional methods for producing CuCr composites are limited in achieving nanometer sized microstructures. The proposed VAPD technique produces nanostructured CuCr films, as it achieves atomic scale mixing, and also offers the opportunity to explore non-equilibrium microstructures that are challenging to obtain using current production methods.

The current study is structured into three parts. In Part 1, CuCr coatings are produced using cold-spray deposition, where deposition pressures are adjusted to manipulate critical velocities of depositing powders. This impacts a coating's internal porosity and conductivity, both of which are critical for contact material applications. The microstructures of the cold-sprayed CuCr coatings are analyzed, and properties such as residual stresses, hardness, and conductivity are measured. The breakdown performance of these coatings is established by comparison with bulk CuCr composites produced through traditional manufacturing methods. Part 2 explores VAPD CuCr

films produced with co-deposition technique by varying Cu/Cr cathode currents. Higher ion-fluxes result in Cu-self sputtering phenomena, leading to compositional non-uniformity across the films. The coatings developed through VAPD exhibit a sub-micron layered Cu-Cr structure, attributed to high adatom mobility and phase separation of the immiscible elements on a sub-micron scale. SRIM calculations are performed to validate the high sputtering yield of Cu from the films under the bombardment of high energy Cu and Cr ions. Part 3 focuses on producing CuCr films using single composite cathode with 65% Cr content, achieved through a pressure-less infiltration technique. The deposition process is carried out under different substrate biasing conditions to study the effects of incident ion energies on microstructure, compositional uniformity, and film density. The hardness and electrical properties of the films are measured. Finally, the vacuum breakdown performance of the CuCr films is established and compared against traditional bulk composites with similar compositions. This study contributes to a comprehensive understanding of CuCr coatings and films, especially on various sub-micron and nanoscale CuCr microstructures that can be obtained, their corresponding properties, and breakdown performance. The findings hold promise for advancements in producing high-performance contact materials.

Chapter 1 Introduction to CuCr Contact Materials and Scope of Present Study

1.1 Introduction

Vacuum interrupters (VI) are extensively utilized for switching high-power electrical applications up to 145kV. Typical VI is constructed with a well-sealed vacuum chamber containing a pair of electrical contacts (depicted in fig.1.1). During a switching operation, the closed contacts are separated to interrupt the circuit current, resulting in the generation of an arc between them. The high dielectric strength of the vacuum environment within a VI rapidly extinguishes any generated arc. Once the contacts are separated, they are designed to withstand any imposed electric field without experiencing additional breakdown. However, the very occurrence of the arc puts a significant thermal burden on the contacts, particularly at the regions where the arc attaches. The localized high temperatures on a contact's surface can lead to erosion and subsequent damage for future use. Furthermore, when VI are utilized for fault current interruption applications, the contacts often remain closed for extended periods. In such cases, it is very important for the contacts to maintain exceptional electrical conductivity. This characteristic is critical to minimize joule heating at the contact interface, otherwise leads to an increased tendency for the contacts to weld together. Ultimately, the successful implementation of vacuum interrupters relies on the degree of vacuum and the quality of electrical contacts used. The performance of these contacts, in turn, depends on the properties of the materials employed [1,2].

Vacuum interrupters offer numerous advantages over traditional switchgear that rely on oil, air-blasts, or SF6 gas as dielectric environments. With a vacuum medium, interrupters exhibit exceptional dielectric strength, enabling high voltage withstand ability within a compact contact

gap, reducing the overall size of the switchgear. Additionally, vacuum interrupters are maintenance-free and operate with low-energy mechanisms. They have a long lifespan and self-contain arcs, making them ideal for interrupting voltages across a wide range of power circuits in various industries.

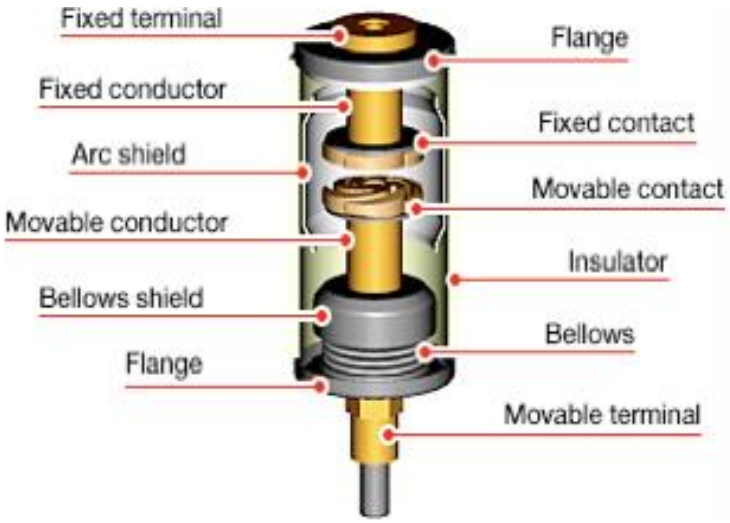

Figure 1.1 Cross-section of a vacuum interrupter [36]

Carefully engineered composites with high arc-erosion resistance and electrical conductivity are currently being used as contact materials. Contact materials for VI are made up of one highly conductive matrix material and at least one uniformly dispersed refractory material. The quality of these composites, which can be affected by defects such as interfacial porosity, high residual gas content, and non-uniform phase distribution, directly impacts the performance of vacuum interrupters. Porosity reduction enhances the interrupter's breaking capacity, and lowering gas content reduces the likelihood of arc re-ignition. The use of composite materials allows for tailoring contact properties to meet different breaking capacity requirements. Due to their high breaking capacity and high voltage withstand capability, CuCr composites are widely utilized as contacts in vacuum interrupters for electrical circuits up to 84 kV [1,4]. The Cr content in the

contacts varies between 20wt% to 60wt% depending on the application, i.e., contact interruption for fault currents vs switching of load currents. Cu75Cr25 composites are approximately 40% more electrically conductive and 25% less hard than Cu50Cr50. CuCr composites with low Cr% have lower hardness and exhibit higher tendency to weld [1,6,10,29]. In such situations, weld tendency of contacts can be further improved by addition of small amounts (1-5 wt%) of W or C [5,18]. Irrespective of an application's voltage or current specification, the choice of the contact material and the correct design of the electrical contact are essential. It is of utmost importance to produce high density CuCr composites to ensures successful functioning of the VI.

1.2 Theory of operation for VI contact materials

A VI comprises of a movable contact which is held against the fixed contact with a predetermined force to minimize the interface resistance. Due to surface roughness, the current flowing through the contacts is confined to a small, constricted areas, resulting in a blow-off force. This blow-off force opposes the contact, leading to an increase in contact resistance. To mitigate this, a spring force is selected to minimize the interface resistance of the contacts. When a circuit current and voltage impressed across opening contacts exceeds a certain threshold minimum, an arc will invariably form between them. This arc formation always involves the generation of metal vapor from the contacts. It is crucial to quickly extinguish this arc to control contact erosion and maintain the integrity of the contacts. As the contact force (F_c) approaches to 0 during contact separation, the contact resistance R_c tends to maximum value ($R_c \propto F_c^{-\frac{1}{2}}$). Consequently, the voltage (U_c) across the contacts increases. At the instant when the voltage across the closed contacts exceeds the melting voltage of the contact material (given by eq 1.1, where T_p is contact temperature and T_0 is bulk temperature), a molten metal bridge forms, which is dragged along with the opening contacts, creating a path for current flow and initiating arcing. When the potential

difference across closed contact interface exceeds 0.67V for Cr or 0.46V for Cu, the materials begin to melt. Therefore, it is essential to minimize localized resistivity variations of CuCr composites to avoid excessive erosion.

$$U_c = \left(4L\{{T_p}^2 - {T_0}^2\}\right)^{1/2} \tag{1.1}$$

Another important criterion for electrical contacts is their ability to resist welding, especially when interrupting high-load currents or inrush fault currents in circuits. As previously mentioned, the effective contact area is determined by surface features and is typically much smaller than the actual cross-sectional area of the contact. At localized contact points, excessive heating can occur, leading to a scenario where certain areas of the contact soften and fuse together due to joule heating, resulting in a localized weld. However, the weld area (a_0) can be improved by enhancing the hardness of the contact material, as indicated by equation 1.2 (where, H_c is hardness, R is contact radius, E is the elastic modulus). By increasing the hardness at a given contact force, the contact material becomes more resistant to softening and fusion, thereby reducing the likelihood of localized welding [4,35].

$$a_0 = \sqrt{{F_c}/{\pi H_c} + \left({1.5F_cR}/{E}\right)^{2/3}} \tag{1.2}$$

In the arcing zone, the metal vapor undergoes ionization due to the electric field imparted across the opening contacts. This ionization process gives rise to multitude of cathode spots on the contact surface, which repel each other and drift towards the contact's edges where they get extinguished. Once the arc is successfully extinguished, no further vapor should be generated between the open contacts, provided they have the necessary voltage withstand capability.

A breakdown occurs across a pair of open electrodes if there is a source for electrons. Electric field strength between a pair of contacts in a VI is typically estimated with eq. 1.3 and geometric enhancement factor (β) is dependent on the surface properties of the contacts. For a given electrode distance (d) and potential difference (U), the field emission current (I_e) can be predicted by Fowler-Nordheim criterion (eq 1.4) based on the contact's work function (Ø). To achieve lower field emission currents, we can focus on 1) increasing the work function, 2) reducing the geometric enhancement factor, and 3) minimizing the emission area (A_e) of the contacts. These factors are of particular interest in the current study [1,2].

$$E = {\beta U}/{d} \tag{1.3}$$

$$i_e = \frac{A_e . B_1 . (\beta U)^2}{\phi d^2} \times e^{\left(\frac{-B_2 \phi^{1.5} d}{\beta U}\right)} \tag{1.4}$$

1.3 Production of CuCr composites

1.3.1 CuCr System

Cu-Cr system exhibits limited solid solubility [22], as depicted in the phase diagram illustrated in Fig 1.2. At approximately 1077ºC, the system reaches its maximum equilibrium solubility limit of around 1.5at%. This indicates the extent to which the reinforcing material Cr is soluble in the Cu matrix during composite processing. The limited solubility between the matrix and particulate phases ensures minimal reduction in the electrical conductivity of the composite after processing. In powder processing, a range of densification temperatures can be selected up to the eutectic point of the system to maintain theoretical resistivity of the composite. However, when processing CuCr above the melting point of Cu, a maximum of up to 1.5% Cr diffuses into the molten Cu. This diffusion can potentially impact the conductivity of the material. To improve the conductivity, dissolved Cr in Cu can be precipitated out by implementing slow cooling (or

stepwise cooling) below the solution treating temperature of the CuCr alloy. Fig 1.3 provides a visual representation of the sequential steps that occur during solidification when processing a CuCr composite close to melting temperatures of Cu. At densification temperatures, molten Cu forms, wets the Cr particulate phase, and spreads through the dissolution of Cr. As the temperature decreases below the melting point of Cu, nucleation of Cu takes place on the surface of particulate Cr phase, gradually leading to the precipitation of any dissolved Cr during equilibrium cooling [13].

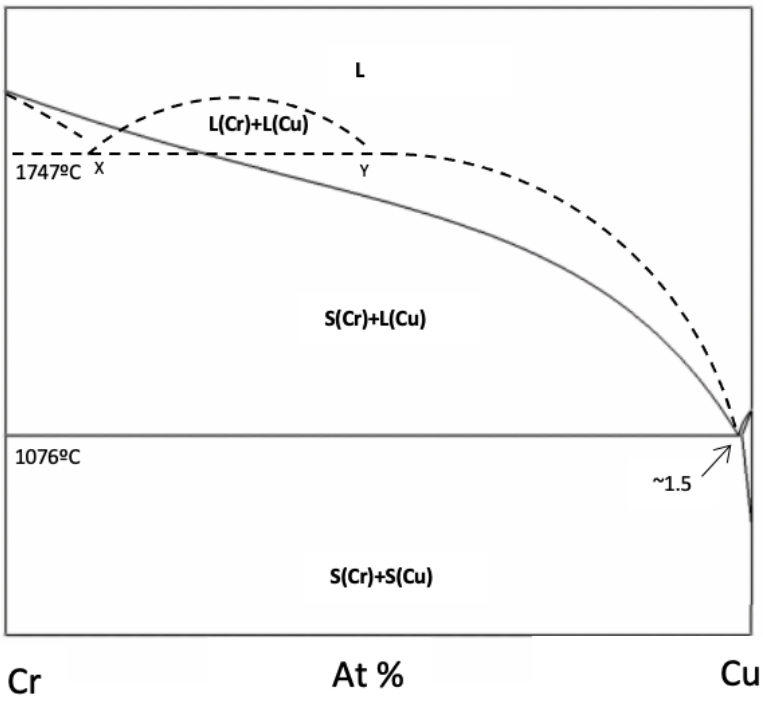

Figure 1.2 Phase diagram of CuCr system

Some studies have identified the existence of a liquid miscibility gap when employing rapid quench solidification techniques for processing CuCr alloy melts [7,27,28]. This phase diagram, represented by a dotted line in Fig 1.2, illustrates a monotectic system characterized by a flat miscibility gap. The gap observed is not consistent and depends on processing conditions, oxide contamination and melting techniques. Some experimentally confirmed observations for the gap is between Cu atomic fractions of 17% and 50% [7] and Cr mass fractions of 40% and 94.5% [27],

occurring at the monotectic temperature of approximately 1750ºC. Producing CuCr alloys above the liquidous temperatures can lead to the formation of metastable alloy compositions, and these compositions can have an impact on both the conductivity and strength of the CuCr materials [8]. Therefore, careful control of processing conditions, particularly in relation to temperature, is essential to achieve desired material properties in CuCr alloys.

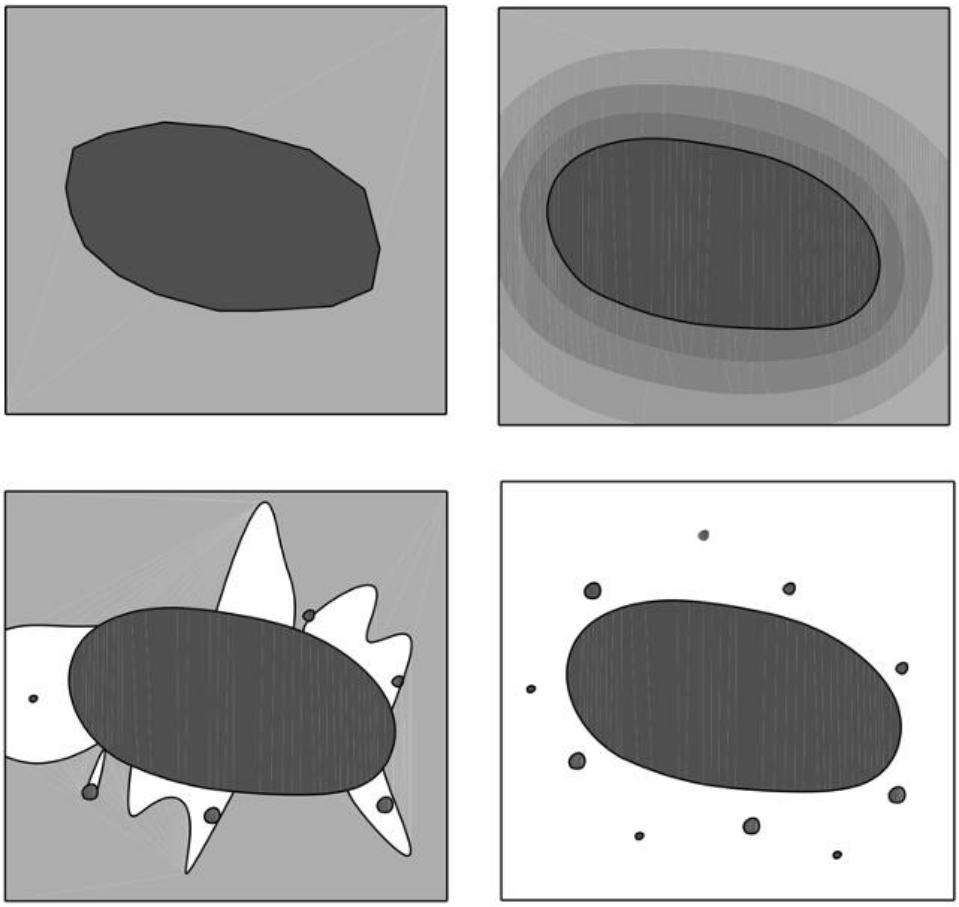

Figure 1.3 Cr particle suspended in molten matrix Cr (b) Diffusion of the Cr into molten Cu (c) Nucleation of solid phase Cu on particulate Cr & precipitation of diffused Cr (d) Complete solidification of Cu engulfing Cr

1.3.2 Powder metallurgy methods for CuCr composites

Several powder metallurgy (PM) techniques have been developed for the production of CuCr electrical contacts, and their selection is based on the required composition of the refractory Cr phase. One commonly used technique is the Press-Sinter (PS) method, where Cu and Cr powders are mixed and pressed in a die to form a green compact. This green compact is then

densified through solid-state or liquid-phase sintering in a high vacuum environment at temperatures around the melting point of Cu. PS method offers advantages such as lower associated costs and the ability to produce near net-shapes, which streamlines the manufacturing process. However, one drawback of this technique is the potential for high retained porosity, especially in compositions with higher refractory content (>35wt% Cr). The presence of surface porosity in electrical contacts reduces the interfacial bonding between particles surrounding voids, leading to increased localized arc erosion and a higher risk of dielectric breakdown. Furthermore, a higher level of retained porosity results in increased resistivity, which is undesirable for electrical contacts [1].

In previous studies, the Press-Sinter-Repress (PSR) process has been proposed as a method to produce electrical contacts with reduced retained porosity when compared to PS process. After the initial compaction of the powder and sintering of the compact (as in the PS technique), the composite undergoes an additional mechanical forming or isostatic pressing step to further decrease porosity in the PSR method. This process results in achieving 99% of theoretical densities for contacts that contain 25-50% refractory material by mass [1,5,35]. However, it has been observed that samples produced using the PSR method can exhibit variations in conductivity across different planes, depending on the pressing direction. In a previous study [5] to determine the conductivity of solid-phase PS Cu-Cr contacts, conductivity values were measured in two different directions: 1) direction corresponds to the direction in which the powders were pressed (Z-axis), 2) in a longitudinal direction (XY-palne) perpendicular to pressing, and demonstrated that the conductivity in the longitudinal direction is lower than the pressing direction. It was reasoned that the variation is caused by a significant contribution from the phase boundaries of the composite material. This contribution could have been due to the segregation of contaminants

towards the grain boundaries or from internal stresses caused by the deformation of grains. To address the potential variations in conductivity within produced composites, researchers have explored techniques such as liquid-phase infiltration or Vacuum Induction Melting (VIM) and Vacuum Arc Melting (VAM) to achieve more uniform electrical properties in Cu-Cr contacts.

1.3.3 Liquid phase processing of CuCr composites

Another method used to produce highly dense electrical contacts is melt-casting (MC). This process involves melting a mixture of a conductive matrix and refractory materials in a vacuum induction furnace or using a vacuum arc source, the molten mixture is then cast to form the final composite, which is later mechanically formed into a blank for machining or directly machined to obtain electrical contacts. MC methods require very high temperatures, often exceeding the melting point of the refractory phase, to melt both the refractory and matrix phases during processing. Consequently, high cooling rates are necessary when casting the melt to prevent the segregation of the reinforcing Cr phase from the Cu matrix during solidification. Some of Cr reinforcing phases exhibit metastable solubility in the Cu matrix when subjected to rapid cooling from high temperatures, resulting in a decrease in electrical conductivity. In such cases, an additional aging treatment is required to achieve high electrical conductivity for the contacts. While existing MC technologies have been successful in fabricating composites with low refractory content, processing becomes more challenging when higher refractory content is required. At higher Cr contents, the microstructures formed often consist of large alternating bands of low conductivity phases [7]. These banded layers resemble large columnar structures, and if they are not oriented in the transverse direction to the contact's surface, they can lead to undesired anisotropic resistivity in CuCr contacts.

For high refractory content in contact materials, a press-sinter-infiltration (PSI) method is preferred as it produces very high-density composites. When processing composites by PSI technique, pressing & sintering is performed to develop a partially fused refractory preform with known porosity. Later the sintered object is subjected to infiltration in a furnace by a low melting point matrix material. During infiltration, matrix material is placed in contact with the preform, under specific temperature and atmospheric control, matrix material melts into the pores of the previously formed preform body. The preform used for infiltration can also be made with part matrix material along with refractory material to obtain composites with low refractory content. PSI techniques are currently modified to remove a separate sintering step, either by subjecting the pressed object to sintering before the onset of infiltration in one thermal cycle or pressing the premixed powder to very high compaction ratios. Because infiltration gravity assisted, only thin, upto few 10s of mm of pore-free composite layers are formed. For all PSI methods, composite bodies produced have high density, but they entail extensive processing times due to slower kinetics of infiltration [1,35].

1.3.4 Other novel techniques to produce CuCr composites

The widely implemented powder metallurgy (PM) methods discussed above typically result in composites with refractory phases that are micron-sized (>20μm). This limits the reduction in the size of contacts beyond the current accepted performance limits, i.e at least 3mm thick CuCr layers. To overcome this limitation by improving the arc-erosion resistance of vacuum interrupters (VI), researchers have explored high energy heating methods with rapid solidification techniques such as selective laser melting (SLM) and electron-beam evaporation/melting (EBM) [9,23,32]. In one research study, a mixture of molten Cu and Cr is atomized into small particles, which are then pressed, and plasma sintered to form a dense contact material [26]. Another

example involves melting the top surface of a sintered contact structure using a vacuum arc or laser [10,27]. These methods incorporate sub-micron or nanocrystalline refractory phases into the final composite, and provide promising results in terms of breakdown performance, which will be further discussed in the next section. However, it is important to note that these processes are more complex and time-consuming compared to conventional PM techniques.

1.4 Nano-crystalline CuCr composites for improved breakdown performance

The current trend towards miniaturization and reduced contact pressure in vacuum interrupters (VI) has led to increased research in advanced additive manufacturing techniques for contact production. Initial studies have shown that incorporating ultrafine refractory Cr particles (<1μm) in the Cu matrix improves the hardness of the composites compared to traditional powder metallurgy (PM) techniques [9,15]. Further investigation was focused on the effect of crystal structure on arc erosion behavior, and it has been observed that materials with amorphous and nanocrystalline phases exhibit well-diffused arc tracks and smaller arc spots compared to materials with micron-sized refractory phases, resulting in improved arc-erosion resistance [11,12,25,29]. Similar trends have been observed for breakdown strength, chopping current and welding resistance, with nanocrystalline materials demonstrating improved properties [4,6,35]. In a study comparing microcrystalline and nanocrystalline CuCr50 contacts as cathodes, it was found that the breakdown strength of the nanocrystalline CuCr50 was approximately 12% higher than that of the microcrystalline CuCr50 [33]. However, for lower Cr content, specifically CuCr25, the microcrystalline material exhibited marginally higher breakdown strength. This was attributed to the high particle emissions observed for the nanocrystalline material when used as an anode [37].

Efforts have also been made to explore the characteristics of Cu-based composite thin films produced by DC magnetron sputtering, which can achieve nanocrystalline and amorphous

coatings. Sputtering facilitates atomic-scale mixing and produces nanocomposite CuCr coatings which exhibit much higher hardness [16,18]. Another advantage of sputter coatings is that by changing process parameters a coating's crystal structure can be precisely tailored between amorphous or nanocrystalline, and it has been studied that arc erosion measured on pure Cu nanostructured coatings were 50% lower than the conventional bulk Cu cathodes [12]. It was also found that immiscible Cu-W, Cu-Cr systems showed a certain degree of miscibility, at least in a metastable as-deposited state, further raising the curiosity on such coatings which potentially can have superior properties [17-19]. The drawback of sputtered coatings is that the rate of deposition is very low (typically between 1-5μm/hr) making it an expensive option for VI contact application.

As an alternative to the DC magnetron sputtering, vacuum arc plasma deposition technique (VAPD) is proposed in this study to produce CuCr coatings. This process can synthesize nanostructured coatings like sputtering but at much higher deposition rates [20]. Some commercially available VAPD systems deposit coatings at a rate of 50-100μm/hr based on the material being used. One of the objectives for current study is to develop and investigate Cu based composite coatings produced by Vacuum Arc Plasma Deposition (VAPD) as a potential substitution or as a supplemental process to the current contact manufacturing.

1.5 Objective of current work and scope of the report

The primary motivation of the current study is to explore the use of coatings as an alternative manufacturing method for CuCr materials. This approach overcomes the time-consuming nature of traditional manufacturing processes. In the conventional approach, after CuCr composites with the desired composition are produced, they need to undergo vacuum brazing onto current-carrying copper electrodes before being installed in vacuum interrupters (VIs). This additional brazing step adds complexity and time to the overall manufacturing process. To address

this, the study proposes a more efficient and streamlined manufacturing process by directly depositing conformal CuCr coatings onto pre-machined unibody copper substrates, eliminating the need for time-intensive vacuum brazing (the improved contact manufacturing process is illustrated in Figure 1.4). Implementing conformal CuCr thin film deposition onto copper electrodes, not only reduces the machining times but also enhances the breakdown performance of the contacts owing to the finer uniform Cr phase distribution. Two coating methods are employed for the study: Cold-Spray and Vacuum arc plasma deposition (VAPD), to produce CuCr coatings. The cold spray technique produces upto 2mm thick CuCr coatings, with uniform Cr phase distribution in the range of 20-45µm. On the other hand, VAPD produces conformal CuCr thin films, which are ~20µm thick and having nano-scale mixing of Cu and Cr phases. By employing both Cold-Spray and VAPD techniques, the study explores the potential of these coating methodologies in producing CuCr coatings with different thicknesses and structures. This allows for a comprehensive investigation into the effectiveness and performance of CuCr coatings across a range of applications.

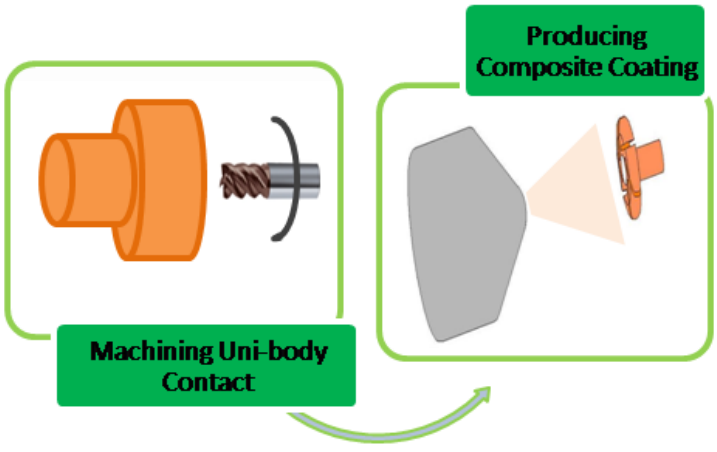

Figure 1.4 Proposed uni-body contact manufacturing with CuCr coatings

The current study is presented in following chapters:

- Chapter 2: Literature Review and Evaluation of CuCr Cold-Spray Coatings- This chapter presents a comprehensive review of the literature on CuCr cold-spray coatings and their breakdown performance. It includes a comparison with press-sinter-infiltrated CuCr reference sample, providing insights into the effectiveness of cold-spray coatings for contact applications.
- Chapter 3: Microstructural Evaluation of CuCr Thin Films Produced by VAPD Co-Deposition Technique- In this chapter, a detailed literature review is presented, focusing on the microstructural evaluation of CuCr thin films produced using the Vacuum arc plasma deposition (VAPD) co-deposition technique. The chapter highlights the relevant findings on films obtained and discusses the impact of ion self-sputtering yield on microstructure of co-deposited CuCr thin films.
- Chapter 4: Preparation of Composite Targets for Single-Target VAPD Deposition- It details the methodology and techniques employed to create the desired CuCr composite targets, which serve as the cathode material for the subsequent single target deposition.
- Chapter 5: Microstructural Evaluation of Single-Target CuCr Thin Films and Initial Breakdown Performance-This chapter focuses on the microstructural evaluation of the CuCr thin films produced using the single-target VAPD deposition. It explores the structural characteristics and properties of the thin films and provides an initial assessment of their breakdown performance. This chapter also investigates the influence of bias voltage on the microstructure, properties, and breakdown performance of CuCr thin films. It examines the breakdown performance of CuCr films with reference to a bulk CuCr composite.

- Chapter 6: Summary, Contributions and Future Work

These chapters collectively contribute to the understanding of CuCr coatings and thin films, providing valuable insights into their microstructural characteristics, properties, and breakdown performance.

References

[1] P.G. Slade, “The Vacuum Interrupter: Theory, Design, and Application”, CRC, 2008.

[2] J. M. Lafferty, “Vacuum Arcs – Theory and Applications”, Wiley, 1980.

[3] J. Koskinen, “Chapter: Cathodic-Arc and Thermal-Evaporation Deposition”, Comprehensive Materials Processing, Elsevier, 2014, Pages 3-55.

[4] Chang, Yanli & Zheng, Wei & Zhou, Zhiming & Zhai, Yuxiang & Wang, Yaping, “Preparation and Performance of Cu-Cr Contact Materials for Vacuum Switches with Low Contact Pressure”, Journal of Electronic Materials, 2016, Volume 45, pages 00.

[5] K.V.Klinski-Wetzel, C.Kowanda, M.Heilmaier, F.E.H. Mueller, “The influence of microstructural features on the electrical conductivity of solid phase sintered CuCr composites”, Journal of Alloys and Compounds, Volume 631, 2015, Pages 237-247.

[6] W. F. Rieder, M. Schussek, W. Glatzle and E. Kny, "The influence of composition and Cr particle size of Cu/Cr contacts on chopping current, contact resistance, and breakdown voltage in vacuum interrupters," IEEE Transactions on Components, Hybrids, and Manufacturing Technology, vol. 12, no. 2, pp. 273-283, June 1989.

[7] Zhou, Z. M., et al. "On the Metastable Miscibility Gap in Liquid Cu–Cr Alloys." Journal of Materials Science, 2009, 44.14.

[8] Y. Wang, X.Song, Z.SUN, X.Zhou, J.Guo, “The Solidification of CuCr alloys under various cooling rates”, Material Science-poland, Vol. 25, 2007, pages 199-207.

[9] Yuhong Chen, Shubin Ren, Yang Zhao, Xuanhui Qu, “Microstructure and properties of CuCr alloy manufactured by selective laser melting,” Journal of Alloys and Compounds, Volume 786, 2019, Pages 189-197.

[10] Shi-xin XIU, Ren YANG, Jun XUE, Jin-xing WANG, Jia-yi WANG, “Microstructure and properties of CuCr contact materials with different Cr content”, Transactions of Nonferrous Metals Society of China, Volume 21, Supplement 2, 2011.

[11] Yaping Wang, Chengyu Zhang, Hui Zhang, Bingjun Ding and Ke Lu, “Effect of the microstructure of electrode materials on arc cathode spot dynamics”, Journal of Physics D: Applied Physics, Volume 36, 2006, page 21.

[12] Lakshminarayana Rao, Richard J Munz and Jean-Luc Meunier, “Vacuum arc velocity and erosion rate measurements on nanostructured plasma and HVOF spray coatings”, Journal of Physics D: Applied Physics, Volume 40, 2007, 2192.

[13] Z.P. Que, J.H. Lee, H.M. Jung, J.H. Shin, S.Z. Han, K.J. Euh, “Microstructure evolution in Cu–1.54wt% Cr alloy during directional solidification”, Journal of Crystal Growth, Volume 362, 2013, Pages 58-61.

[14] Zaoli Zhang, Jinming Guo, Gerhard Dehm, Reinhard Pippan, “In-situ tracking the structural and chemical evolution of nanostructured CuCr alloys”, Acta Materialia, Volume 138, 2017, Pages 42-51.

[15] V.V. Bukhanovsky, N.I. Grechanyuk, R.V. Minakova, I. Mamuzich, V.V. Kharchenko, N.P. Rudnitsky, “Production technology, structure and properties of Cu–W layered composite condensed materials for electrical contacts”, International Journal of Refractory Metals and Hard Materials, Volume 29, Issue 5, 2011.

[16] G.M. Mikhailov, I.V. Malikov, A.V. Chernykh, V.T. Petrashov, “The effect of growth temperature on electrical conductivity and on the structure of thin refractory metal films, grown by laser ablation deposition, Thin Solid Films, Volume 293, Issues 1–2, 1997, Pages 315-319.

[17] F.T.N. Vüllers, R. Spolenak, “Alpha- vs. beta-W nanocrystalline thin films: A comprehensive study of sputter parameters and resulting materials' properties”, Thin Solid Films, Volume 577, 2015, Pages 26-34.

[18] V. Bukhanovsky, N.I. Grechanyuk, R.V. Minakova, I. Mamuzich, V.V. Kharchenko, N.P. Rudnitsky, “Production technology, structure and properties of Cu–W layered composite condensed materials for electrical contacts”, International Journal of Refractory Metals and Hard Materials, Volume 29, Issue 5, 2011, Pages 573-581.

[19] J Musil, I Leipner, M Kolega, “Nanocrystalline and nanocomposite CrCu and CrCu–N films prepared by magnetron sputtering, Surface and Coatings Technology”, Volume 115, Issue 1, 1999, Pages 32-37.

[20] F.T.N. Vüllers, R. Spolenak, “From solid solutions to fully phase separated interpenetrating networks in sputter deposited “immiscible” W–Cu thin films”, Acta Materialia, Volume 99, 2015, Pages 213-227.

[21] An, W., Dou, Z., Han, J., Zhang, T., “Microstructure uniformity control of CuCr alloy prepared in-situ by aluminothermic reduction coupled with permanent magnetic stirring”, Journal of Alloys and Compounds 960, 170797,2023.

[22] Chakrabarti, D.J., Laughlin, D.E., “The Cr-Cu (Chromium-Copper) system”, Bulletin of Alloy Phase Diagrams 5, 1984, 59–68.

[23] Durakov, V.G., Gnyusov, S.F., Dampilon, B.V., Dehonova, S.Z., Ubiennykh, B.I., “Microstructure and properties of vacuum electron beam facing CuCr25 contact material”, 2012 25th International Symposium on Discharges and Electrical Insulation in Vacuum (ISDEIV), pp. 525–528.

[24] Frey, P., Klink, N., Michal, R., Saeger, K.E., “Metallurgical aspects of contact materials for vacuum switching devices”, IEEE Transactions on Plasma Science 17, 734–740, 1989.

[25] L. Yu, J. Wang, Y. Geng, G. Kong and Z. Liu, "High-Current Vacuum Arc Phenomena of Nanocrystalline CuCr25 Contact Material," in IEEE Transactions on Plasma Science, vol. 39, no. 6, pp. 1418-1426, June 2011.

[26] Kuskov, K.V., Rogachev, A.S., Vadchenko, S.G., Shkodich, N.F., Rouvimov, S., Shchukin, A.S., Illarionova, E.V., Kudryashov, V.A., Mukasyan, A.S., "Resistance of microcrystalline and nanocrystalline Cu/Cr pseudo-alloys to vacuum discharge", Journal of Alloys and Compounds 750, 2018, 811–818.

[27] R. Müller, "Arc-Melted CuCr alloys as contact materials for vacuum interrupters," Siemens Forsch.- Entwicklungsber, vol. 17, no. 3, pp. 105–111, 1988.

[28] H. Okamoto, "Cr-Cu (Chromium-Copper)," J. Phase Equilib. Diffus., vol. 33, no. 4, pp. 342–343, Aug. 2012.

[29] Z. Yang, Q. Zhang, C. Zhang, Y. Sun, and B. Ding, "Influence of microstructure of CuCr25 cathode on the motion of vacuum arc spots," Physics Letters A, vol. 353, no. 1, pp. 98–100, Apr. 2006.

[30] "Low Electrode Erosion Rate Of Nanocrystalline Cucr-50 Alloy In Vacuum", Modern Physics Letters B Vol. 20, No. 21, pp. 1329-1334 (2006).

[31] W. An, Z. Dou, J. Han, and T. Zhang, "Microstructure uniformity control of CuCr alloy prepared in-situ by aluminothermic reduction coupled with permanent magnetic stirring," Journal of Alloys and Compounds, vol. 960, p. 170797, Oct. 2023.

[32] A. Schneider, S. Popov, V. G. Durakov, B. V. Dampilon, S. Z. Dehonova, and A. Batrakov, "On breaking capacity of the CuCr25 composite material produced with electron-beam cladding," in 2012 25th International Symposium on Discharges and Electrical Insulation in Vacuum (ISDEIV), Sep.

[33] Zhang, C., Yang, Z., Wang, Y. and Ding, B, "Properties of Nanocrystalline CuCr50 Contact Material", Adv. Eng. Mater., 7, 2005.

[34] Yu Y.T., Pochiraju K.V., "Multi-scale analysis of diffusivity in polymers and polymeric matrix composites", 22nd Technical Conference of the American Society for Composites 2007 - Composites: Enabling a New Era in Civil Aviation, 2, pp. 929 - 948.

[35] Jin-ru Han, Zhi-he Dou, Ting-an Zhang, Wang An, "Review of the recent Chinese research on the electrical properties of CuCr contacts for vacuum interrupters", Journal of Materials Research and Technology, Volume 25, 2023, Pages 1585-1598.

[36] Shemshadi, Asaad, "Life time enhancement of a Vacuum Interrupter for AC Smart Grid Applications", International Journal of Electronics and Electrical Engineering, 2012.

[37] L. Zhao, Z. Li, K. Shi, J. He and H. Li, "Electrical Properties of Nanocrystalline CuCr25 Contact Material," in *IEEE Transactions on Components, Packaging and Manufacturing Technology*, vol. 3, no. 4, pp. 625-632, April 2013

Chapter 2 Evaluation of Cold-Sprayed CuCr Coatings for VI Applications

Abstract

In the present study, cold-sprayed copper-chromium (CuCr) coatings are investigated as an alternative to traditional CuCr composites which are used in medium voltage vacuum interrupters (VIs). Test samples for this study are produced by depositing coatings on copper substrates using pre-mixed Cu and Cr powders with N2 as main gas, at two different pressures. Electrical resistivity and hardness of CuCr coatings are measured, and compared with bulk CuCr composites which are produced by the conventional press-sinter-infiltration (PSI) method. Furthermore, the coatings are subjected to electrical arcs in a vacuum chamber to establish vacuum breakdown characteristics. Through the annealing studies conducted on CuCr coatings at 200°C and 425°C, improvements were observed in the electrical resistivity and vacuum breakdown strength of the coatings. These improvements brought the properties of the annealed CuCr coatings to a level comparable to the PSI samples.

2.1 Introduction

CuCr composites are widely used as electrical contacts in vacuum interrupters (VIs) due to their excellent electrical conductivity, high breakdown strength and superior arc erosion resistance. Commercially available CuCr composites are manufactured using either the press-sinter (PS) or press-sinter-infiltration (PSI) methods, depending on the desired Cr content and density requirements. These methods involve using powder precursors and are performed under vacuum conditions to prevent the formation of undesirable oxides, especially in the chromium phase [9,11,21,22]. However, these traditional manufacturing processes are time-consuming. After the

CuCr composites with the desired composition are produced, they need to be vacuum brazed onto current-carrying copper electrodes before being installed in VIs. This additional step of brazing adds complexity and time to the manufacturing process. In the present study, an alternative method called cold gas dynamic spray (CGDS) or cold-spray is employed to produce dense CuCr coatings directly onto copper substrates, eliminating the need for time-intensive vacuum processing and brazing. A potentially more efficient and streamlined manufacturing process is achieved by cold-spraying CuCr coatings onto copper electrodes.

Cold spray, a technique from the thermal spray family, employs low deposition temperatures and high powder velocities to plastically deform ductile materials onto a substrate to form dense oxide-free coatings. In this process the feedstock powders are accelerated to supersonic velocities in a convergent-divergent nozzle using an inert carrier gas. A coating is formed due to adhesion when accelerated powders with high kinetic energy impact with the substrate or to other deforming particles [2,6]. Therefore, successful bonding of impacting particles requires localized transition from elastic to plastic deformation, which occurs at high impact velocities known as critical velocity. This critical velocity is dependent on the precursor properties such as bulk modulus, particle morphology and size; as well as process parameters such as feed rates, carrier gas temperatures and pressures [2,5]. In previous research, the parameters influencing critical velocities to produce dense copper coatings have been extensively investigated. However, when it comes to forming CuCr coatings, the presence of a non-deforming Cr phase adds complexity. The Cr phase needs to be encapsulated within a deforming Cu phase. This presence of the Cr phase affects the previously established process parameters that influence the critical velocity required for Cu deformation. To achieve highly dense microstructures in coatings containing an undeformed Cr phase, it is crucial to formulate parameters that promote both inter-particulate and intra-

particulate adhesion. Improper adhesion or high porosity in the coatings can adversely affect their electrical conductivity and breakdown performance when used as electrical contacts. In the present study, the effect of main gas pressure on coating properties, such as porosity and electrical conductivity, and Cr phase retention are investigated to optimize the cold spray process to produce CuCr coatings.

Cold-Spray process offers advantages over other thermal spray techniques, as it does not involve melting the feedstock material. This prevents the formation of non-metallic bonds at the particulate interfaces, which can occur due to oxide formation or other undesirable chemical reactions. Consequently, CuCr coatings produced by Cold-Spray can exhibit high electrical conductivity with low oxide content, making them desirable for use as contact materials [7,8]. However, in the as-sprayed state, CuCr coatings have high dislocation densities within the Cu phase, resulting from the plastic deformation that occurs during the deposition process. These dislocations impede the motion of free electrons, thereby reducing the overall electrical conductivity of the coatings. Additionally, the final Cr content in the coatings also influences their electrical conductivity. Lowering the Cr content to compensate for the reduced electrical conductivity of the as-sprayed Cu phase can compromise the breakdown strength and arc-erosion resistance of the coatings. To improve electrical conductivity of the CuCr coatings, the process of annealing is investigated. It is crucial to consider the annealing temperature carefully, as very high temperatures can lead to the formation of sub-micron voids around grain boundaries, which increase resistance to free electron motion. Therefore, the annealing experiments in this study are performed close to the recovery and recrystallization temperatures that have been reported previously for cold-sprayed Cu coatings [7,12,23].

For successful implementation of CuCr coatings in VIs, they need to demonstrate similar breakdown strength in electric fields as conventional CuCr composites. Breakdown strength and arc erosion modes have been extensively studied for traditional CuCr composite materials [8,9,21,22]. However, these properties remain unknown for CuCr coatings, thus becomes the primary objective of present evaluation.

2.2 Materials and Methods

2.2.1 Powder Feedstock Preparation

Cr powder with particle sizes of ≤150µm (99.8% purity, AEE, PA, USA) and Cu powder with particle sizes of ≤45µm (99.9% purity, AEE, PA, USA) were utilized for this study. As-received Cr powder was sieved using a benchtop sieve to achieve a particle size of ≤45µm. Subsequently, the sieved Cr powder was dried in a convection oven at 70ºC for 8 hours. To produce feedstock 'X' used in the cold-spray process, a mixture was created by combining 55% of the stock Cu powder and 45% of the sieved Cr powder (≤45µm) by mass. The blending process was carried out in a tumble mixer, which rotated at a speed of 60rpm for 2 hours. On the other hand, feedstock 'Y' to produce PSI samples, was prepared by mixing 20% Cu powder and 80% Cr powder (with particle sizes ≤150µm) by mass, in a tumble mixer rotating at 60rpm for 2 hours.

2.2.2 Cold-Spray of Cu-Cr Coatings

100x100x12.5mm sized Multipurpose 110 Copper bars (McMaster Carr, IL, USA) were used as substrates. All substrates were ground using 400 grit silica paper and cleaned with IPA (99.5% pure, Fisher Scientific, USA) prior to deposition. In-house developed cold-spray system was used to produce CuCr composite coatings with feedstock ‘X’ and deposition parameters used are listed in Table 2.1. Two coatings were deposited by varying the main gas pressures, at 2.25 MPa (sample name CuCrA) and 3.45 MPa (sample name CuCrB). The coating samples CuCrA &

CuCrB were cut into 50x50x12.5mm coupons for annealing and further analysis. Details for current cold-spray setup and experiment descriptions can be found in earlier studies [13]. Deposition efficiency of the coatings was calculated (using eq. 2.1) by weighing the un-deposited powder (Wrp) in the powder feeder, weight of the coatings (Wc) not including the substrate and total powder wt. (Wp).

$$Deposition\ Efficiency = \frac{(Wc - Wrp)}{Wp} \times 100 \tag{2.1}$$

Substrate	Copper
Stand off	10 mm
Powder feed rate	10 g/min
Main gas Pressure	CuCrA 2.25 MPa
	CuCrB 3.45 MPa
Carrier gas Pressure	0.7 MPa
Process Temperature	500ºC
Carrier Gas	N_2

Table 2.1 Parameters of cold spraying

2.2.3 CuCr Composites with PSI Method

Powder feedstock 'Y' was filled in a machined SS316 mold having a diameter of approximately 40mm and compacted in a hydraulic press. Pressed Cu-Cr green compact was then placed in a graphite crucible along with pure Cu bar, which approximately exceeds the porosity in the green compact, and heated in a vacuum furnace. Heating was carried out for 2 hours, until the excess Cu bar placed on top of the green compact completely infiltrated into the pores of Cu-Cr skeleton forming a dense composite. After furnace cooling, the infiltrated sample was machined

to remove excess un-infiltrated copper from the top surface of PSI sample. The composite processing parameters are listed in Table 2.2. Finally, the PSI sample was then cut approximately into 30x30x5 mm coupons using a wet saw equipped with a silica blade for further tests and analysis.

Compaction Pressure	127 MPa
Sintering Temperature	925ºC
Sintering Time	1 Hour
Infiltration Temperature	1250ºC
Infiltration Time	2 Hours

Table 2.2 Parameters for Press-Sinter-Infiltration

2.2.4 Annealing of CuCr Coatings

Both cold-sprayed samples, CuCrA and CuCrB, were heated in a tube furnace (Lindberg MPH, MI, USA) at temperatures of 200ºC and 425ºC respectively for 1.5 hours each and allowed to cool down to <80ºC before removing from the furnace. Ar+5%H2 (UHP, Metrogas Welding, MI, USA) gas flowing at 250 sccm was used for all annealing experiments.

2.2.5 Microstructure and Elemental Analysis

Using a wet saw, the coating samples were cut perpendicular to the deposition surface and the PSI samples were cut axially, to reveal the sample cross-section and were prepared for analysis using standard metallurgical methods. The microstructures of the samples were observed by SEM (S-2600N, Hitachi Ltd., NY, USA) in backscattered electron (BSE) mode. Accelerating voltage of 20kV, emission current of 100μA and working distance of 15.4 mm was used for imaging. The energy dispersion spectrum detector (EDS) attached to the SEM was used to investigate the Cu and Cr content of the samples. Higher magnification (>3kx) images of the samples were taken using Tescan Mira SEM at an accelerating voltage of 20kV, at a WD of ~15mm and in BSE mode.

2.2.6 Residual Stress Measurements

The residual stress for each of the samples was measured using a Rigaku Ultima IV X-ray Diffractometer by the sin2Ψ technique. 2θ peaks for Cu (220) phase were measured at 5 negative Ψ angles, ranging between 0° and 34°, in steps of 6º~8° intervals. At each tilt angle, diffraction intensity was recorded for diffraction angle 2θ=74° using Cu K-alpha radiation at 40kV and 40mA power settings. Other parameters used for recoding the diffraction intensity are: step size of 0.05° and dwell-time of 2s. The in-plane normal stresses were measured along the direction parallel to the coating surface.

2.2.7 Microhardness Measurement

Microhardness of the samples was measured on the polished cross-sections of the samples using a Vickers microhardness tester (Duramin-5, Struers, Ltd, Kyoto, Japan) under a load of 300 gf applied for 20 seconds. The average of 10 readings made across each of the samples was used as an indicator for the microhardness.

2.2.8 Electrical Resistivity Measurements

The resistivity of the samples was measured using 4-point probe technique as described in [24]. A hand-held probe with S=1mm tip spacing (Type B, Jandel, UK) connected to a reversible current source (#6220, Keithley, OR, USA) and a nanovoltmeter (#2182A, Keithley, OR, USA) was used for all measurements. Each measurement is an average of 1000 voltage values (measured across tip 2-3 in fig 2.1) obtained by alternating DC current of 100mA between probe tip 1 and 4. For each of the samples, the resistivity was calculated as an average of 3 measurements made along the x- axis, y-axis, and diagonal of the x-y plane on the surface at the center of the samples. Each resistivity measurement was initially recorded for 50mA, 75mA and 100mA current, and 100mA was selected for final measurements as the variability was less than 0.1%.

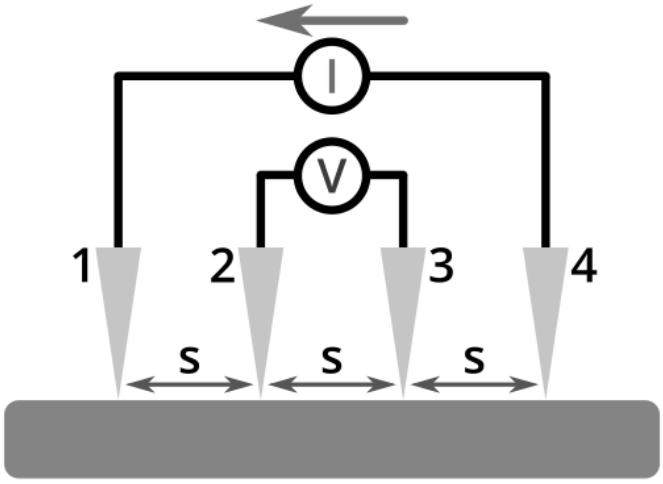

Figure 2.1 4-point probe resistivity measurement

2.2.9 EBSD Images

A Joel JSM-7800FLV SEM coupled with an Oxford NordlysMax² EBSD detector was used for microstructure measurements on the cold sprayed coatings. A 25kV electron signal was used with a high beam intensity. A working angle of 70° and 8.74Hz acquisition rate as used. Coatings were examined over an area of ~400µm2. The EBSD scans were later cleaned and processed using Oxford AztecHKL analysis software. Patterns only with >80% hit rate were mapped. Multiple areas were analyzed for different coatings and best scans have been reported. Indexing of phases was done by importing crystallographic information adapted from the ICSD database.

2.2.10 Vacuum Arc Tests

The vacuum breakdown tests were conducted in a UHV vacuum chamber modified to accommodate a moving anode and a fixed cathode. A RC-power circuit connected to 0-12kV DC voltage source was used as arching source. This circuit was built with 16µF capacitance, charge resistance of 8kΩ and discharge resistance of 1kΩ; its illustration can be found in earlier studies [8,9,15]. Prior to the arching tests, each of the samples were polished using 0.3µm alumina suspension (Allied High Tech. Products Inc., CA, USA), and washed in IPA (99.5% pure, Fisher Scientific, USA) and distilled water. The cleaned samples were dried at 45°C for 4 hours before

installing in the vacuum chamber. After measuring the surface roughness, each individual sample was fixed inside the vacuum chamber and acted as cathode. Above the cathode, a pure tungsten rod with a radius of 3 mm and a tip angle of 20° was used as an anode. The anode was fixed onto a movable electrode holder connected to a high accuracy (0.5μm) and high resolution (0.0001mm) micrometer (Mitutoyo, MI, USA), which can support linear motion (up-down) for manipulating and measuring the distance between the electrodes. Prior to start of the test, the chamber was evacuated to 3×10−3 Pa and a steady flow of 10sccm of Ar was introduced to maintain the chamber pressure consistent across multiple tests. For each breakdown cycle, the capacitor circuit was charged to 8.5 kV (Ui), anode was then lowered downwards until an arc was developed between the electrode gap. The distance between two electrodes (d) was recorded to compute the breakdown strength (UBD=Ui/d). The real-time voltage discharge curve was recorded by an oscillograph (Fluke, Digi-key, USA) and the arc-life can be directly measured by the current waveforms of the discharge. Then the anode was retracted to home position and the above procedure was repeated for 100 breakdown cycles for each tested sample to record its vacuum breakdown behavior.

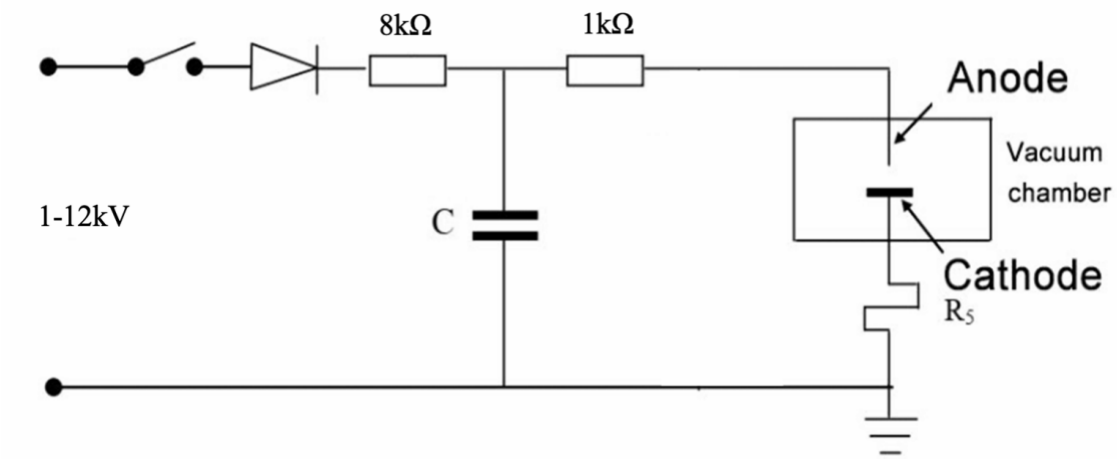

Figure 2.2 Vacuum arc discharge setup

2.2.11 Arc-erosion Profile Imaging

Prior to breakdown tests, the surface roughness of the samples was measured using a surface profilometer (Mitutoyo SJ201, MI, USA). An average of 3 readings is reported for the Ra and Rz values. After conducting 100 breakdown tests as describe above, the samples were subjected to 400 additional breakdown cycles. The arc-erosion profiles after a total of 500 arcing cycles were imaged by a SEM (S-2600N, Hitachi Ltd., NY, USA) in secondary electron (SE) mode. Accelerating voltage of 20kV, emission current of 100μA and working distance of 27 mm was used for imaging. The erosion depth was measured using a profilometer.

2.3 Microstructure & Properties of Cold-Sprayed CuCr Coatings

2.3.1 Cold Spray of CuCr Coatings

Microstructure & compositional analysis of cold-sprayed coatings are shown in fig. 2.3 and fig. 2.5(a) respectively. It is apparent that un-deformed Cr particles are surrounded by highly deformed and elongated Cu particles, forming composite CuCr coatings. Cu phase, which has higher ductility compared to Cr, requires lower impact velocities for plastic deformation and serves as a matrix phase that encapsulates Cr particles. It is observed that the CuCrB sample, deposited at a higher main gas pressure compared to CuCrA, exhibits lower interfacial voids and displays an improved Cr/Cu interphase (fig.2.3 (b,d)). Increase in deposition pressure leads to higher particle impact velocities, resulting in enhanced deformation of the Cu phase and improved bonding between particulate boundaries. This reduces void formation and contributes to higher microhardness and electrical conductivity of the coatings.

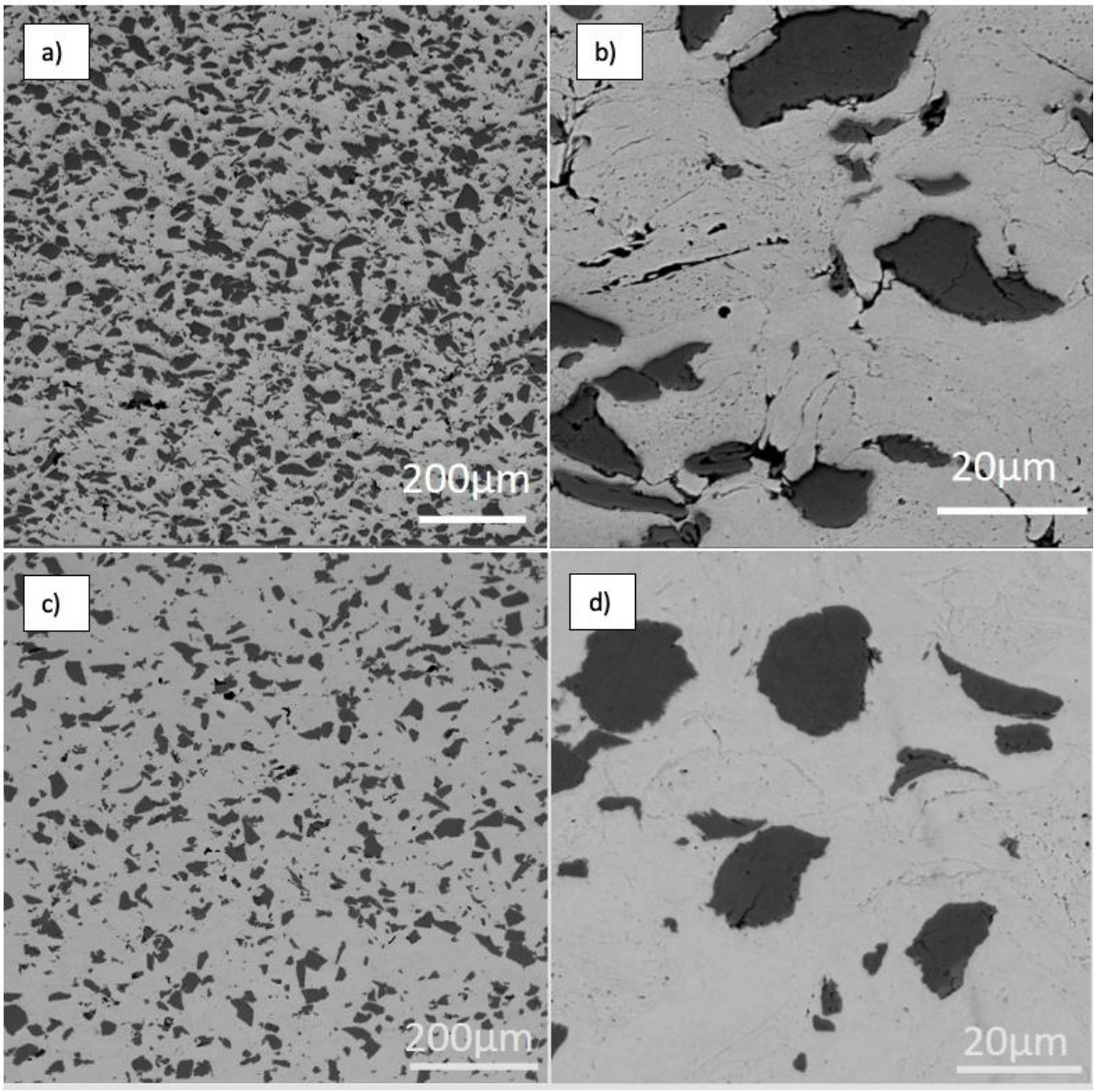

Figure 2.3(a) CuCrA Coatings at 300x, (b) CuCrA Coating at 3kx (c) CuCrB Coatings at 300x, (d) CuCrB Coating at 3kx

Both CuCrA and CuCrB samples exhibited a deposition efficiency of approximately 55%. However, the relative Cr retention within the coatings differed between the two samples. CuCrA, deposited at a lower main gas pressure, demonstrated higher Cr retention with an average of 28% by weight. On the other hand, CuCrB exhibited slightly lower Cr retention at 21% by weight. Decreased Cr content in cold-sprayed coatings compared to the initial feedstock composition is consistent with findings from previous studies [7,13,19], and this observation can be attributed to

several factors. Firstly, particle size influences the critical velocity, which affects the deposition efficiency of the cold spray coatings [6]. Even with similar-sized Cu and Cr particles in the feedstock mixture, the density difference between them can lead to different velocities in the deposition jet. Lower-density Cr particles may outpace the Cu particles at the exit of the cold spray nozzle, resulting in a higher Cr-to-Cu particle ratio before reaching the deposition surface [7]. If the deposition parameters favor higher Cr-Cr particle interactions, rather than favorable Cu-Cr or Cu-Cu interactions at the deposition front, then Cr particles tend to rebound from the coating. In the case of CuCrB, deposited at higher pressure, the higher velocities of the Cr particles compared to CuCrA can lead to increased unfavorable Cr-Cr interactions, leading to lower Cr retention. Secondly, inhomogeneity in the powder distribution of the feedstock can inadvertently introduce smaller-sized Cr particles into the feed stream, increasing the likelihood of unfavorable Cr-Cr interactions. It has been reported that the retention efficiency of Cr decreases as the feedstock powder size decreases [19]. A third reason for lower Cr retention efficiency could be the presence of hard Cr particles in the feedstock with higher kinetic energies. These particles can exert unfavorable effects such as tamping, which can affect the overall cold-spray ability of the powder mixture [1]. The final Cr retention in the coatings plays a significant role in determining the electrical resistivity. A higher Cr content in the CuCr coatings results in increased resistivity. Balancing the Cr content while maintaining adequate inter-particulate bonding and low void content is important to optimize both the electrical resistivity and overall performance of the coatings.

2.3.2 Comparison of Cold-Sprayed Coatings with PSI Samples

Obtained microstructure of PSI sample is shown in figure 2.4(a), and exhibits notable differences compared to the cold-sprayed coatings. Use of larger-sized Cr powders (≤150μm) in

the PSI technique enhances the infiltration of molten Cu into the green compact and reduces overall porosity [22]. But it leads to more exposed Cu phase with non-uniform Cr distribution. On the contrary, use of smaller Cr powders (≤45μm) for cold-sprayed coatings increases the dispersion uniformity of Cr phase within the coatings (as shown in fig 2.4). In the PSI process, the infiltrated Cu matrix undergoes solidification with a slow cooling rate in a vacuum environment. The slower cooling rates promotes growth of coarser Cu grains, resulting in improved electrical conductivity compared to the cold-sprayed CuCr coatings (resistivity plotted in figure 3(a)).

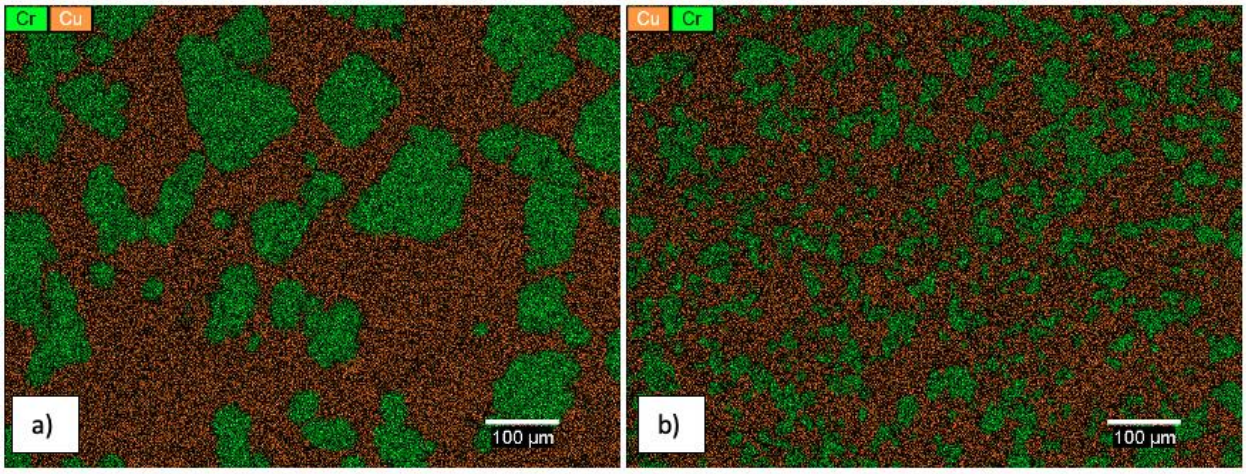

Figure 2.4 (a) CuCr PSI sample with 33 wt% Cr, (b) CuCrA Coating with 28 wt% Cr

PSI process also produces more coherent Cu/Cr interface connectivity as nucleation of molten Cu is facilitated on the Cr particulate phase in the green compact. During the vacuum infiltration, approximately 1.2 wt% Cr can diffuse into the molten Cu, and by implementing slow cooling, any dissolved Cr will precipitate out without adversely affecting electrical conductivity [15,18]. The PSI sample contains about 33 wt% Cr, which is slightly higher than the samples obtained using cold spray. Residual stresses in the Cu phase of the samples are measured and shown in figure 2.5(b). Cold-sprayed coatings exhibit high compressive stresses in the Cu phase because of plastic deformation of the spray material. This is indicated by the negative slope of the Sin2Ψ plot. In contrast, the Cu phase in the PSI samples remains relatively un-stressed due to the

slower kinetics of the vacuum infiltration technique. High compressive residual stresses in cold-sprayed coatings are commonly observed and aligns with findings from other studies [26,27]. Inherent compressive stresses in cold-sprayed coatings contribute to improved microhardness of the CuCr samples, even with lower Cr content compared to PSI samples. Cold-sprayed coating with comparable Cr content to the PSI sample has higher resistivity. This can be attributed to the higher levels of voids and inferior bonding between Cu and Cr phases in cold-sprayed coatings.

2.3.3 Effect of Annealing on Cold-Sprayed Coatings

Annealing was carried out on the as sprayed CuCrA and CuCrB samples to relieve the residual compressive stresses and improve their electrical resistivity. Heat treatment temperatures of 200°C and 425°C were chosen based on previous studies, which reported the onset of recrystallization of cold-sprayed Cu coatings at 200°C and negative effects of void assemblage at temperatures above 500°C [12,17]. Fig. 2.6(a) depicts the change in resistivity of CuCrA and CuCrB samples with annealing. For CuCrA, the resistivity decreases by 6% at 200°C and by 38% at 425°C. Similarly, for CuCrB, the resistivity decreases by 2% at 200°C and 11% at 425°C. Fig. 2.6(b) presents the changes in microhardness of the samples with annealing temperatures. It is observed that the hardness decreases for both CuCrA and CuCrB samples as the annealing temperature increases. This reduction in hardness is expected as annealing leads to the recovery of internal stresses and recrystallization of the material, resulting in a strain-free and softer microstructure. It is noteworthy that CuCrA, having comparable Cr content to the PSI sample, shows similar electrical resistivity after annealing at 425°C. However, its hardness is significantly lowered.

At lower annealing temperatures of 200ºC, marginal improvement in resistivity and reduction in hardness is primarily attributed to the recovery from deposition stresses and the onset

of recrystallization. At higher annealing temperatures of 425ºC, there is larger improvement in resistivity indicating that interconnection of sub-micron voids occurs. At high temperatures, some voids are gradually eliminated through chemical diffusion. Thereafter, enhancing the contact between adjacent Cu-splats and Cu/Cr interfaces, leading to improved electrical conductivity [12]. Furthermore, annealing between 300-500°C, results in reduction of total pore area within the coatings, and increase in grain size and homogeneity. Which further improves the electrical conductivity of the material but at the expense of hardness [17,25]. For cold-sprayed coatings, annealing at 425°C relieves residual compressive stresses completely, this is evident from the Sin2Ψ plots (fig.2.7(a)). In the present study, Sin2Ψ plots are only used as indicators of stresses rather than for direct comparison of absolute values. Both CuCrA and CuCrB samples displayed similar reduction is stresses after annealing.

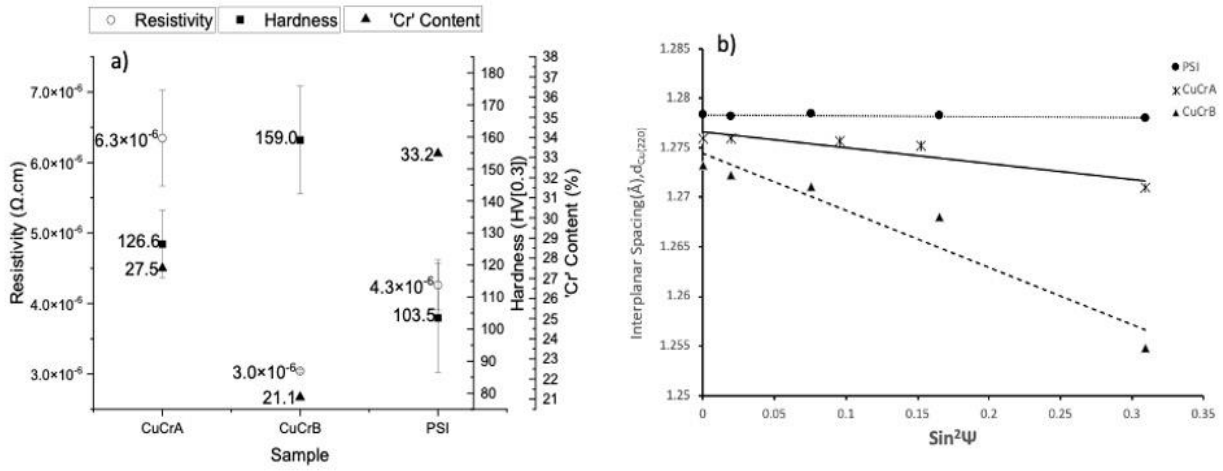

Figure 2.5 Comparison for (a) Cr%, Resistivity & Vickers Hardness of the samples (b) Residual stress comparision

EBSD micrographs for CuCrB sample at different annealing temperatures are shown in fig.2.8. When compared to CuCrA, the EBSD micrographs for CuCrB have lower zero solutions (<10%) and higher C.I for Kikuchi bands, due to better etching uniformity resulting from lower microstructural porosity. In general, high dispersion of Cr phase in the current samples made it challenging to obtain a good surface finish required to obtain reliable EBSD maps. Typically, cold-

sprayed coatings exhibit elongated grains in the direction of particle impact, with some recrystallized sub-grains formed at particle(splat)-particle(splat) boundaries due to deformation plastic flow [5,12]. From fig.6, it is observed that the sample annealed at 200°C has some elongated grains, while the sample annealed at 425°C exhibits finer equiaxed grains. Although the grain sizes appear similar for both annealed samples (Fig. 2.7(b)), the 425°C annealed sample displays slightly higher percentage of finer grains. Grain sizes within the cold-sprayed Cu phase are influenced by the dislocation density. Previous studies have shown that Cu coatings with high dislocation density can exhibit resistance to annealing below 200°C [25].

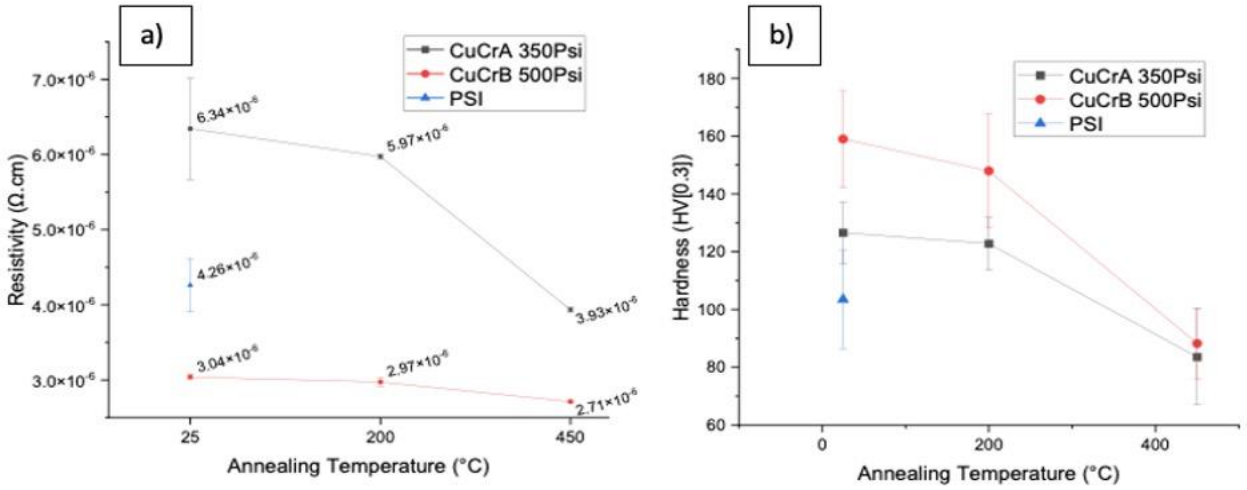

Figure 2.6 Effect of annealing cold-sprayed samples (a) Measured resistivity (b)Vickers Hardness

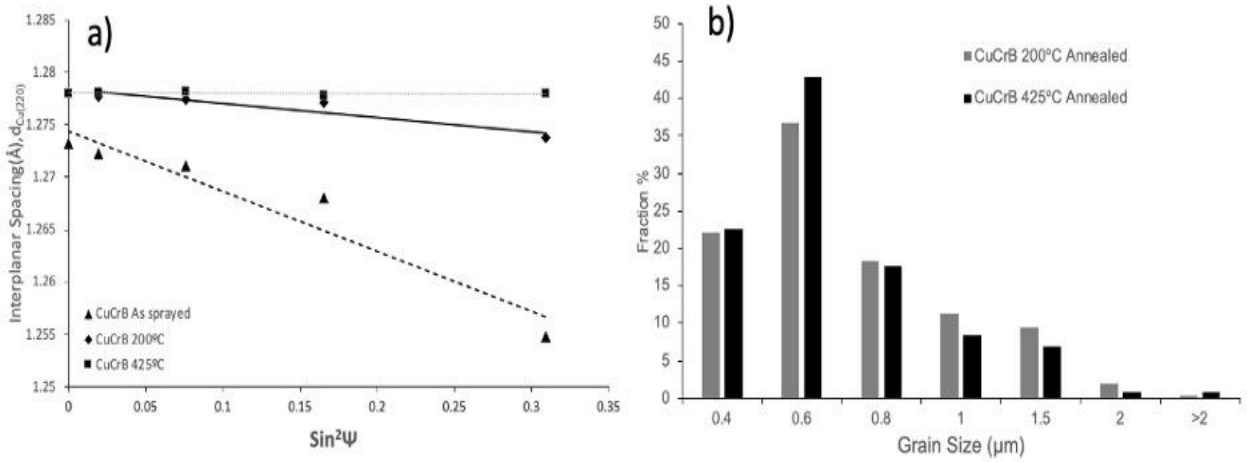

Figure 2.7 Effect of annealing on residual stress of cold-sprayed CuCrB samples (a) Residual stress (b) Grain Size

However, the current samples demonstrate a reduction in hardness and lower grain orientation spread (GOS) of 2.4° at 200ºC, which is close to the recrystallization criterion observed for Cu(~2º) [28]. Furthermore, the 425°C annealed sample exhibits significantly lower hardness and an average GOS of 1.9°, indicating a higher fraction of recrystallized grains compared to the 200°C annealed sample.

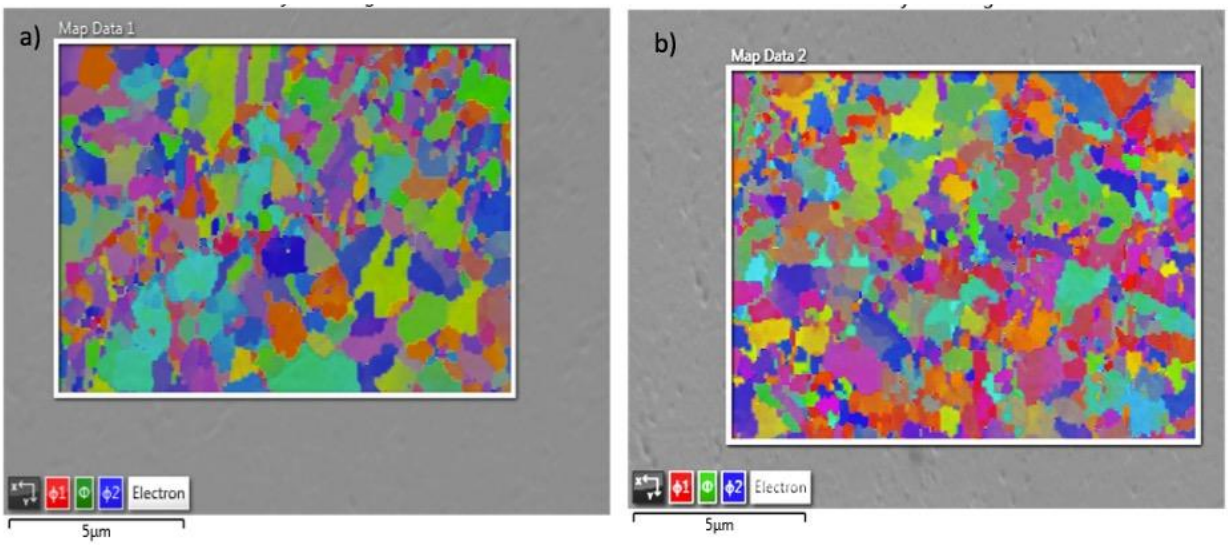

Figure 2.8 EBSD for CuCrB coating annealed at (a) 200°C (b) 425°C

2.4 Breakdown Characteristics of Cold-Sprayed CuCr Coatings

2.4.1 Vacuum Breakdown Strength of Cold-Sprayed CuCr Coatings

Previous studies using similar test setups have signified that breakdown strength stabilizes after conditioning the test samples [3,15,22]. Therefore, 25 conditioning cycles were performed on each test sample prior to recording breakdown voltages for 100 consecutive tests. Fig. 2.9 displays the breakdown probability plotted against breakdown strength for CuCr coatings and PSI sample. Breakdown strength (UBD50) for 50% probability was obtained for each of the samples from fig.2.9 and used as a metric for comparison of breakdown characteristics. PSI sample, which had the highest Cr content, exhibited higher breakdown strength compared to the cold-sprayed coatings (table 2.3). While the difference in breakdown strength between CuCrA and CuCrB

samples can be attributed to the difference in Cr content, the larger difference between the cold-sprayed samples and the PSI sample cannot be solely explained by this factor. Breakdown in a vacuum is influenced by the electric field across the electrodes and the work function (Ø) of the electrode materials. Surface properties, such as roughness, particulate inclusions, adsorbed gases, and oxide impurities, also affect the breakdown performance. However, since the samples were ground and polished before the breakdown tests, the influence of surface oxide on breakdown strength is expected to be negligible. Surface roughness measured (table 2.3) for the tested samples did not show a significant difference among them, eliminating roughness as a significant contributing factor to the large difference in UBD50 values. The difference in UBD50 between cold-sprayed coatings and the PSI sample can be attributed to two factors. First, the presence of entrapped gases between deformed particulate grains and inter-particulate voids. Second, the difference in distribution of Cr phase in cold-sprayed coatings when compared to PSI sample. Both factors can alter the microscopic enhancement factor (β), which affects the electric field and breakdown behavior. Additionally, Cr (Ø=4.5eV) has a slightly lower work function compared to Cu (Ø=4.65eV), making it a potential site for electron emission at a given electric field. The scattered distribution of the Cr phase in the cold-sprayed samples could lead to more emission sites according to Fowler and Nordheim equation, thereby increasing the probability of breakdown occurrence (B1, B1 are constants, U is the applied voltage, d is the electrode separation distance, Ie field emission current, Ae emission area) [22].

$$i_e = \frac{A_e . B_1 . (\beta U)^2}{\phi d^2} \times e^{\left(\frac{-B_2 \emptyset^{1.5} d}{\beta U}\right)} \tag{2.2}$$

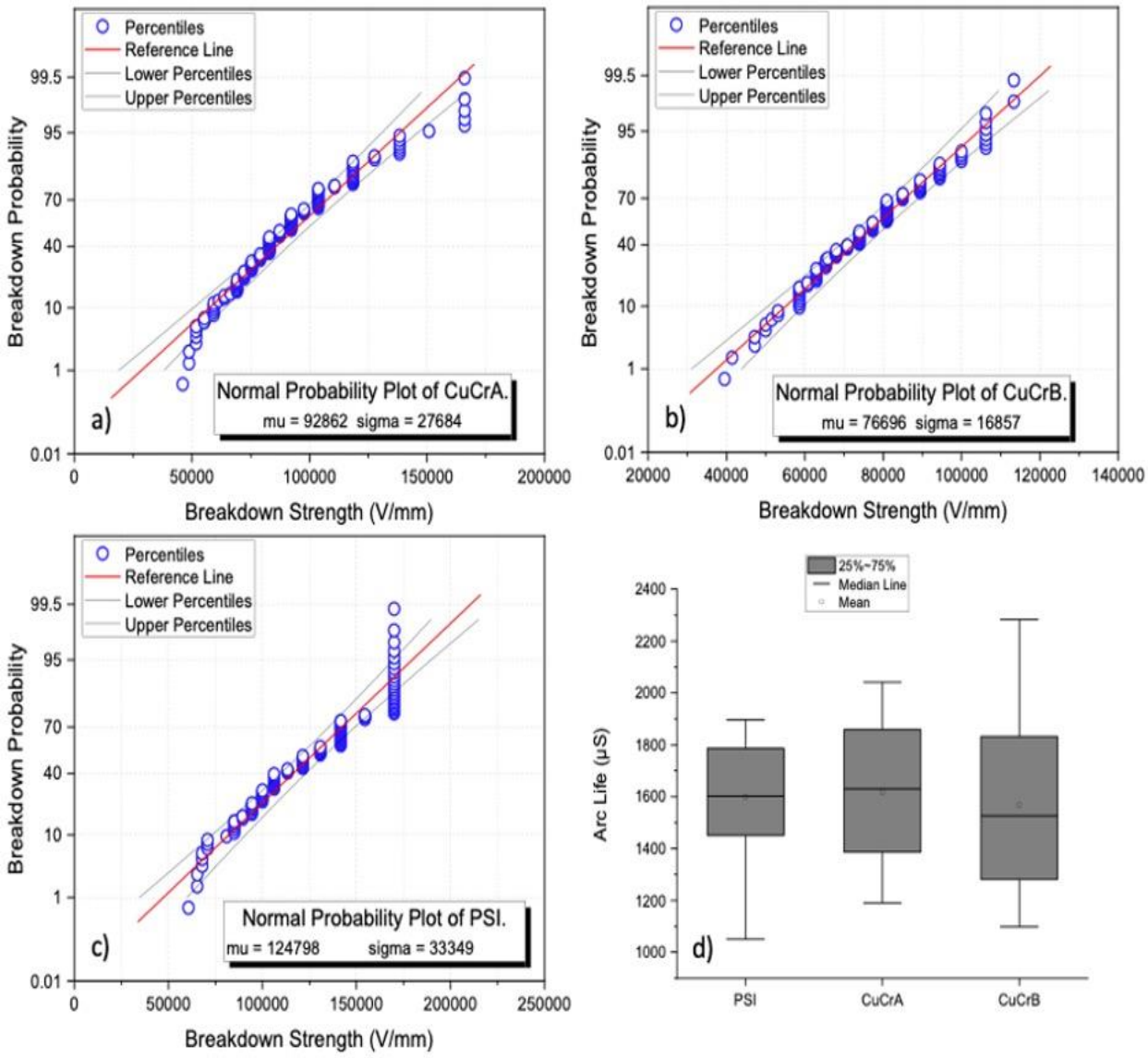

Figure 2.9 Breakdown strength measured for (a) CuCrA (b) CuCrB (c) PSI (d) Comparison of arc-life on samples

Sample	Ra (µm)	Rz (µm)	U_{BD50} (V/mm)	Erosion Depth, d_e (µm)
CuCrA	0.33	1.66	$8.7x10^4$	66.2
CuCrB	0.18	1.25	$7.7x10^4$	55.5
PSI	0.24	1.65	$1.2x10^5$	46.5

Table 2.3 Surface roughness, Breakdown strength & Erosion depth measurements

2.4.2 Effect of Annealing on Breakdown Strength of CuCr Coatings

Figures 2.10(a&b) show the breakdown strength for 100 arcing cycles of annealed cold-sprayed coatings. Both as-sprayed CuCrA and CuCrB coatings exhibited improvements in breakdown strength after annealing. Annealing reduces the number of emission sites on a cathode surface at a given voltage, leading to improved breakdown strength [22,25]. The breakdown strength for CuCrA increased by 4% at 200°C and by 11% at 425°C, while CuCrB showed an increase of 12% at 200°C and 16% at 425°C. CuCrA coating annealed at 425°C achieved a breakdown strength comparable to the PSI samples. The slight difference can be attributed to marginally lower Cr content in the coating compared to the PSI samples.

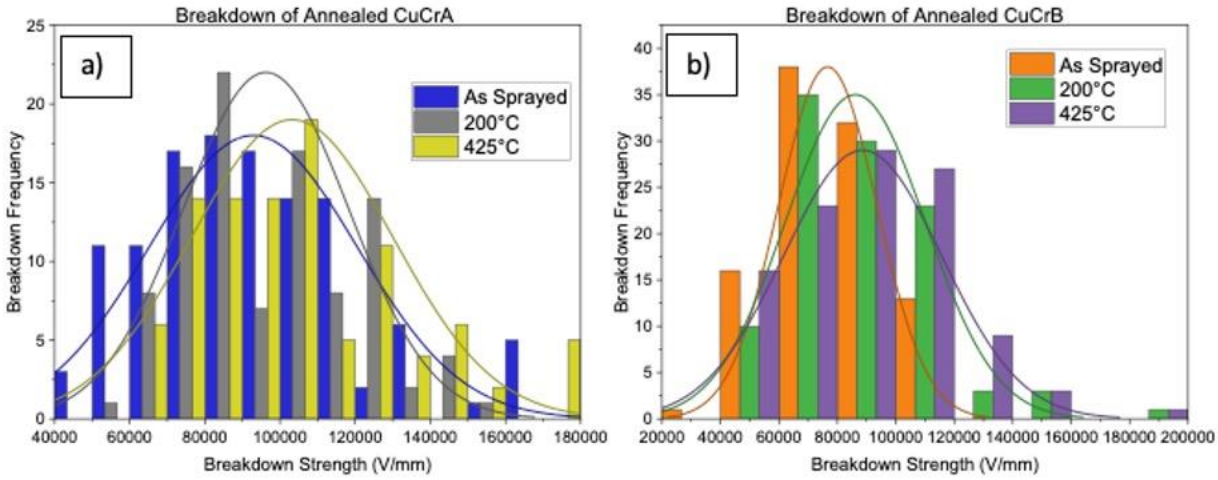

Figure 2.10 Normal distribution of breakdown strength of annealed cold-sprayed samples (a) CuCrA (b) CuCrB

2.4.3 Comparison of Arc-life during Breakdown Tests

After a breakdown event occurs, a vacuum arc is formed on the sample surface and traverses on a random path before extinction due lack of external electric field. Shorter arc-life on an electrode surface suggests that any arc formed during VI operation is quickly quenched. The average arc-life measured for 25 arcing cycles on each of the samples is presented in fig. 2.9(d). CuCrB sample has the lowest average arc-life, followed by the PSI sample and CuCrA respectively. The arc-life is primarily dependent on thermal conductivity of the electrode material

[22,24]. Higher thermal conductivity can facilitate efficient distribution of heat at the arcing surface, aiding in its extinction. At any given temperature 'T', the relationship between electrical resistivity (ρ) and thermal conductivity (λ) of a sample is determined using Wiedwermann-Franz law (eq 2.3, where 'k' is the Boltzmann's constant and 'e' is the electronic charge). Electrodes with lower resistivity tend to have higher thermal conductivity which results in shorter arc-life. The as-sprayed CuCrB sample deposited at higher main gas pressures, has improved particulate bonding and lower Cr content. As a result, has the lowest resistivity and exhibits shorter arc-life. On the contrary, CuCrA sample exhibits highest resistivity, due to weaker particulate interfaces and voids, which hinders the heat flow contributing to higher arc-life. The differences in resistivity and particulate nature of the CuCr coatings can contribute to deviations in arc-life behavior compared to PSI samples.

$$\lambda\,(T)\,\rho\,(T)=(k/e)^2T \tag{2.3}$$

2.4.4 Comparison of Arc-mode & Arc-erosion profiles

Arc-erosion performance of CuCr contacts is largely related to the content and distribution of Cr phase, and vapor pressure of the electrode material [11,14, 22, 24]. In CuCr electrodes, the Cr phase, which has a lower work function (Ø), is observed to be the preferential phase for vacuum arc attachment [8,18,22]. This observation is consistent with the PSI sample, where the erosion is primarily initiated within the Cr phase and due to the retrograde motion of the cathode spot moves to the Cu phase (fig.2.11). However, for the cold-sprayed coatings, the interface between Cu and Cr phases exhibits equal or higher erosion compared to the Cr phase (fig.2.12). This phenomenon can be attributed to the presence of interfacial voids, which create areas of low thermal transfer and hot zones. Erosion on the surface is caused by several moving cathode spots, resulting in material evaporation, splashing, and boiling. From the fig. 2.13, it is noticeable that the severe arc-

eroded sites are in the center directly facing the pointed anode end, where a crater with rough microstructures is formed by re-solidified electrode material. The overall erosion profiles on PSI and cold sprayed samples exhibit some differences. PSI sample has a more constricted erosion zone, forming a smaller erosion crater with a depth of 46.5 μm. The constricted erosion zones (Type-2) are typically observed with CuCr materials with lower impurities and homogenous Cr distribution (fig. 2.13(c)). In contrast, for cold-sprayed samples, the erosion zones appear to be larger and scattered (fig. 2.13(a&b)). The diffused erosion zones (Type-1) can be attributed to impurities such as voids and scattered distribution of Cr phase, creating more arc attachment sites. The erosion depths of cold-sprayed coatings are proportionate to the Cr content within the coatings and are greater than that of the PSI sample (table 2.3). The surface area of erosion zone for CuCrA and CuCrB are similar, despite having different Cr contents. This indicates that the arc erosion on cold-sprayed coatings is predominantly influenced either by weaker interfacial bonding of the Cu/Cr interface or higher porosity.

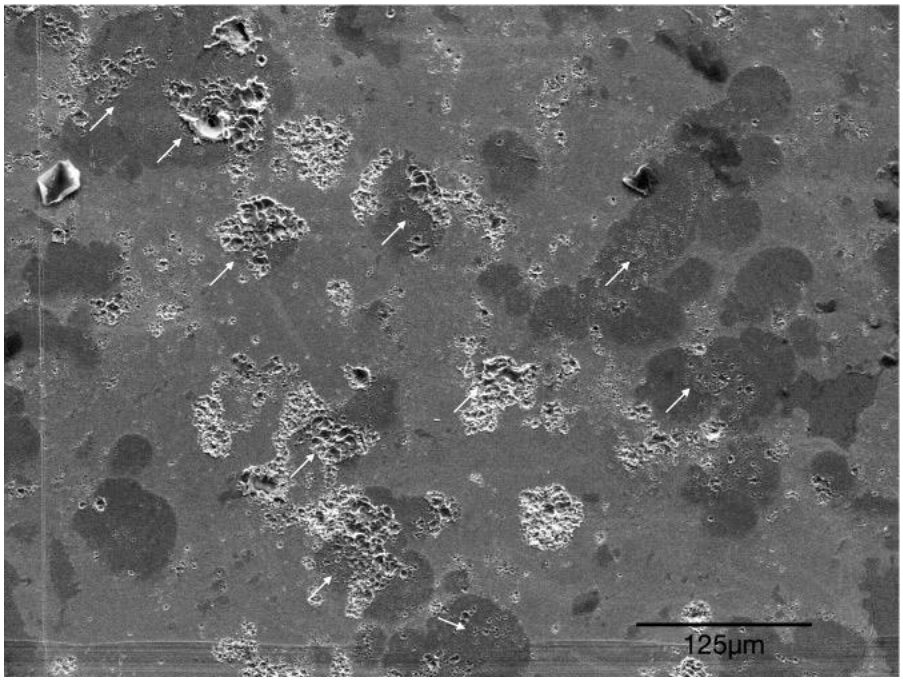

Figure 2.11 Arc-erosion profile on PSI showing preferential cathode spot attach sites on Cr Phase at 200x

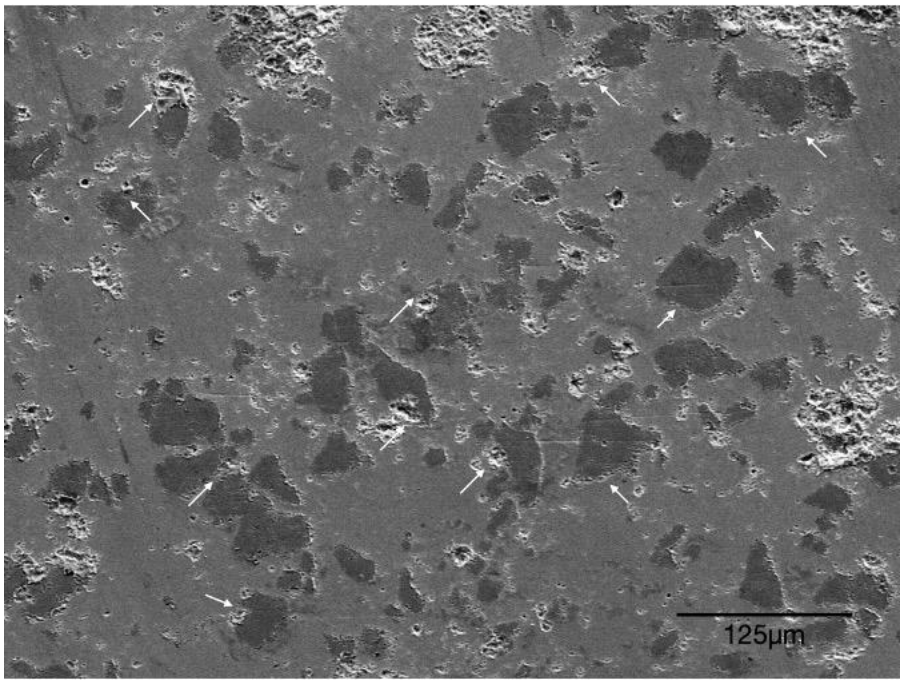

Figure 2.12 Arc-erosion on CuCr coating showing preferential cathode spot attach sites on Cu/Cr interphase at 200x

2.5 Discussion on Breakdown Performance of CuCr coatings

The comparable breakdown strength reported for traditional CuCr samples using a similar test setup is approximately 2.8×10^5 V/mm [15]. However, the breakdown strength obtained for the PSI sample is 1.25×10^5 V/mm, which is lower. This difference observed is due to setup marginality and higher chamber pressure compared to the previous study. Higher chamber pressures reduce the vacuum dielectric capability. In the present study, a steady flow of 10sccm Ar gas was used for all breakdown tests to eliminate setup variations that potentially impact measurement deviations. Therefore, we use the PSI sample as a relative benchmark to compare the cold-sprayed CuCr breakdown performance. Repeat breakdown tests were conducted to increase the confidence in the measured values, and the results showed a variation within 3% (see table 2.4 below). It has been observed that with annealing CuCr coatings we can consistently achieve comparable breakdown performance as traditional PSI samples.

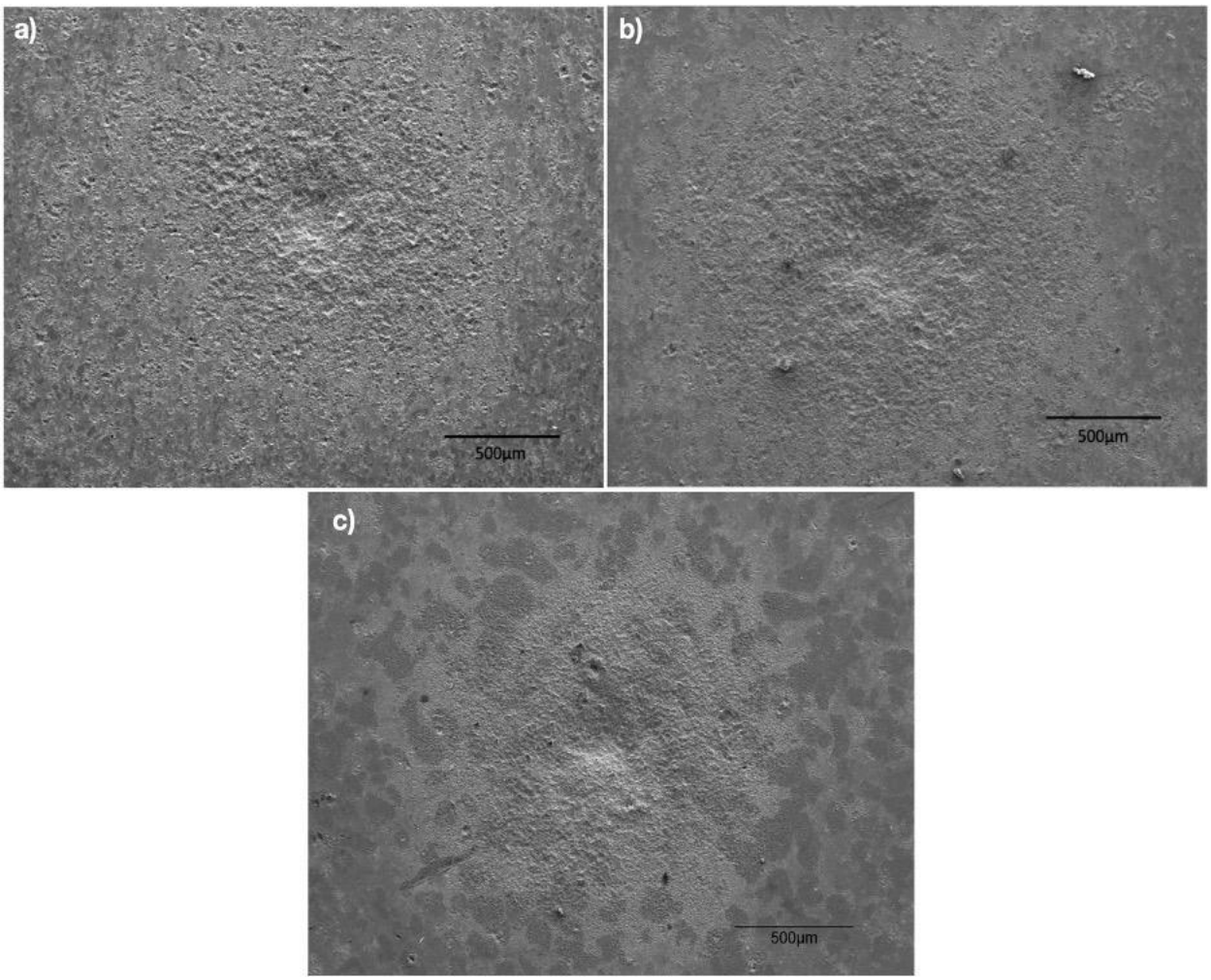

Figure 2.13 Arc-erosion profile on CuCrA after 500 breakdown cycles at 50x (a)CuCrA (b) CuCrB (c) PSI sample

Sample	**Test 1: $U_{(BD50)}$ (V/mm)**	**Test 2: $U_{(BD50)}$ (V/mm)**
PSI	$1.25x10^5$	$1.19x10^5$
CuCrA 450ºC annealed	$1.05x10^5$	$1.08x10^5$

Table 2.4 Breakdown strength for repeat tests

The difference in breakdown performance between the as-sprayed CuCr coatings and the PSI sample can be attributed to void content, distribution of the Cr phase, and final Cr retention within the coatings. These factors can lead to variations in the microscopic enhancement factor and increase electron emission sites, which affect the breakdown performance. One approach to

improve breakdown strength of CuCr coatings is to increase the deformation of the Cu phase during deposition, to improve particulate bonding within the coating and reduce the void content. However, it is to be noted that increasing deposition pressures may lead to a reduction in the Cr content, which adversely affects the breakdown strength. Our previous experience with cold-sprayed CuCr coatings [13,19] has shown that there can be a variability of approximately 5% in Cr retention, even when using the same feedstock. This variability can be attributed to the powder size distribution within the feedstock. Therefore, it is important to attain a balance between Cu phase deformation and Cr content by optimizing the deposition parameters and improve the coating's performance.

It is also important to consider the resistivity and thermal conductivity of the CuCr coatings, as these factors significantly influence arc erosion performance. The particulate nature and high deformation of the Cu phase in CuCr coatings results in higher resistivity and lower thermal conductivity compared to PSI samples. This characteristic can contribute to longer arc life and increased surface erosion during VI operations. Though we can achieve lower resistivity by annealing the CuCr coatings, it is essential to carefully select the annealing temperature to avoid compromising on hardness, as certain applications for VI require high hardness to prevent excessive erosion or contact sticking [22].

2.6 Conclusion

The primary objective of the study was to establish vacuum breakdown characteristics of the cold-sprayed CuCr coatings and compare them to bulk CuCr composites. To this end, the samples required for the tests were prepared by CGDS and PSI techniques. The properties which influence breakdown performance, such as electrical resistivity and microhardness, were measured for the test samples. Finally, the CuCr coatings were subjected to breakdown tests in a vacuum

chamber to determine breakdown strength, establish arc-life and arc-erosion profile. Then established breakdown characteristics were compared with PSI sample to estimate the performance of the CuCr coatings for electrical contact materials in VIs. Additionally, annealing process was performed to relieve residual compressive stresses in cold-sprayed coatings and improve the electrical conductivity.

The conclusions drawn from this study are summarized below:

- For cold-spray deposition of CuCr coatings, the choice of deposition pressure affects the particle impact velocity, deformation of the Cu phase, and the resulting bonding between particulate phases. Higher deposition pressure results in better interfacial bonding, with reduced voids, and improved electrical conductivity of the coatings. However, at higher deposition pressures of 3.45MPa, the Cr retention in the coatings is reduced to 21%. This is due to higher unfavorable Cr-Cr interactions during deposition. Highest Cr retention for cold sprayed coatings was 28% at a deposition pressure of 2.25MPa. CuCr coatings deposited at lower pressure, exhibited high interfacial porosity which resulted in very high electrical resistivity. The measured microhardness and electrical resistivity for sample CuCrA, deposited at 2.25 MPa, is [Hv] 127(±11) and $6.3x10^{-6}(\pm 0.67x10^{-6})$ Ω.cm, respectively. For the sample CuCrB, deposited at 3.45 MPa, microhardness increases to [Hv] 159(±17) and electrical resistivity reduces to $3x10^{-6}(\pm 0.07x10^{-6})$ Ω.cm.
- In contrast to cold-sprayed CuCr coatings which contain un-melted Cu phase, PSI samples were produced by molten Cu infiltration into green compact, resulting in microstructures with 33% Cr content and improved Cu/Cr interface with low inherent porosity. PSI sample exhibited 46% lower electrical resistivity compared to CuCrA with comprable Cr content. However, the resistivity of CuCrA reduced significantly after annealing the coating at

425°C for 1 hour, making it comparable to PSI sample. Annealing at higher temperature reduced the hardness of CuCrA [Hv] to 84 (±17). As sprayed CuCr coatings have high compressive residual stresses, which contribute to higher hardness when compared to PSI sample ([Hv] 104 (±17)).

- Breakdown strength (U_{BD50}) for CUCr coatings is measured to be $8.7x10^4$ V/mm for CuCrA and $7.7X10^4$ V/mm for CuCrB. This difference is primarily due to variation in Cr content. On the contrary, PSI sample had much higher U_{BD50} $1.25x10^5$ V/mm, the differences in breakdown strength observed between the cold-sprayed coatings and the PSI sample can be attributed to factors such as the presence of entrapped gases, void content and differences in Cr phase distribution. U_{BD50} for annealed cold-sprayed coatings improved significantly, CuCrA coating annealed at 425°C achieved a breakdown strength of $1.05x10^5$ V/mm, comparable to the PSI samples. The slight difference in U_{BD50} can be attributed to marginally lower Cr content in the coating when compared to the PSI samples.
- The arc-life was lowest for CuCrB followed by PSI and CuCrA respectively. The sample having higher conductivity had the shortest arc-life. the resistivity and thermal conductivity of the electrode materials play a significant role in determining the arc-life. Lower resistivity and higher thermal conductivity tend to result in shorter arc-life, while higher resistivity and lower thermal conductivity can lead to longer arc-life. The differences in resistivity and bonding characteristics between the CuCrA, CuCrB, and PSI samples contribute to variations in their arc-life behavior.
- Arc-erosion profile on cold-sprayed coatings was diffused and spread over a larger area compared to constricted erosion profile on the PSI sample. This observed difference is due to impurities such as voids, higher distribution of Cr phase, which create more arc

attachment sites for cold-sprayed samples. For CuCr coatings, the preferential site for arc attachment was at the interface between Cu/Cr and in pure Cr phase. On the contrary, for PSI sample the preferential attachment site was just in the lower dielectric strength Cr phase. The erosion depths for both cold-sprayed coatings are similar to each other but higher than PSI sample. Effects of annealing on arc-life and erosion depth are not investigated in the present study and needs to be further evaluated.

References

[1] X. Chu, H. Che, C. Teng, P. Vo, S. Yue, A multiple particle arrangement model to understand cold spray characteristics of bimodal size 316L/Fe powder mixtures, Surface and Coatings Technology. 381 (2020) 125137. https://doi.org/10.1016/j.surfcoat.2019.125137.

[2] H. Assadi, F. Gärtner, T. Stoltenhoff, H. Kreye, Bonding mechanism in cold gas spraying, Acta Materialia. 51 (2003) 4379–4394. https://doi.org/10.1016/S1359-6454(03)00274-X.

[3] C. Zhang, Z. Yang, Y. Wang, B. Ding, Cathode spot propagation on the surface of amorphous, nanocrystalline and crystalline Cu60Zr28Ti12 cathodes, Physics Letters A. 318 (2003) 435–439. https://doi.org/10.1016/j.physleta.2003.09.050.

[4] T.I. Awan, A. Bashir, A. Tehseen, S. Bibi, Chapter 7 - Electrons in nanostructures, in: T.I. Awan, A. Bashir, A. Tehseen (Eds.), Chemistry of Nanomaterials, Elsevier, 2020: pp. 179–206. https://doi.org/10.1016/B978-0-12-818908-5.00007-X.

[5] R. Nikbakht, H. Assadi, K. Jahani, M. Saadati, B. Jodoin, Cold spray deformation and deposition of blended feedstock powders not necessarily obey the rule of mixture, Surface and Coatings Technology. 424 (2021) 127644. https://doi.org/10.1016/j.surfcoat.2021.127644.

[6] F. Raletz, M. Vardelle, G. Ezo'o, Critical particle velocity under cold spray conditions, Surface and Coatings Technology. 201 (2006) 1942–1947. https://doi.org/10.1016/j.surfcoat.2006.04.061.

[7] X. Wu, X. Zhou, H. Cui, X. Zheng, J. Zhang, Deposition Behavior and Characteristics of Cold-Sprayed Cu-Cr Composite Deposits, J Therm Spray Tech. 21 (2012) 792–799. https://doi.org/10.1007/s11666-012-9755-0.

[8] C. Weichan, L. Shuhua, Z. Xiao, W. Xianhui, Y. Xiaohong, Effect of Fe on microstructures and vacuum arc characteristics of CuCr alloys, International Journal of Refractory Metals and Hard Materials. 29 (2011) 237–243. https://doi.org/10.1016/j.ijrmhm.2010.10.012.

[9] C. Weichan, L. Shuhua, Z. Xiao, W. Xianhui, Y. Xiaohong, Effect of Mo addition on microstructure and vacuum arc characteristics of CuCr50 alloy, Vacuum. 85 (2011) 943–948. https://doi.org/10.1016/j.vacuum.2011.02.001.

[10] X. Chu, F. Meng, Z. Chi, H. Aydin, Y.-K. Wei, P. Vo, W. Sun, R. Huang, S. Yue, Effects of powder characteristics and mixing powders on cold sprayability and corrosion properties of tantalum coatings, Surface and Coatings Technology. 426 (2021) 127763. https://doi.org/10.1016/j.surfcoat.2021.127763.

[11] W. Guan, J. Yuan, H. Lv, T. Zhu, Y. Fang, J. Liu, H. Wang, Z. Li, Z. Tang, W. Yang, Homogeneous arc ablation behaviors of CuCr cathodes improved by chromic oxide, Journal of Materials Science & Technology. 81 (2021) 1–12. https://doi.org/10.1016/j.jmst.2020.10.083.

[12] B. Yu, J. Tam, W. Li, H.J. Cho, J.-G. Legoux, D. Poirier, J.D. Giallonardo, U. Erb, Microstructural and bulk properties evolution of cold-sprayed copper coatings after low temperature annealing, Materialia. 7 (2019) 100356. https://doi.org/10.1016/j.mtla.2019.100356.

[13] Y. Chang, P. Mohanty, N. Karmarkar, M.T. Khan, Y. Wang, J. Wang, Microstructure and properties of Cu–Cr coatings deposited by cold spraying, Vacuum. 171 (2020) 109032. https://doi.org/10.1016/j.vacuum.2019.109032.

[14] XIU Shi-xin et.al., Microstructure and properties of CuCr contact materials with different Cr content, Transactions of Nonferrous Metals Society of China. 21 (2011) s389–s393. https://doi.org/10.1016/S1003-6326(11)61612-9.

[15] C. Zhang, Y. Wang, Z. Yang, Y. Guo, D. Bingjun, Microstructure and properties of vacuum induction melted CuCr25 alloys, Journal of Alloys and Compounds. 366 (2004) 289–292. https://doi.org/10.1016/j.jallcom.2003.07.001.

[16] T. Stoltenhoff, C. Borchers, F. Gärtner, H. Kreye, Microstructures and key properties of cold-sprayed and thermally sprayed copper coatings, Surface and Coatings Technology. 200 (2006) 4947–4960. https://doi.org/10.1016/j.surfcoat.2005.05.011.

[17] Parameter study influencing thermal conductivity of annealed pure copper coatings deposited by selective cold spray processes, Surface and Coatings Technology. 206 (2012) 2316–2324. https://doi.org/10.1016/j.surfcoat.2011.10.010.

[18] C. Zhang, Z. Yang, Y. Wang, B. Ding, Properties of Nanocrystalline CuCr50 Contact Material, Advanced Engineering Materials. 7 (2005) 1114–1117. https://doi.org/10.1002/adem.200500139.

[19] Y. Chang, J. Wang, P. Mohanty, M.T. Khan, L.N.U. Rehman, L. Shan, C. Fu, J. Wang, The Effect of Cr Particle Size on Cr Deposition Efficiency during Cold Spraying, J. of Materi Eng and Perform. 31 (2022) 4060–4067. https://doi.org/10.1007/s11665-021-06486-6.

[20] X.-J. Ning, J.-H. Jang, H.-J. Kim, The effects of powder properties on in-flight particle velocity and deposition process during low pressure cold spray process, Applied Surface Science. 253 (2007) 7449–7455. https://doi.org/10.1016/j.apsusc.2007.03.031.

[21] W.F. Rieder, M. Schussek, W. Glatzle, E. Kny, The influence of composition and Cr particle size of Cu/Cr contacts on chopping current, contact resistance, and breakdown voltage in vacuum interrupters, IEEE Transactions on Components, Hybrids, and Manufacturing Technology. 12 (1989) 273–283. https://doi.org/10.1109/33.31434.

[22] P.G. Slade, The Vacuum Interrupter: Theory, Design, and Application, CRC Press, 2020.

[23] F.J. Wei, B.Y. Chou, K.Z. Fung, S.Y. Tsai, Thermomechanical properties of cold-sprayed copper coatings from differently fabricated powders, Surface and Coatings Technology. 434 (2022) 128128. https://doi.org/10.1016/j.surfcoat.2022.128128.

[24] F.M.Smits, "Measurement of Sheet Resistivities with the Four-Point Probe", The Bell System Technical Journal 37, 711-718 (1958)

[25] Calla, E.; McCartney, D. G.; Shipway, P. H. Effect of Deposition Conditions on the Properties and Annealing Behavior of Cold-Sprayed Copper. *J Therm Spray Tech* **2006**, *15* (2), 255–262. 10.1016/j.actamat.2007.03.021.

[26] Moridi A. Fatigue Behavior of Cold Spray Coatings: The Effect of Conventional and Severe Shot Peening as Pre-/Post-Treatment.

[27] Yeom, H.; Dabney, T.; Pocquette, N.; Ross, K.; Pfefferkorn, F. E.; Sridharan, K. Cold Spray Deposition of 304L Stainless Steel to Mitigate Chloride-Induced Stress Corrosion Cracking in Canisters for Used Nuclear Fuel Storage. *Journal of Nuclear Materials* **2020**, *538*, 152254.

[28] Field, D. P.; Bradford, L. T.; Nowell, M. M.; Lillo, T. M. The Role of Annealing Twins during Recrystallization of Cu. *Acta Materialia* **2007**, *55* (12), 4233–4241. 10.1016/j.actamat.2007.03.02.

[29] McCune, R. C.; Donlon, W. T.; Popoola, O. O.; Cartwright, E. L. Characterization of Copper Layers Produced by Cold Gas-Dynamic Spraying. *J Therm Spray Tech* **2000**, *9* (1), 73–82. 10.1361/105996300770350087.

Chapter 3 Investigation of CuCr Films Produced by Co-deposition Using VAPD

Abstract

In this chapter, Vacuum Arc Plasma Deposition (VAPD) for producing CuCr thin films is investigated as an alternative to overcome the limitations of cold-sprayed coatings. One of the limitations of cold-spray coatings is the difficulty in increasing the Cr content beyond a certain threshold due to process constraints. Additionally, cold-spray coatings have larger micron-sized Cu and Cr phase sizes within the films as opposed to sub-micron phases in VAPD. Historically, VAPD has been used to produce coatings with thicknesses of around few tens to several hundred microns, in contrast to the higher deposition rates and mm-thick coatings achievable with cold spraying. For this study, CuCr films are co-deposited using independent Cu and Cr cathodes with in-house built two-cathode deposition system. The films are deposited at three different Cr/Cu cathode current ratios, to understand the impact of ion flux on the final composition and microstructure of the films. Finally, the chapter reports on the residual stresses and nanohardness measurements for the obtained films.

3.1 Introduction

Vacuum arc plasma deposition or cathode arc spray technique utilizes a high current, low voltage arc between two metallic electrodes (anode and cathode) to evaporate material of interest for depositing thin films. When the arc strikes on the cathode (or target material), a highly energetic emitting area called the cathode spot originates (spot size in the order of 1–10μm), and violently vaporizes the cathode material. As a resultant of very high current density, part of the vaporized material transitions into dense ionized plasma which expands rapidly into vacuum and is directed towards the substrate where it gets deposited. The generated cathode spots move randomly across the surface of the target with very high velocities, and in presence of an axial magnetic field these

spots can be steered (direction of **-j x B**) on the surface of the cathode ensuring uniform rate of erosion over time. If a reactive gas (such as nitrogen or oxygen) is introduced during the evaporation process, dissociation and ionization will occur during interaction with material plasma and a compound film will be deposited [21-30].

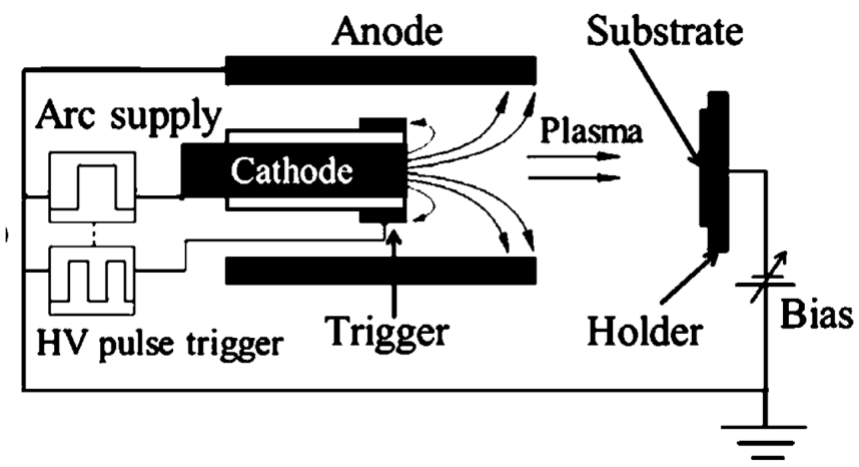

Figure 3.1 Schematic of VAPD system (vacuum system not shown)

A typical unfiltered VAPD system is shown in fig. (3.1), it consists of a cathode (or target material) which acts as a plasma source for deposition, an anode, high voltage pulsed ignition system to initiate the arc on the cathode, focusing coils (magnetic coils) for confining the movement of cathode spots and a high voltage bias power supply for accelerating the ionized target material onto the substrate. After generation of plasma at non-stationary cathode spots, the plasma containing ionized cathode material expands into the interelectrode space. During this expansion, various system parameters can be controlled to manipulate the properties of the plasma. Factors such as ion density, particle temperatures, streaming velocity, and ion charge state distribution are some process parameters that can be employed to obtain various microstructures for the thin films. The plasma density and ion acceleration are influenced by pressure gradients and the coupling between electrons and ions, which is controlled by cathode arc currents. The plasma density in absence of external magnetic field can be estimated using: $n = C\, I_{arc}/r^2\, Cos^{\alpha}\vartheta$, where Iarc is the

arc current, C is the cathode erosion rate, r is the distance from the cathode spot , ϑ is the angle normal to cathode surface for plasma expansion and α is the plasma plume shape factor (typically >1). Therefore, it is evident that the plasma density increases with arc current and reduces moving away from the cathode spot [2,20,21].

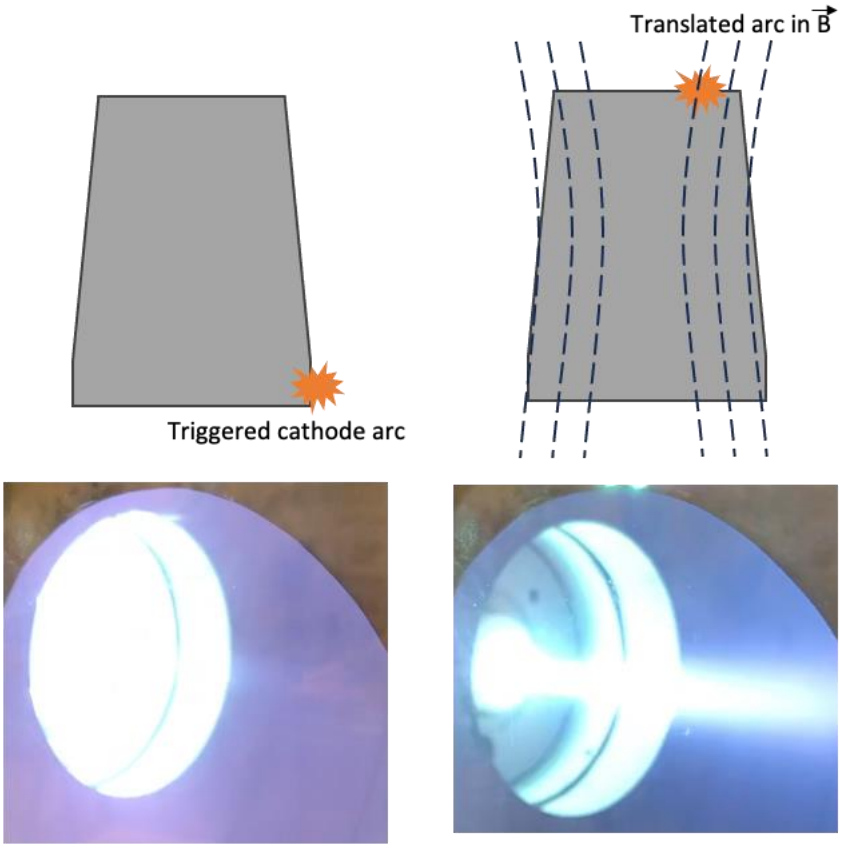

Figure 3.2 Depiction of axial magnetic field used in current VAPD setup (a,c) location of triggered arc on cathode and plasma without magnetic field, (b,d) Movement of the arc to the cathode surface and constricted plasma in axial magnetic field

Presence of a magnetic field will strongly influence plasma expansion. In the deposition configuration shown in fig 3.2, the magnetic field lines intersect the cathode surface axially and propel the triggered arc & cathode plasma towards the substrate. Triggered arc on the cathode moves towards the surface following acute angle rule in an axial magnetic field. Application of axial filed impedes the motion of magnetized ions and electrons in the direction perpendicular to the field lines. Therefore, the dense plasma does not transition by rapid expansion into vacuum,

thereby minimizing loss of particle temperatures. In contrast to other thin film techniques such as thermal evaporation and DC sputtering, VAPD offers the advantage of achieving a high degree of material ionization, typically ranging from 30% to 100%. Additionally, moderately high ion kinetic energies, typically between 10-100 eV, can be attained. This capability of VAPD makes it highly desirable for applications that require high film density and thicknesses [20, 23, 26].

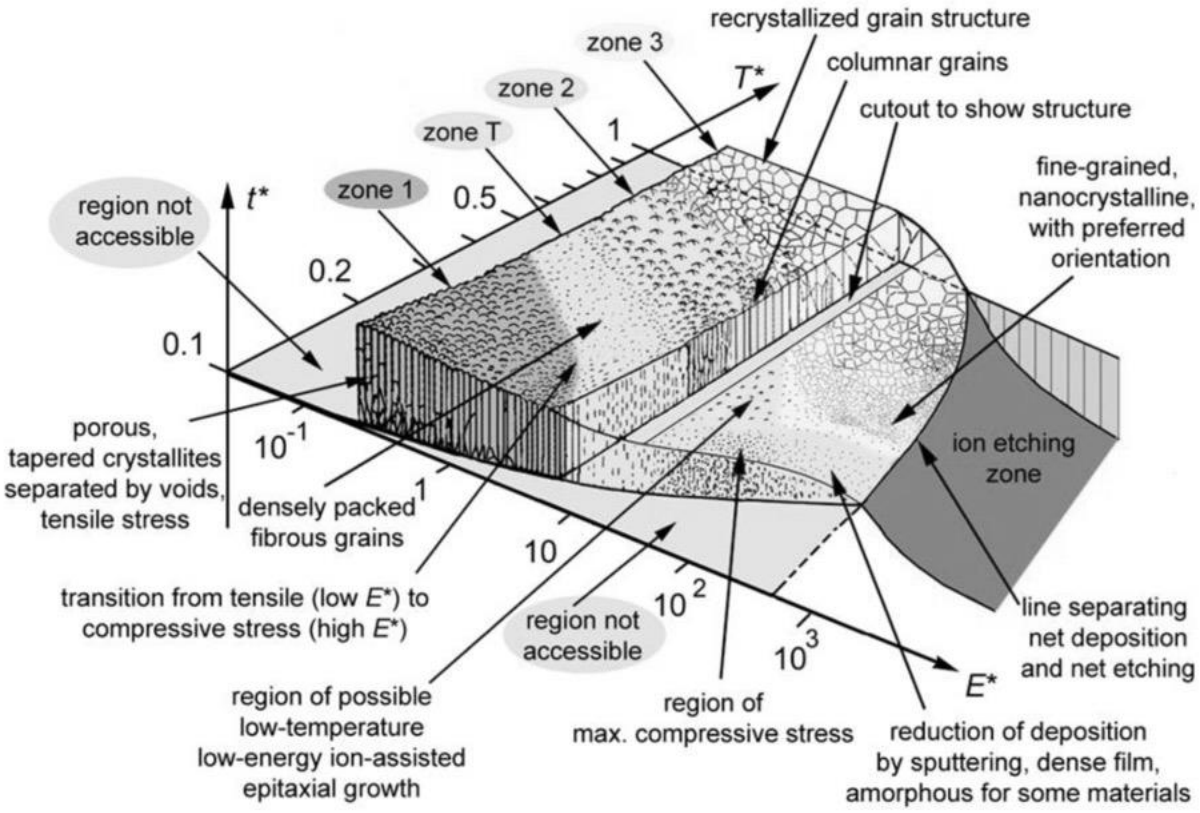

Figure 3.3 Structure-Zone model developed to predict the microstructures of thin films [26]

Figure 3.3 provides a summary of the progression of attainable microstructures with various deposition techniques. The illustration captures all microstructures attainable from low-energy thermal evaporation to high-energy VAPD techniques as a function of homologous temperature (ratio of substrate temperatures and melting temperature of material) with respect to time and ion energies achieved during deposition. VAPD stands out in terms of the high ion energies it can achieve and this has several effects on the deposited coatings. Firstly, they

contribute to the formation of dense microstructures in the films. Secondly, they help mitigate the presence of porous fibrous grain structures that are characteristic of thermal evaporation methods. Lastly, they minimize the formation of low-density columnar grain structures typically obtained with DC sputtering techniques [23,26].

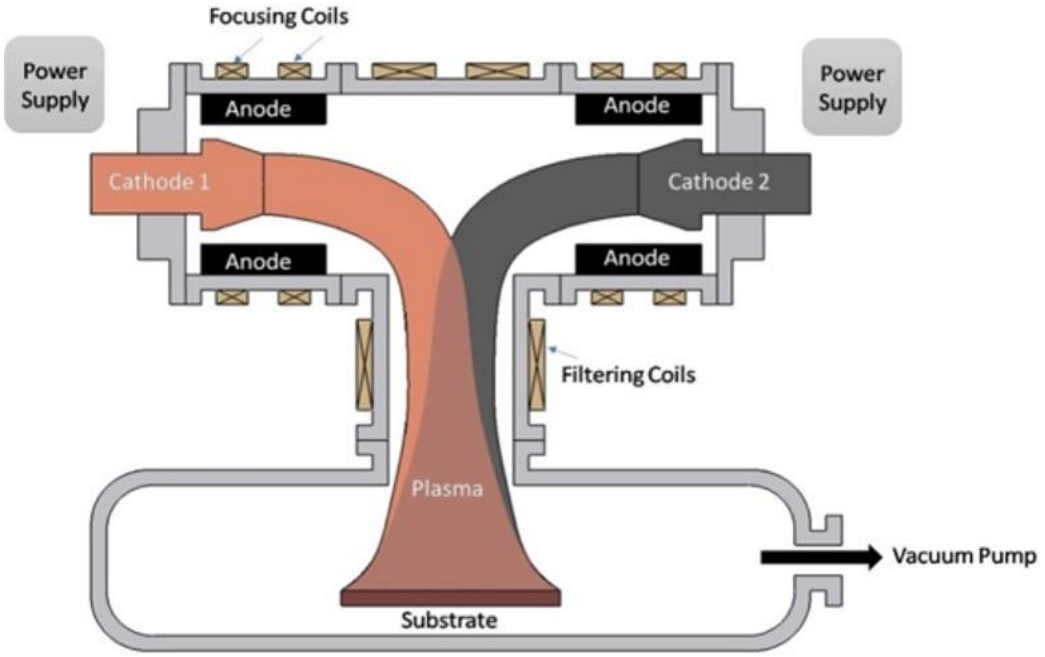

Figure 3.4 Schematic of a Co-Deposition VAPD Torus System for Depositing Multi-Phase Coatings

The combination of high material ionization, moderately high ion kinetic energies, and the resulting nanocrystalline coatings make VAPD a promising technique for various applications in which film density, thickness, and fine-grained microstructures are desired. One disadvantage for this process is simultaneous production of small liquid droplets at the cathode spot commonly referred to as macroparticles. These macroparticles have sizes ranging from 0.2 to 100μm and produce inferior films as they hinder the adhesion of coating inter-layers. To filter the macroparticles some setups adapt filtering magnetic coils and a torus design as shown in fig. 3.4. Disadvantage of using filtering coils is that rate of deposition rate is drastically decreased and requires precise process tuning especially with co-deposition (depositing with two different targets

for alloy coatings). The production of macroparticles particles is inherently connected to the existence of non-stationary cathode spots. Pressure of resultant plasma at a cathode spot can be approximated using: $P_p \approx 2QC\ (I_{arc}/r^2)\mathrm{k}T_e$; where, Q is the mean ion charge state, C is the cathode erosion rate, k is Boltzmann constant, and T_e is the e^- temperature. For a given cathode, the arc current controls the plasma pressure on the cathode spot. Therefore, inclusion of macroparticles in the coatings can be limited to a certain degree by optimizing the current density on cathode and by using appropriate magnetic field to move the cathode spots (to control the erosion) during deposition [20-24].

In the current experiments, the magnetic field, substrate distance, voltage bias, and deposition pressure are fixed, and only the arc current on independent cathodes is varied for deposition. By depositing at different arc currents, the ion charge state and ion density reaching the substrate surface can be modified, leading to changes in the microstructure evolution during the co-deposition of Cu and Cr. However, at low arc currents (as used in the current study), the influence on the ion charge state is minimal, allowing for a focus on the plasma density reaching the substrate surface and its impact on microstructural evolution. [23]

3.2 Materials and Methods

3.2.1 Co-deposition of CuCr Films

The deposition process was conducted using an in-house built VAPD system, which is illustrated in figure 3.5(a). The vacuum chamber has dimensions of ø18” diameter and 36” length, and it is equipped with a water circulation system to maintain a chamber temperature of 40ºC during deposition. Desired vacuum level was achieved in two stages, a mechanical pump was employed to attain a rough vacuum of approximately $6\text{x}10^{-3}$ Torr and followed by the use of a diffusion pump to achieve a high vacuum level of around $4\text{x}10^{-6}$ Torr. The chamber incorporates a

custom gas flow system capable of injecting up to 50 sccm of argon gas for arc ignition and pressure control, as necessary. The figure 3.5(b) depicts a cross-section of the 'Bulat' cathode [2] configuration used in the setup. The cathode holder is designed to accommodate cathodes with diameters of up to 75mm and is water-cooled to maintain a temperature of 10ºC during the deposition process. The cathode is centrally located within an annular stainless steel (SS-316) anode. A triggering circuit, operating at a high voltage of 5kV and a frequency of 100kHz, is connected to SS-316 trigger installed at the trailing edge of the cathode. A DC magnetic coil, located concentrically on the anode, is connected to a regulated DC power supply capable of operating in current regulation mode within a range of 0-50V and 0-5A. To prevent metal vapors from entering the diffusion pump, a particle trap is included before the inlet of the pump to condense and trap any particles.

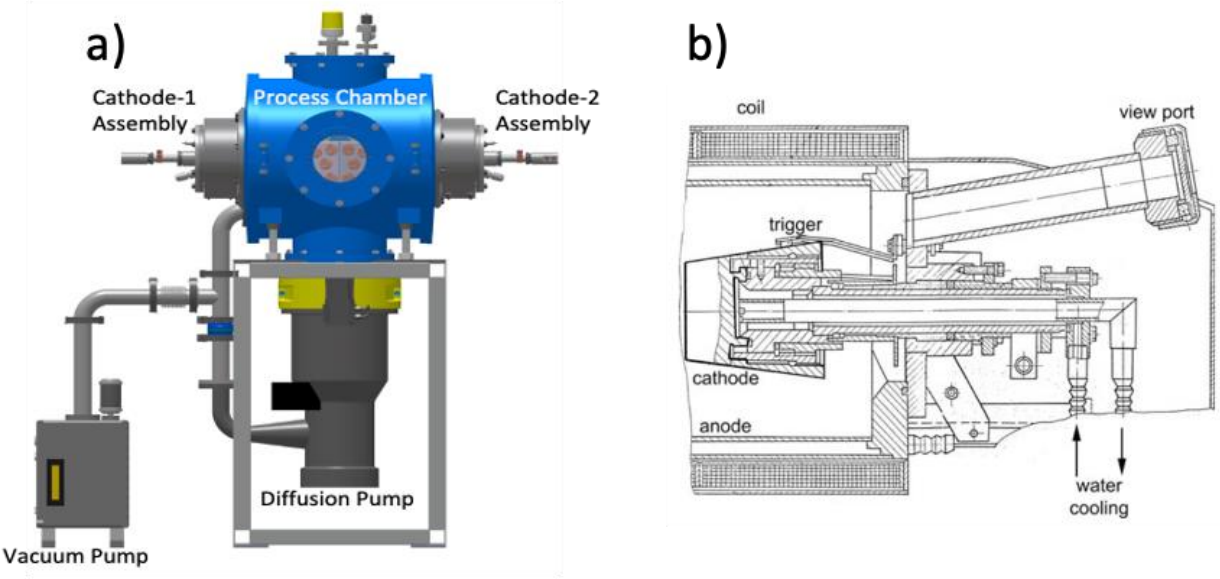

Figure 3.5 a) In-house assembled VAPD system b) Bulat cathode design used [2]

The Bulat cathode design used in the experiment is known for its simplicity and effectiveness in steering the arc on the cathode surface. Spot steering is achieved by employing an

external magnetic coil that generates an axial magnetic field symmetric to the conical cathode. When the arc is initiated, it follows the acute angle rule and moves towards the front face of the cathode, as depicted in the provided figure 3.2 (d). In all the experiments conducted, a magnetic current of 1.8A was utilized to generate the required magnetic field for arc steering.

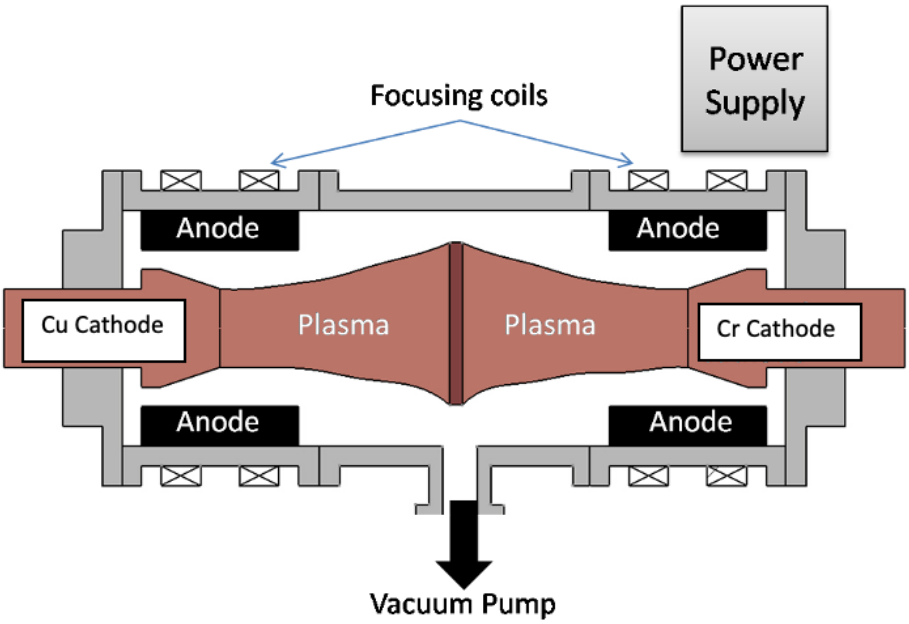

Figure 3.6 Current Co-deposition setup

For the co-deposition process, cathode assemblies were installed with consisting of a 99.99% pure 50mm diameter Cu target and a 99.99% pure 50mm diameter Cr target, on either end of the process chamber as shown in fig (3.6). The substrates used in the study were 2" in length, 2" in width, and 0.125" in thickness, made of SS-316. Prior to the deposition, the substrates were ultrasonic washed in deionized (DI) water followed by an ethanol rinse. The washed substrates were placed on a rotating holder positioned at a distance of 12" from the cathode and rotated at a speed of 30rpm throughout the process. The chamber was initially evacuated to a pressure of $6x10^{-6}$ Torr, and then a steady flow of 10 sccm of Ar gas was introduced into the chamber for arc ignition. Once the arc was successfully stabilized on the cathode, the chamber pressure stabilized at $2x10^{-5}$ Torr. Prior to the actual deposition, the substrates were subjected to a sputter cleaning process to

further remove surface contaminants and improve adhesion. Chromium ions (Cr+) were used for sputter cleaning using a bias voltage of -200V for 2 minutes, followed by a bias voltage of -500V for 3 minutes. After substrate sputtering, bias voltage was then kept constant at -20V during the deposition, while the arc current (I_{arc}) was varied as shown in Table 3.1 to produce different test samples.

Sample	Deposition Time, min	Chamber Pressure (Torr)	Bias Voltage, V	Arc Current, A Cr/Cu	Arc Voltage, V Cr/Cu	Mag. Coil Current, A Cr/Cu
CuCr A	120	$2x10^{-5}$	-20	90/60	20/23	1.8/1.5
CuCr B	120	$2x10^{-5}$	-20	60/110	20/23	1.8/1.5
CuCr C	120	$2x10^{-5}$	-20	90/90	20/23	1.8/1.5

Table 3.1 Co-deposition parameters

3.2.2 SEM Imaging and Compositional Analysis

Using a wet saw, the coating samples were cut perpendicular to the deposition surface to reveal the sample cross-section and were prepared for analysis using standard metallurgical methods. Final polishing was performed on the SEM samples using a vibratory machine filled with 100nm Al_2O_3 suspension (~pH 9) for 4 hours. The microstructures of the samples were observed by FE-SEM (JEOL JSM-7800FLV) in secondary electron and backscattered electron (BSE) mode. Accelerating voltage of 20kV, emission current of 1-10μA and working distance of 14-15 mm was used for imaging. The energy dispersion spectrum detector (EDS) attached to the SEM was used to investigate the Cu and Cr content of the samples.

3.2.3 XRD and Residual Stress Calculation

The crystallographic data for CuCr films was obtained using the Rigaku Miniflex X-ray diffractometer (XRD) operating at 30 kV and 15 mA. XRD patterns were recorded using Cu target (1.54Å) and scanned from 40° to 85° 2θ at a scan speed of 1°/min and 0.1° step size. Obtained patterns are processed in JADE software for analyzing the crystallographic data. Residual stresses within the thin films were obtained by measuring elastic lattice strains using the sin2ψ method using Rigaku Ultima IV diffractometer. 2θ peaks for Cr (211) phase were measured at 5 negative ψ angles, ranging between 0° and 34°, in steps of 8° intervals. At each tilt angle, diffraction intensity was recorded for diffraction angle 2θ=81.6° using Cu K-alpha radiation at 40kV and 40mA power settings. Other parameters used for recoding the diffraction intensity are: step size of 0.05° and dwell-time of 2 s. The in-plane normal stresses were measured along the direction parallel to the coating surface, and the residual stress was calculated using Youngs modulus (E) 248 GPa and the Poisson ratio (v) was 0.22 for Cr.

3.2.4 Nanoindentation Testing

The values of hardness were measured by using Hysitron Tribo-Indenter equipped with a Berkovich probe. Initially loads of 5 mN, 8mN and 15 mN were tested, and 8mN was selected for all films for comparison to limit the indentation depth <300nm. The loading rates were 20 mN/min with a 5s pause at peak load. The nanoindentation testing was repeated 5-8 times on the cross-section of each sample and then took the average as the final test value. Nanoindentation technique simultaneously measures load (F) and displacement (dh) to plot the load response curve for both loading and unloading phase of the test. The hardness (H) is calculated using H = F/A, where ‘F’ is the maximum force applied and ‘A’ is the measured indented area of the Berkovich

probe. The slope of the unloading curve is used to calculate contact stiffness (S), which is then related to the elastic modulus of the film (E).

3.3 Results and Discussion

3.3.1 Microstructure of VPD CuCr Coatings

In contrast to Cr thin films, there is limited literature on unfiltered Cu deposition using the VPD technique. As part of this study, an initial attempt was made to investigate Cu coatings under specific deposition conditions using current setup. Figure 3.7(b) shows the surface morphology of Cu deposited at $2x10^{-5}$ Torr pressure, 100A arc current, -20V substrate bias, and a deposition time of 15 minutes. The surface morphology confirms a 3D-island growth mechanism, indicating a stronger affinity between Cu atoms compared to Cu-substrate interaction. The surface reveals a highly porous morphology, indicating incomplete densification of the film. Additionally, the Cu target, which has a high arc-erosion coefficient of 33µg/J, results in a higher inclusion of cathode droplets with majority droplet sizes which are <5µm.

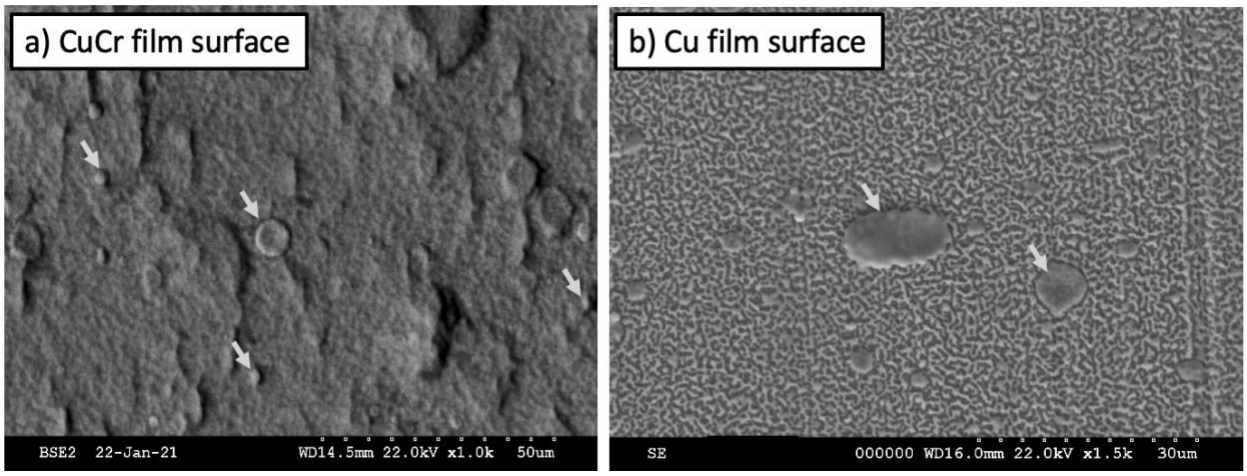

Figure 3.7 Surface morphology of a) CuCr films b) Cu films

To improve film densification, the bias voltage was increased to -80V (fig. 3.8(b)), resulting in a reduction in surface pores, indicating better densification. However, no improvement in overall porosity was observed. To improve the thickness, the deposition time was increased to

60 minutes, and the microstructure obtained is shown in Figure 3.8(c). While the surface porosity showed improvement, the cross-section image revealed some areas where film porosity spanned throughout the film's thickness. Also, from the image 3.8(d) it is evident that the growth direction is vertical or normal to the substrates surface. To address this issue, it is necessary to either increase the arc current or reduce the chamber pressure at the given bias voltage. It should be noted that increasing the arc current beyond 100A led to the unstable burning of the Cu cathode, and the currents deposits are produced at a chamber base pressure of $2x10^{-5}$ Torr, as limited by the vacuum pumping arrangement (for 10sccm Ar). It has been reported that the deposition rate, especially for Cu, reduces significantly when the bias voltage increases due to increase in re-sputtering effects [1]. Therefore, a low bias voltage of -20V was used for co-deposition films.

The microstructures of co-deposited CuCr coatings are presented in the figure 3.9-3.11, and the compositional analysis is provided in Table 3.2. The thickness of the coatings is between 11-14µm, and the deposition rate is approximately 100 nm/min. Among the samples, CuCrB exhibits the highest Cu content, followed by CuCrA and CuCrC. Both CuCrA and CuCrC samples display predominant Cr-rich regions closer to the top of the coatings. The cross-section SEM image of the CuCrA sample shown in figure 3.9 reveals a maximum composition of 33 wt% Cu and 76 wt% Cr near the substrate, while the top of the deposit shows a minimum composition of 4 wt% Cu and 96 wt% Cr. Similarly, CuCrC exhibits a maximum content of 26 wt% Cu and 74 wt% Cr in the bottom 3µm of the coating near the substrate, and the rest of the coating thickness consists of 1 wt% Cu and 99 wt% Cr. The EDX mapping of the CuCrC sample, as depicted in the figure 3.11, further confirms the concentration of Cu in the bottom section of the coating close to the substrate.

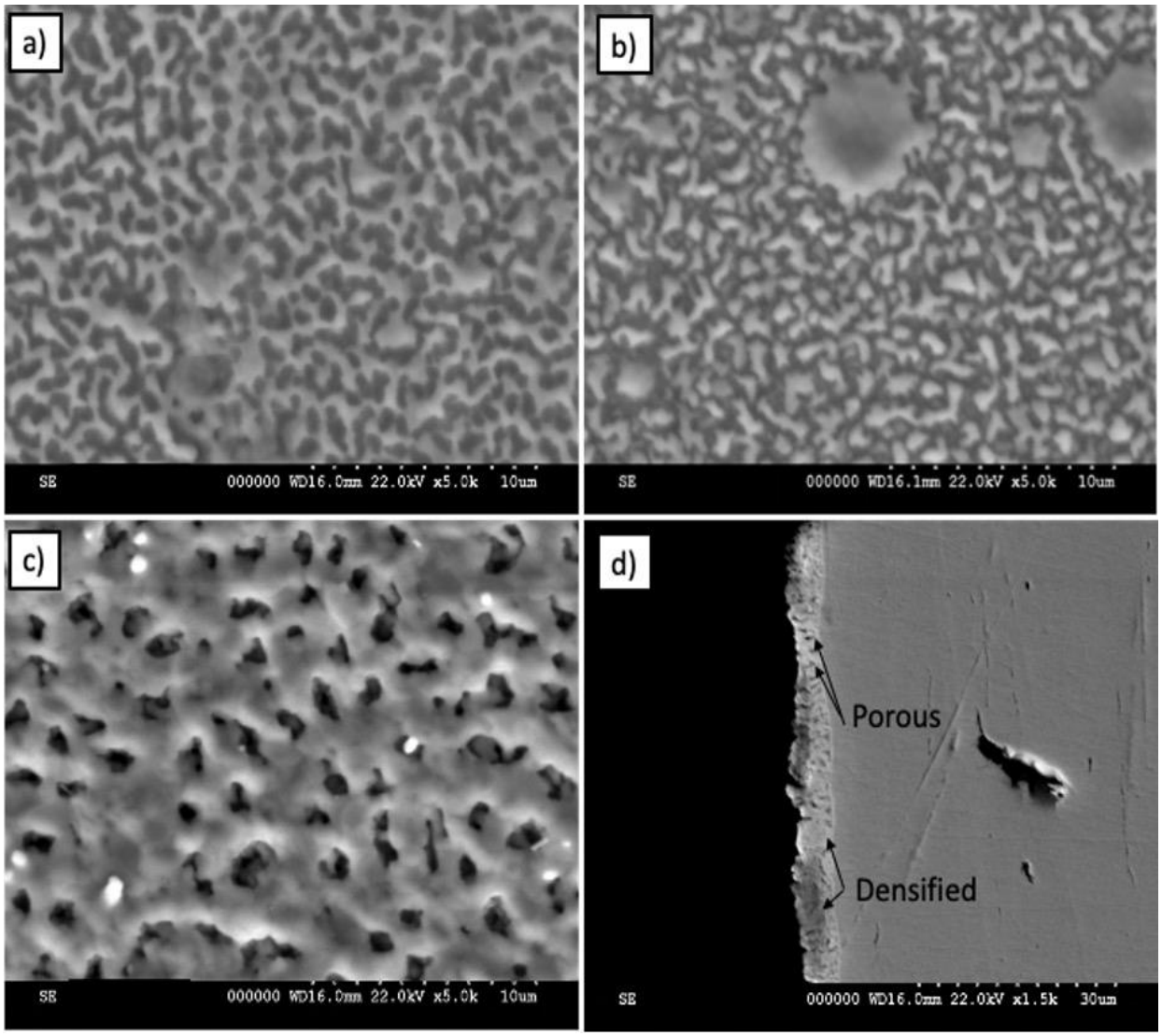

Figure 3.8 Surface morphology of Cu films deposited at a)-20V bias, 15 mins b) -80V bias, 15mins c) -20V bias, 60 mins d) Cross-section -20V, 60 mins

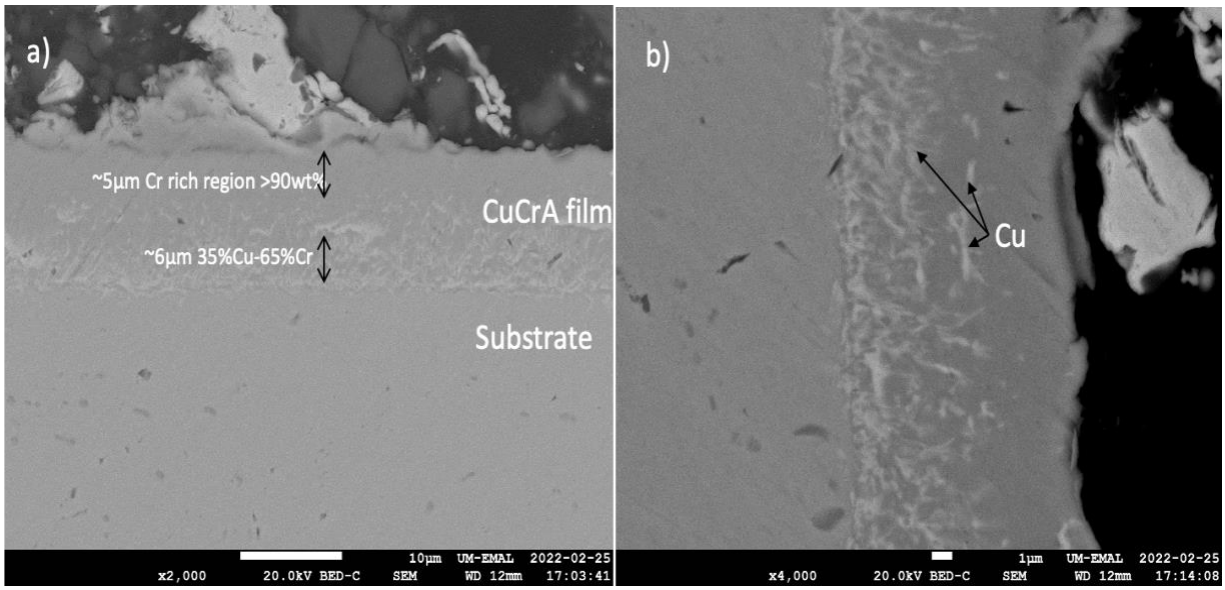

Figure 3.9 CuCrA film a)2kx image showing CuCr film closer to substrate and Cr rich layer at top surface of the film b)4kx image showing Cu islands within CuCr film

In comparison to CuCrC, CuCrA, deposited at a lower arc current for the Cu target (60A vs 90A), demonstrates a higher Cu content distributed over a thickness of approximately 6µm from the substrate. Both coatings exhibit Cr-rich top regions, suggesting significant Cu re-sputtering occurs as the process time increases. As the process time increases, the substrate temperature also rises to approximately 350-400ºC, providing sufficient energy for Cu atoms to be re-sputtered away from the deposited film. From the compositional analysis, increasing the Cr ion flux during deposition affects the Cu content retained with the film [33].

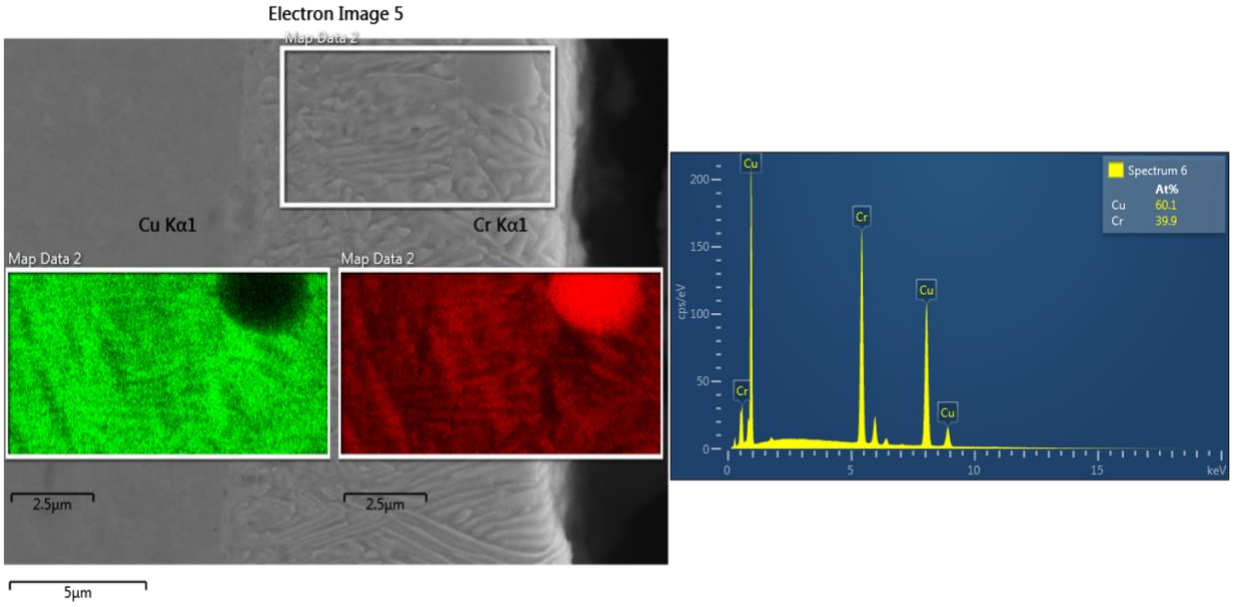

Figure 3.10 CuCrB film cross-section with EDX mapping inset and spectrograph on the right

CuCrB sample, as depicted in figure 3.10, exhibits a layered structure consisting of alternating Cr and Cu layers. The composition in this sample is more uniform and closer to a 1:1 Cu to Cr ratio when compared to the CuCrA and CuCrC samples. The length of the layers are smaller near the substrate and gradually increases moving away from the substrate. This observation suggests that temperature effects may be contributing to this phenomenon as the deposition time increases. The layered needle-like structures observed in the sample do not exhibit a preferential growth direction but appear to align normal to the substrate surface, indicating a vertical growth. Cu and Cr are mostly immiscible phases, with FCC Cu phase containing approximately 1.2% at Cr in solid solution. Therefore, growth predominantly occurs as two-phase islands, where the mobility of like phases increases at higher substrate temperatures over longer deposition times. It is noteworthy that CuCr coatings produced using other PVD techniques have reported layered structures at much smaller nano-scales than the sub-micron scales in the current samples [17,18].

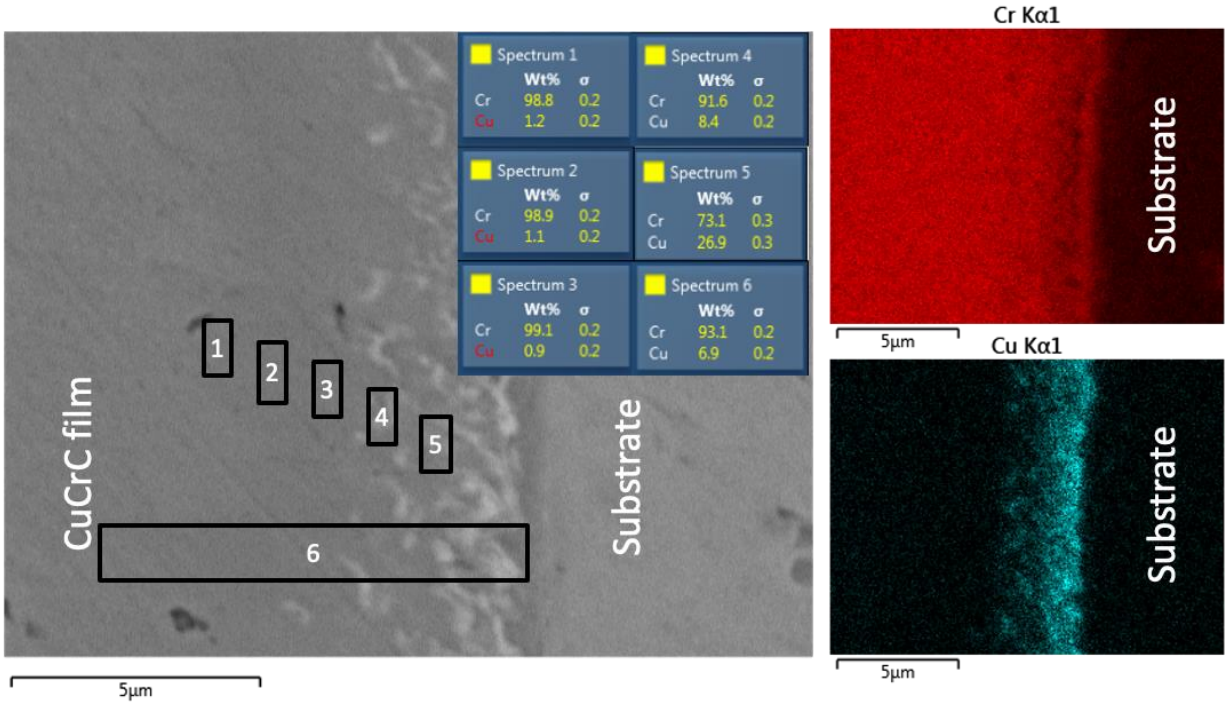

Figure 3.11 CuCrC film with EDX mapping on right

Sample	Coating Thickness (µm)	Film Cross-Section composition by EDX				Film composition by XRD	
		Cu %		Cr %		Cu %	Cr %
		Min	Max	Min	Max		
CuCr A	11 / ±1	4	33	67	96	4	96
CuCr B	14/± 2	42	61	39	58	48	52
CuCrC	12 /±1	1	26	74	99	3	97

Table 3.2 Analysis of CuCr films

3.3.2 Xray Diffraction Analysis of CuCr films

XRD patterns obtained for the CuCr films are shown in the figure 3.12, with reference peaks corresponding to FCC Cu (111), (200), and (220) at 2θ values of 43.4°, 50.5°, and 74.2°,

and to BCC Cr (110), (200), and (211) at 2θ values of 44.4°, 64.6°, and 81.6°, respectively. To investigate the effects of different deposition parameters on diffraction intensity, the XRD patterns are fitted using the mixture of Gaussian and Lorentzian profiles using Jade-8 software. In the CuCrA and CuCrC samples, the Cu intensities are lower compared to CuCrB due to the presence of a Cr-rich top film surface. Both CuCrA and CuCrC samples exhibit similar FWHM values, which are lower than those of the CuCrB samples. The CuCrB sample, on the other hand, displays some broadening of the Cr peaks, approximately 0.05° in (110) and (200), and greater than 0.1° in (211) orientations, respectively. This broadening can be attributed to smaller crystallite sizes resulting from growth suppression due to the layered Cu/Cr structure. Also, for CuCrB sample, the Cu (200) and Cr (200) are the preferential plane orientations.

Typically, for Cr coatings (or other closed packed crystal structures) should present a preferential orientation corresponding to the (110) crystallographic planes which have the highest reticular density [7,8]. However, parameters which control the adatom energy, such as deposition rate, substrate temperature and bias voltage, and presence of impurities can alter preferential crystallographic orientation. The texture observed in Cr films at low substrate temperatures and ion energies, generally orient to crystallographic planes with lower reticular densities, i.e (211)>(200)>(110) [7]. Consequently, an increase in temperature facilitates the orientation in crystallographic planes with the highest reticular density. Therefore, low bias voltage used for current films results in deposition at low substrate temperatures, and at relatively high deposition rates preferential orientation other than Cr(110) and Cu (111) can be expected.

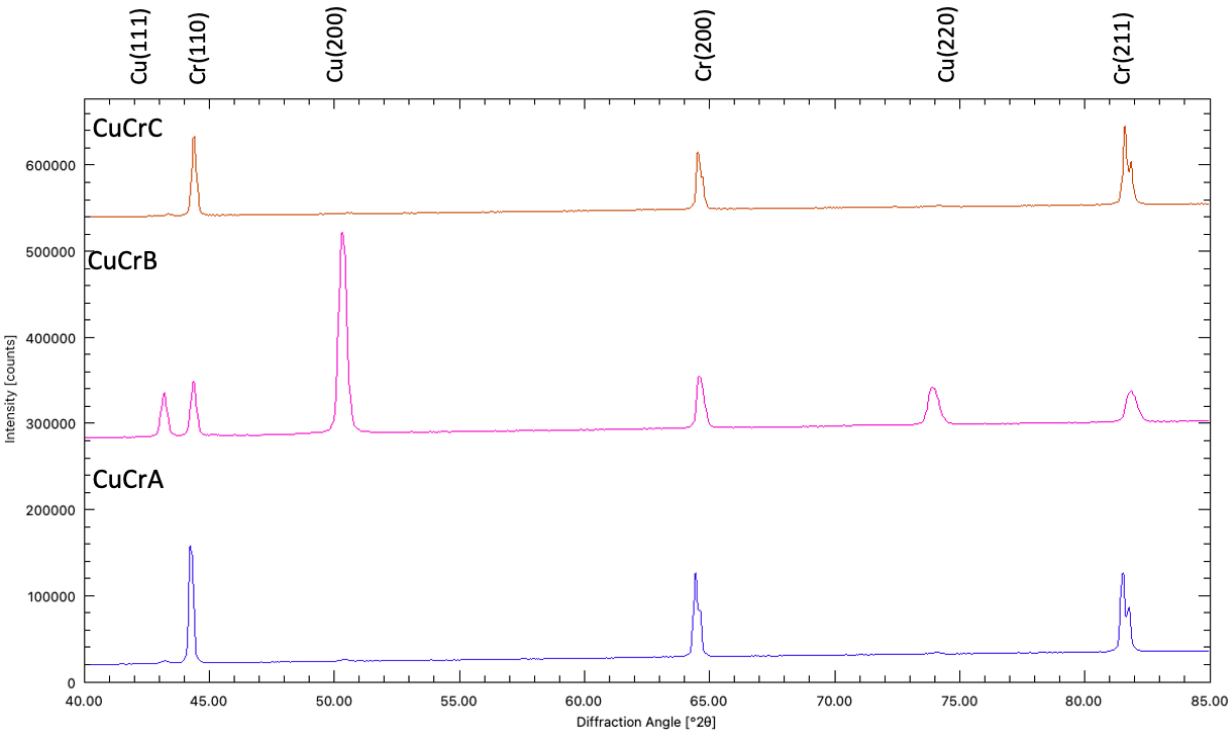

Figure 3.12 XRD of CuCr films

Figure 3.13 shows the $Sin^2\psi$ plot used for residual stress calculation. Samples CuCrA, CuCrB and CuCrC have residual stresses of 960, 1620 and 1020 MPa respectively. It is noteworthy that all samples have tensile residual stresses (as indicated by the positive slope of the plot). Samples CuCrA and CuCrC have comparable residual stresses and CuCrB has 1.5 times higher stress. Cr (211) peak was used to compare the residual stress as samples CuCrA and CuCrC have very low intensity of Cu peaks at high diffraction angles.

Residual stresses in thin films are resultant from contribution of intrinsic and thermal stresses. Thermal stresses can be neglected as the films are deposited at low substrate temperature $< T_m$, melting point of the film. The film growth mechanisms such as grain growth, defect annihilation, phase transition tend to generate tensile stresses [13]. It has been reported that ion bombardment low energies lead to film containing voids due to the low adatoms mobility. This shrinks the film due to the high surface tension of the inner surface of the voids, which decreases

the film volume and generates the tensile stress in the film [5,14]. Severe tensile stresses are associated to cause cracks in the film and de-laminating it at the substrate.

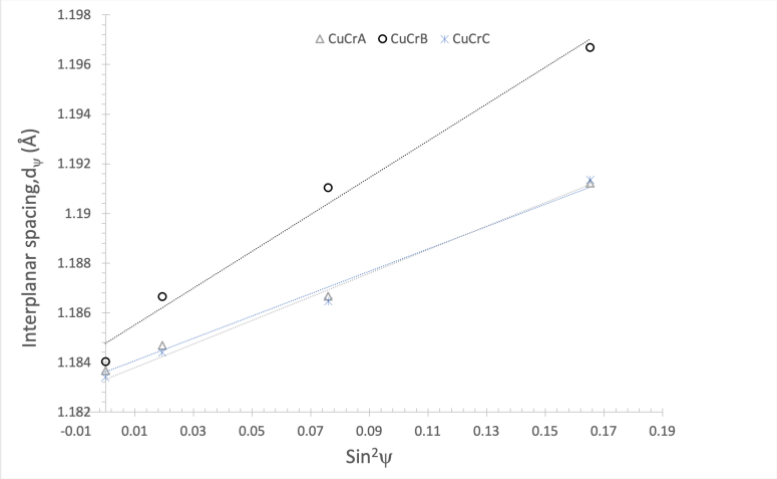

Figure 3.13 Residual stress plot for CuCr films

On the other hand, compressive stresses are developed in a film due to 'atomic peening' effect when high ion energies are employed for deposition. Deposition with high energy ions can cause atoms to be incorporated into vacant spaces which are smaller than the usual atomic volume, causing outward film expansion. However, as the film grows, it becomes constrained and unable to freely expand, resulting in compressive stresses. Additionally, very high ion bombardment during deposition induces surface diffusion, local heating and collapse of voids leading to dense packing and contributes to the decrease of tensile stress. Generally, compressive stresses are proportional to the substrate bias, as higher bias results in increased ion energies [13]. For current films with low substrate bias, the tensile residual stress can be attributed to the low ion energy film growth process.

3.3.3 Hardness Measurements for CuCr films

The hardness (H) and elastic modulus (E) values obtained through nanoindentation measurements are presented in Figure 3.14. For CuCrA, CuCrB, and CuCrC, the hardness values are 3.9 (±0.2), 5.2 (±0.8), and 4.2 (±0.6) GPa, respectively, while the corresponding modulus

values are 192 (±4), 174 (±16), and 190 (±8) GPa. CuCrB exhibits the highest hardness among the three samples, which can be attributed to its layered structure. In layered heterogeneous films, the deformation is limited by the softer phase. In this case, Cu phase undergoes plastic deformation first, and then the interaction with harder neighboring Cr layer resists further deformation, thereby improving the hardness [16,18,31].

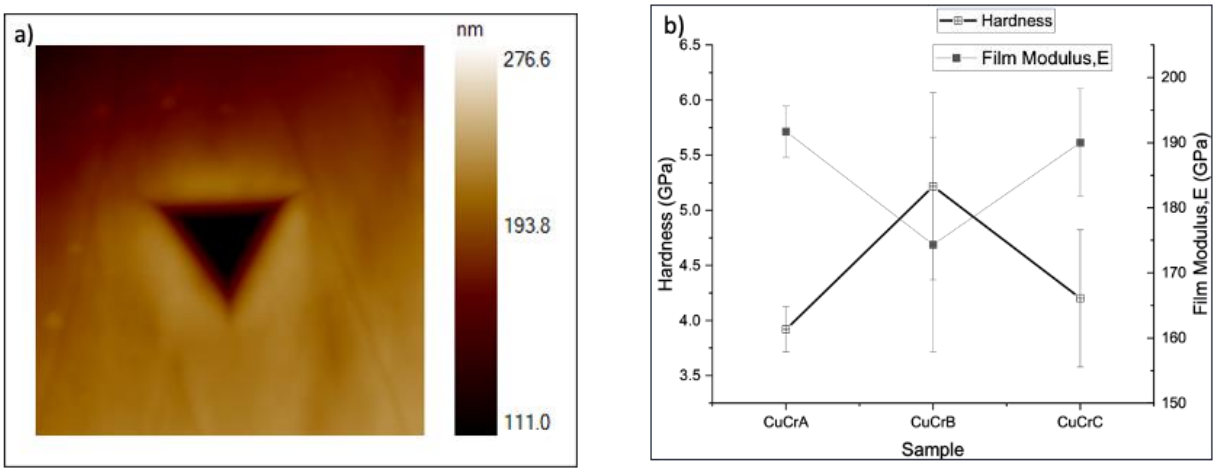

Figure 3.14 a) Typical indent with Berkovich probe b) Hardness and bulk modulus of CuCr films

Additionally, in polycrystalline films, the strength is influenced by grain sizes and film density [5,10]. The effect of grain size d_g on yield stress σ_y (and in turn hardness) as correlated to dislocation pile-up at grain boundaries, consequently affecting films hardness, is given by: $\sigma_y = \sigma_o + k_{HP}\, {}^{1}\!/\!_{\sqrt{d_g}}$; where σ_y & k_{HP} are constants. In general, for very small grain sizes (<10 nm), an inverse Hall-Petch effect is observed, where hardness decreases with decreasing grain size. However, for the CuCrB sample, the ion energies during deposition are high to produce smaller grain sizes which exhibit the inverse Hall-Petch effect. For sample CuCrB, which exhibits XRD peak broadening should have lower crystallite sizes when compared to the other samples, resulting in higher hardness.

3.4 Discussion on CuCr Co-deposited Films

The microstructural analysis of the co-deposited films reveals that their compositions vary depending on the arc currents applied to the Cu and Cr cathodes. Increasing the Cr:Cu arc current ratio results in a decrease of overall Cu content in the films. As the deposition process continues for a longer duration, higher substrate temperatures are reached, leading to an increase in the rate of Cu sputtering from the coatings [33], especially form the top film surface as observed in samples CuCrA and CuCrC. To investigate the loss of Cu content with increasing Cr cathode currents, the self-sputtering yield for CuCr films is estimated using the Monte Carlo simulation TRIM code. Surface atoms are not as strongly bound as sub-surface atoms, making it easier for bombarding ions to remove surface atoms from their lattice sites. The TRIM calculations consider surface binding energy and displacement energy to determine the outcome of an ion cascade. When the energy exchange of the bombarding ion is greater than the displacement energy, surface atoms are sputtered away [29]. For CuCr films, the TRIM calculations are performed using Cr ions and Cu ions with 100eV kinetic energy at varying ion collision angles between 0-90º (with respect to the substrate's normal axis) as the substrate rotates during deposition. The Cu/Cr self-sputter yield ratio is plotted (against ion collision angle) to illustrate how many additional Cu atoms from the film surface are sputtered away compared to Cr atoms per single colliding ion. The results indicate that when either Cu or Cr ions bombard the CuCr film between 0-45º ion collision angle, at least 2x more Cu atoms are sputtered away (compared to Cr) from the growing film per colliding ion. This confirms that when the ion density of Cr is higher than that of Cu, more Cu will sputter away, leading to lower Cu content in the coatings. However, as Cu ion densities increase and the rate of Cu deposition increases when compared to rate of sputter resulting in an improved Cu content in

the films, as seen in CuCrB samples. This demonstrates that for co-deposition, having a low Cr/Cu cathode current ratio seems ideal for depositing a 1:1 CuCr film with an improved Cu content.

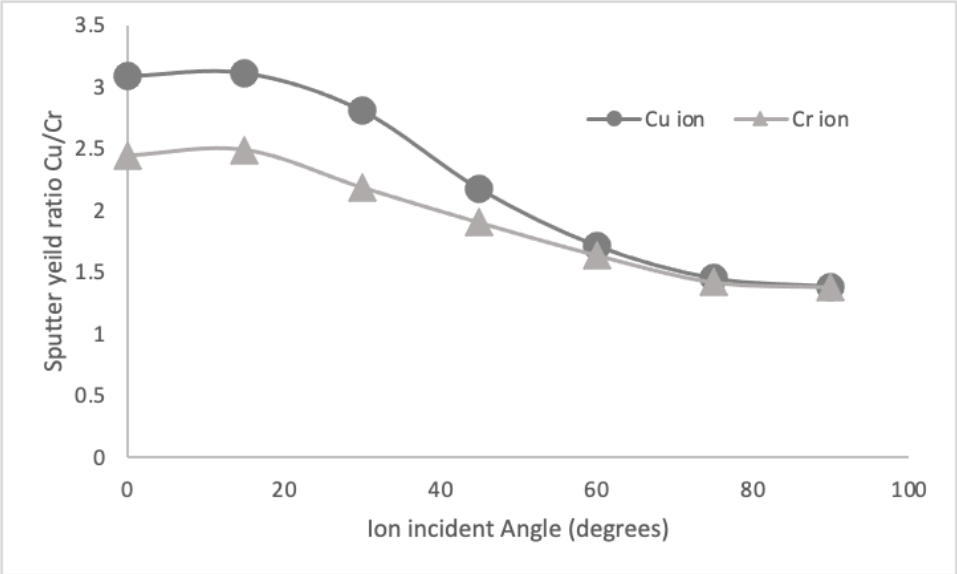

Figure 3.15 Calculated sputter yield ratio of Cu/Cr atoms sputtered per incident ion

In the CuCrB sample with a higher Cu content, a layered structure is observed, similar to previous studies using sputtering methods. However, in this study, the layered structure in CuCrB appears larger in size, on the micron scale, compared to the nanosized layers reported in the literature. The difference in scale can be attributed to energetic condensation of ions leads to higher mobility and larger immiscible Cu/Cr layers. Unlike CuCr films deposited by sputtering PVD techniques, the VAPD process shows no evidence of the formation of metastable phases. Both Cu and Cr are observed to be in pure polycrystalline phases. The absence of metastable phases can be beneficial for achieving higher electrical conductivity in the final CuCr coatings which is critical for VI applications. The VAPD technique also demonstrates a higher deposition rate of approximately 100 nm/min compared to rates of around 10s nm/min for MBE and sputtering techniques. The measured residual stresses in the films agree with those reported for DC sputtering techniques for CuCr films. The hardness of DC magnetron sputtered coatings typically falls within

the range of 2-12 GPa, as reported in previous studies [17, 18]. Similarly, the hardness of VAPD CuCr coatings is measured to be within similar range (4-5GPa). However, when comparing VAPD CuCr coatings with similar microstructural composition to those produced by DC magnetron sputtering, the hardness is slightly lower in the VAPD coatings. This difference in hardness can be attributed to factors such as smaller grain sizes and the presence of nano-layered structures, which are more prevalent in sputtered coatings. However, the hardness of the VAPD films are much higher than cold-sprayed and other traditional PM methods which can be beneficial for arc-erosion resistance as discussed in chapter 1.

3.5 Conclusions

The primary objective of the study was to investigate the influence of arc current ratios of Cr/Cu in producing CuCr thin films using in-house built VAPD system using co-deposition technique. After analyzing the microstructural composition and hardness properties of the films, the following conclusions were drawn:

- CuCr films deposited at high Cr/Cu arc currents showed significant Cu-sputtering from the deposited films. When the Cr/Cu arc current ratio was >1, there was a noticeable removal of Cu atoms from the film due to sputtering. On the other hand, when the Cr/Cu ratio was <1, the film had close to a 1:1 Cu:Cr wt% composition. The samples CuCrA and CuCrC, which were deposited with higher current ratios, showed a Cr-rich top surface. The higher sputter-yield of Cu is consistent with TIMS calculations.
- All samples had a thickness greater than 10μm, and the deposition rate was approximately 100nm/min. CuCrB, in particular, exhibited broadened XRD peaks and preferred growth orientation for Cu(200) and Cr(200).

- The VAPD-deposited films displayed tensile residual stress as low bias voltage was employed for deposited for the films. CuCrB had the highest residual stress value and hardness compared to the other two samples.

References

[1] J.R. Shi, S.Lau, Z. Sun, X. Shi, B.K. Tay, H.S. Tan, Surf. Coating Technol., 138 (2001), p. 250

[2] S.P Lau, Y.H Cheng, J.R Shi, P Cao, B.K Tay, X Shi, Filtered cathodic vacuum arc deposition of thin film copper, Thin Solid Films, Volumes 398–399, 2001,P 539-543

[3] Crystal Structures 1 (1963) 7-83 Second edition. Interscience Publishers, New York

[4] Mechanical properties of thin films

[5] Volkhonsky, A.O.; Blinkov, I.V.; Belov, D.S. The Effect of the Metal Phase on the Compressive and Tensile Stresses Reduction in the Superhard Nitride Coatings. Coatings 2020, 10, 798. https://doi.org/10.3390/coatings10080798

[6] John A. Thornton, D.W. Hoffman, Stress-related effects in thin films, Thin Solid Films, Volume 171, Issue 1, 1989, Pages 5-31, ISSN 0040-6090, https://doi.org/10.1016/0040-6090(89)90030-8.

[7] C Gautier, J Machet, Effects of deposition parameters on the texture of chromium films deposited by vacuum arc evaporation, Thin Solid Films, Volume 289, Issues 1–2, 1996, Pages 34-38, ISSN 0040-6090,

https://doi.org/10.1016/S0040-6090(96)08891-8

[8] E. Grantscharova, Texture transition in thin metal films vacuum condensed on glass: a general consideration, Thin Solid Films, Volume 224, Issue 1, 1993, Pages 28-32, ISSN 0040-6090, https://doi.org/10.1016/0040-6090(93)90453-V

[9] J.R Shi, S.P Lau, Z Sun, X Shi, B.K Tay, H.S Tan, Structural and electrical properties of copper thin films prepared by filtered cathodic vacuum arc technique, Surface and Coatings Technology, Volume 138, Issues 2–3, 2001, Pages 250-255, ISSN 0257-8972, https://doi.org/10.1016/S0257-8972(00)01159-2

[10] C Mitterer, P.H Mayrhofer, J Musil, Thermal stability of PVD hard coatings, Vacuum, Volume 71, Issues 1–2, 2003, Pages 279-284, ISSN 0042-207X, https://doi.org/10.1016/S0042-207X(02)00751-0.

Recrystallization

[11] Cullity BD, Stock SR. Elements of X-ray Diffraction, Third Edition. New York: Prentice-Hall, 2001.

[12] F.M. D'Heurle, J.M.E. Harper, Note on the origin of intrinsic stresses in films deposited via evaporation and sputtering, Thin Solid Films, Volume 171, Issue 1, 1989, Pages 81-92,ISSN 0040-6090, https://doi.org/10.1016/0040-6090(89)90035-7.

[13] Grégory Abadias, Eric Chason, Jozef Keckes, Marco Sebastiani, Gregory B. Thompson, Etienne Barthel, Gary L. Doll, Conal E. Murray, Chris H. Stoessel, Ludvik Martinu; Review

Article: Stress in thin films and coatings: Current status, challenges, and prospects. Journal of Vacuum Science & Technology A 1 March 2018; 36 (2): 020801. https://doi.org/10.1116/1.5011790

[14] A Misra, S Fayeulle, H Kung, T.E Mitchell, M Nastasi, Residual stresses and ion implantation effects in Cr thin films, Nuclear Instruments and Methods in Physics Research Section B: Beam Interactions with Materials and Atoms, Volume 148, Issues 1–4, 1999, Pages 211-215, ISSN 0168-583X, https://doi.org/10.1016/S0168-583X(98)00780-0.

[15] X. G. Li et al., "Tuning the Microstructure and Mechanical Properties of Magnetron Sputtered Cu-Cr Thin Films: The Optimal Cr Addition," Acta Materialia 151 (June 1, 2018): 87–99, https://doi.org/10.1016/j.actamat.2018.03.044.

[16] M. A Baker et al., "The Nanostructure and Mechanical Properties of PVD CrCu (N) Coatings," Surface and Coatings Technology 162, no. 2 (January 20, 2003): 222–27, https://doi.org/10.1016/S0257-8972(02)00571-6.

[17] T. P. Harzer et al., "Nanostructure and Mechanical Behavior of Metastable Cu–Cr Thin Films Grown by Molecular Beam Epitaxy," Acta Materialia 83 (January 15, 2015): 318–32, https://doi.org/10.1016/j.actamat.2014.10.013.

[18] Xiaoqin Wang et al., "Layered Structure Enhances the Hardness of Cu-48at.%Cr Film Prepared by Co-Sputtering Deposition Technique - ScienceDirect," accessed June 27, 2023, https://www.sciencedirect.com/science/article/pii/S0042207X2100292X.

[19] Andersen, H.H. and Bay, H.L., 1981. Sputtering by ion bombardment. ed. R. Berisch, Springer–verlag, Berlin Heidelberg New York, 145.

[20] Andre Andes, "Cathodic arc plasma deposition", Vacuum Technology & Coatings, Volume 3, 2002.

[21] R. L. Boxman and S. Goldsmith, "Principles and applications of vacuum arc coatings," IEEE Transactions on Plasma Science, vol. 17, 1989, pages 705-712.

[22] R.L. Boxman, S. Goldsmith, "Macroparticle contamination in cathodic arc coatings: generation, transport and control, Surface and Coatings Technology", Volume 52, 1992, Pages 39-50

[23] X. Maeder, A. Neels, M. Döbeli, A. Dommann, H. Rudigier, B. Widrig, J. Ramm, "Comparison of in-situ oxide formation and post-deposition high temperature oxidation of Ni-aluminides synthesized by cathodic arc evaporation", Surface and Coatings Technology, Volume 309, 2017, Pages 516-522.

[24] Chi-Lung Chang, Jun-Han Chen, Pi-Chuen Tsai, Wei-Yu Ho, Da-Yung Wang, "Synthesis and characterization of nano-composite Ti–Si–N hard coating by filtered cathodic arc deposition", Surface and Coatings Technology, Volume 203, Issues 5–7, 2008, Pages 619- 623.

[25] J.Q. Zhu, M.P. Johansson-Jöesaar, P. Polcik, J. Jensen, G. Greczynski, L. Hultman, M. Odén, “Influence of Ti–Si cathode grain size on the cathodic arc process and resulting Ti– Si–N coatings”, Surface and Coatings Technology, Volume 235, 2013, Pages 637-647.

[26] Andes Andre, “A structure zone diagram including plasma-based deposition and ion etching”, Thin Solid Films, vol. 518, 2010, issue 15, pages 4087-4090.

[27] C. Sabitzer, J. Paulitsch, S. Kolozsvári, R. Rachbauer, P.H. Mayrhofer, “Impact of bias potential and layer arrangement on thermal stability of arc evaporated Al-Cr-N coatings”, Thin Solid Films, Volume 610, 2016, Pages 26-34.

[28] V.D. Ovcharenko, A.S. Kuprin, G.N. Tolmachova, I.V. Kolodiy, A. Gilewicz, O. Lupicka, J. Rochowicz, B. Warcholinski, “Deposition of chromium nitride coatings using vacuum arc plasma in increased negative substrate bias voltage”, Vacuum, Volume 117, 2015, Pages 27-34.

[29] F.T.N. Vüllers, R. Spolenak, “From solid solutions to fully phase separated interpenetrating networks in sputter deposited “immiscible” W–Cu thin films”, Acta Materialia, Volume 99, 2015, Pages 213-227.

[30] Farid Movassagh-Alanagh, Meisam Mahdavi, “Improving wear and corrosion resistance of AISI 304 stainless steel by a multilayered nanocomposite Ti/TiN/TiSiN coating”, Surfaces and Interfaces, Volume 18, 2020, 100428.

[31] B.D. Beake, V.M. Vishnyakov, A.J. Harris, “Relationship between mechanical properties of thin nitride-based films and their behavior in nano-scratch tests”, Tribology International, Volume 44, Issue 4, 2011, Pages 468-475.

[32] Andersen, H.H. and Bay, H.L., 1981. Sputtering by ion bombardment. ed. R. Berisch, Springer–verlag, Berlin Heidelberg New York, 145.

[33] J. F. Ziegler and J. Biersack, Monte Carlo code SRIM2006.02, downloadable from http://srim.org/,” 2006.

Chapter 4 Development of Composite Targets for VAPD

Abstract

This chapter focuses on the production of high Cr content CuCr composite targets using a pressure-less infiltration technique. Compared to other powder metallurgical techniques, the developed infiltration method yields high-density CuCr composites. In this study, two different Cr powders are employed to investigate the impact of Cr size dispersion on void content and electrical resistivity of the targets. The angular Cr powders exhibit high porosity, leading to areas of incomplete infiltration. On the other hand, spheroidal Cr powder produces dense composites with improved density. Furthermore, a CuCrW target is also produced for future investigations of VAPD coatings, as the addition of W is known to enhance the weld resistance of CuCr contacts. The final composition of the target material for VAPD is Cu35Cr65.

4.1 Introduction

Vacuum-arc plasma deposition (VAPD) technique requires arc ignition and sustained arc-spots on the target for the development of coatings. To ensure production of reliable coatings from composite targets, it is crucial to establish stable arcing conditions on the target surface. Unstable arcing can lead to undesired macroparticular ejection from the target's surface, which adversely affects the adhesion of coating interlayers on the substrate. From material standpoint, several factors need to be controlled, including phase distribution within the composite, surface defects, and impurities such as dielectric layers (e.g., oxides) on the target, to stabilize the arcing during deposition. Preparation of composite materials typically results in inadvertent internal porosity, which can entrap processing gasses from surrounding atmosphere. Targets containing pores or

entrapped gases result in unstable arcing conditions during deposition. High content of entrapped gases reduces the vacuum pressure and results in low charge state for ions within the deposition plasma. Higher chamber pressure also results in increased particle collisions with neutrals and reduces the ion energies [1]. Furthermore, the thermal properties of CuCr composites are essential for uniform target evaporation, which can be compromised if the composites have high porosity or inadequate interfacial bonding between the Cu matrix and Cr particles. Figure 4.1 shows targets with high porosity which undergo excessive surface melting and non-uniform wear during deposition.

Figure 4.1 Excessive arc-erosion on VAPD targets due insufficient thermal conduction as a result of high porosity

To achieve high Cr% composites (>50%) with minimal porosity through pressure-less infiltration, precise control over the distribution of Cr powder is essential to prevent premature sintering before the onset of Cu infiltration. Improper packing density of the Cr powders during processing can lead to the incomplete sintering of some unmelted Cr particles, resulting in the formation of internal voids that are inaccessible to molten copper during infiltration. Therefore, it is crucial to control the distribution of Cr powder within the composite to produce a dense composite, especially since porosity negatively affects thermal conductivity. This chapter aims to

explore the Cr powder effects on porosity of high refractory content CuCr composites, especially for use as a cathode for VAPD to produce CuCr films.

4.2 Materials and Methods

4.2.1 Materials

For this study two different Cr powders are used which have different powder shapes and SEM images of powders are shown in fig 4.2. The details of all stock powders used in this study are listed in table 4.1. Each of as-received Cr powders, were sieved to 3 cuts using a bench top sieving machine; Cut 1: having powder size ≤150-75µm, Cut 2: having size ≤75-45µm and Cut 3: having size ≤45µm in a benchtop sieve. The powders were dried in a convection oven at 70ºC for 8 hours and were individually mixed with stock Cu powder in a tumble mixer rotating at 60rpm for 2 hours. Three feedstock mixtures were obtained for the study and details for powder compositions are listed in table 4.2.

Powder	Stock Size	Purity	Supplier
Angular Cr (A-Cr)	≤200µm	99.8%	AEE, PA, USA
Spheroidal Cr (Sp-Cr)	≤150µm	99.9%	Chemalloy, PA, USA
Copper (Cu)	≤45µm	99.9%	AEE, PA, USA
Tungsten (W)	1-5µm	99.9%	AEE, PA, USA

Table 4.1 Details of as-received powders

Powder	Feedstock CuCr1	Feedstock CuCr2	Feedstock CuCr3
Cr (75-150µm)	A-Cr 27.5%	Sp-Cr 27.5%	Sp-Cr 26%
Cr (45-75µm)	A-Cr 27.5%	Sp-Cr 27.5%	Sp-Cr 26%
Cu	5%	5%	5%
W	0	0	3%

Table 4.2 Powder feedstock details

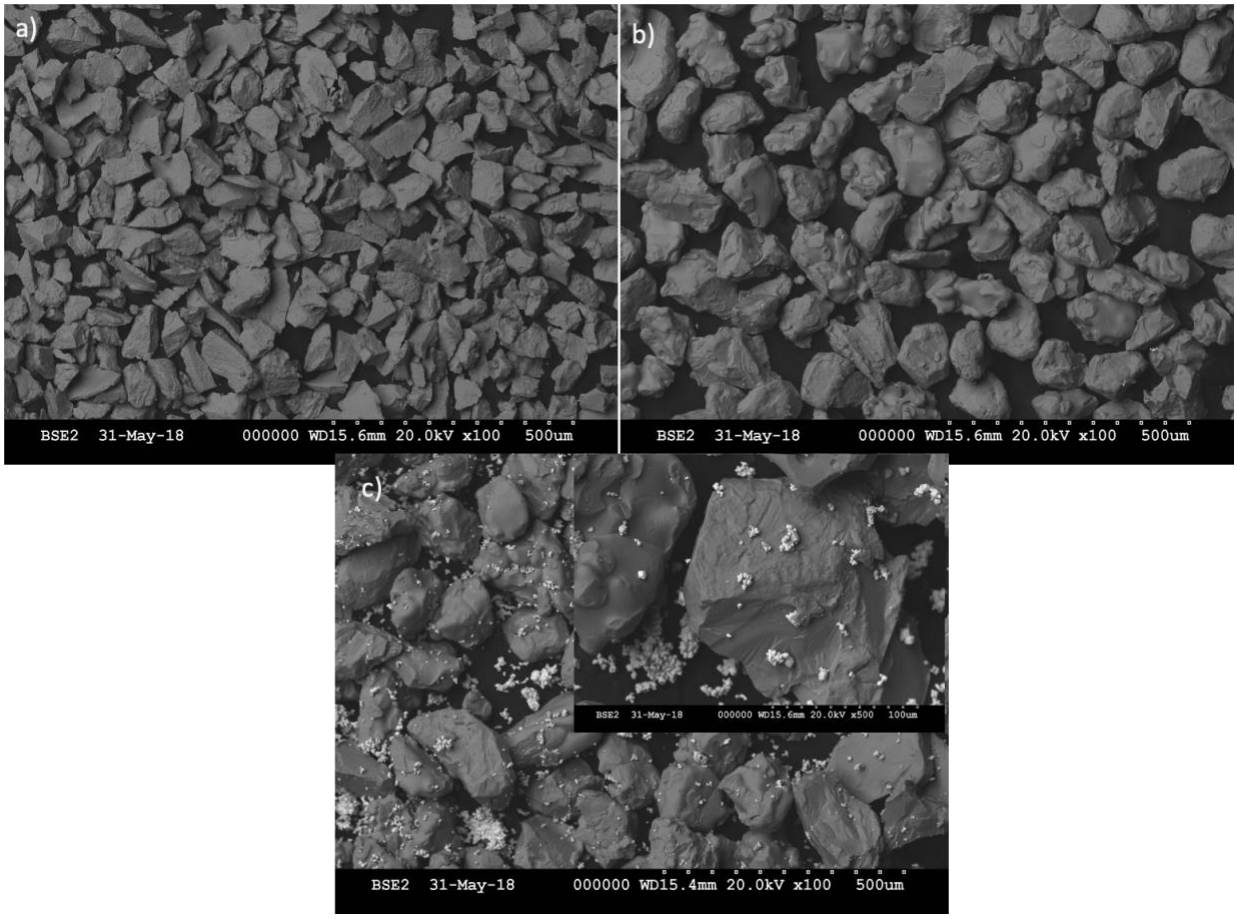

Figure 4.2 a) Angular Cr powder b) Spheroidal Cr powder c) Spheroidal Cr mixed with W powder (inset 500x)

4.2.2 Infiltration Experiments

Each of the feedstock powders from table 4.2 were placed in a graphite crucible having internal diameter of 65mm and height 65mm and packed using a vibratory table for 60 seconds. Additional copper block of approximately 60mm was placed on top of the packed powder feedstock (shown in fig (4.3)) and closed with a vented graphite cap. The crucibles were placed in a vacuum furnace and evacuated to $4x10^{-4}$ Torr. The heating was conducted in 3 stages according to the parameters shown in table 4.3, at a heating rate was 10ºC/min. After the completing the heating cycle, the samples were vacuum cooled and removed from the furnace when the temperature was below 100C.

Step	Temperature(ºC)	Time(min)
Furnace homogenizing	1050	60
Densification	1280	180
Precipitation	900	60

Table 4.3 3-Step heating sequence used for processing CuCr composites

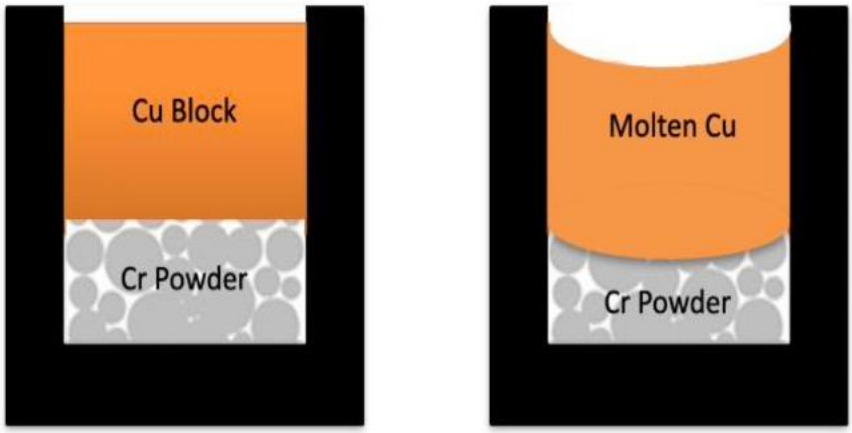

Figure 4.3 Assembly of packed feedstock powders and Cu piece inside graphite crucible for infiltration

4.2.3 Sample Preparation

Each of the infiltrated samples were cut to obtain 5mm thick discs from the bottom surface using a wet saw. Subsequently, using a milling machine, each 5mm disc was further cut into 2-ø20mm pieces, which were then prepared for analysis using standard metallurgical methods. The microstructures of the samples were observed using a Hitachi S-2600N SEM in backscattered electron (BSE) mode. The imaging was carried out with an accelerating voltage of 20kV, an emission current of 100μA, and a working distance of 15.4 mm. To investigate the Cu and Cr content of the samples, an energy dispersion spectrum detector (EDX) attached to the SEM was utilized. For each sample, the microstructural composition was reported as the average of 10 EDX

mappings, performed on a 4mm2 area at 50x magnification of the 2-ø20mm samples. This approach ensures accurate averaging for determining final composition of the CuCr composites.

4.3 Results & Discussion

SEM images of the samples CuCr1 to CuCr3 are shown in fig 4.4. CuCr1 samples produced with angular Cr powder displayed macro-porosity, indicating several un-infiltrated areas. The high packing density achieved for angular-shaped powders led to increased Cr sintering driven by powder necking at Cr-Cr contact points. This necking is thermodynamically preferred during homogenization (1050ºC) as it promotes surface energy reduction, resulting in the formation of Cr-Cr particulate bonds through chemical diffusion and leading to partial sintering at all Cr-Cr contact sites. Any partial sintering can cause blockages within the powder bed hindering the infiltration of molten Cu, causing porosity. One approach to reduce porosity in such cases is to increase Cu powder in the feedstock, which decreases the final Cr content in the composite. In contrast, spheroidal Cr powder produced dense composites with lower porosity, indicating improved infiltration of the matrix material (Cu) into the preform.

The total void volume present in the interconnected particulate network determines the amount of matrix material which needs to be infiltrated into the preform. Therefore, void fraction of perform determines composition of the composite. Figure 4.5 depicts relationship of void volume (as % porosity) with increasing % of larger particles in a packed bed containing multi-modal spherical powders. When the packed bed contains only small particles, the void volume in the preform is highest and indicted by V_S (typically around 60%). By substituting some of the smaller particles with larger particles, packing density of the powder bed increases; thereby, decreasing the void volume. A minimum void volume V* (typically around 35%) is achieved when the ratio of mean diameter of large particles to mean diameter of small particles is around 7.

Increasing the particle sizes further increases the void volume and reaches a value indicated by V_L. Typically, $V_S > V_L > V^*$ for most multi-modal powder beds. For a packed bed preform produced

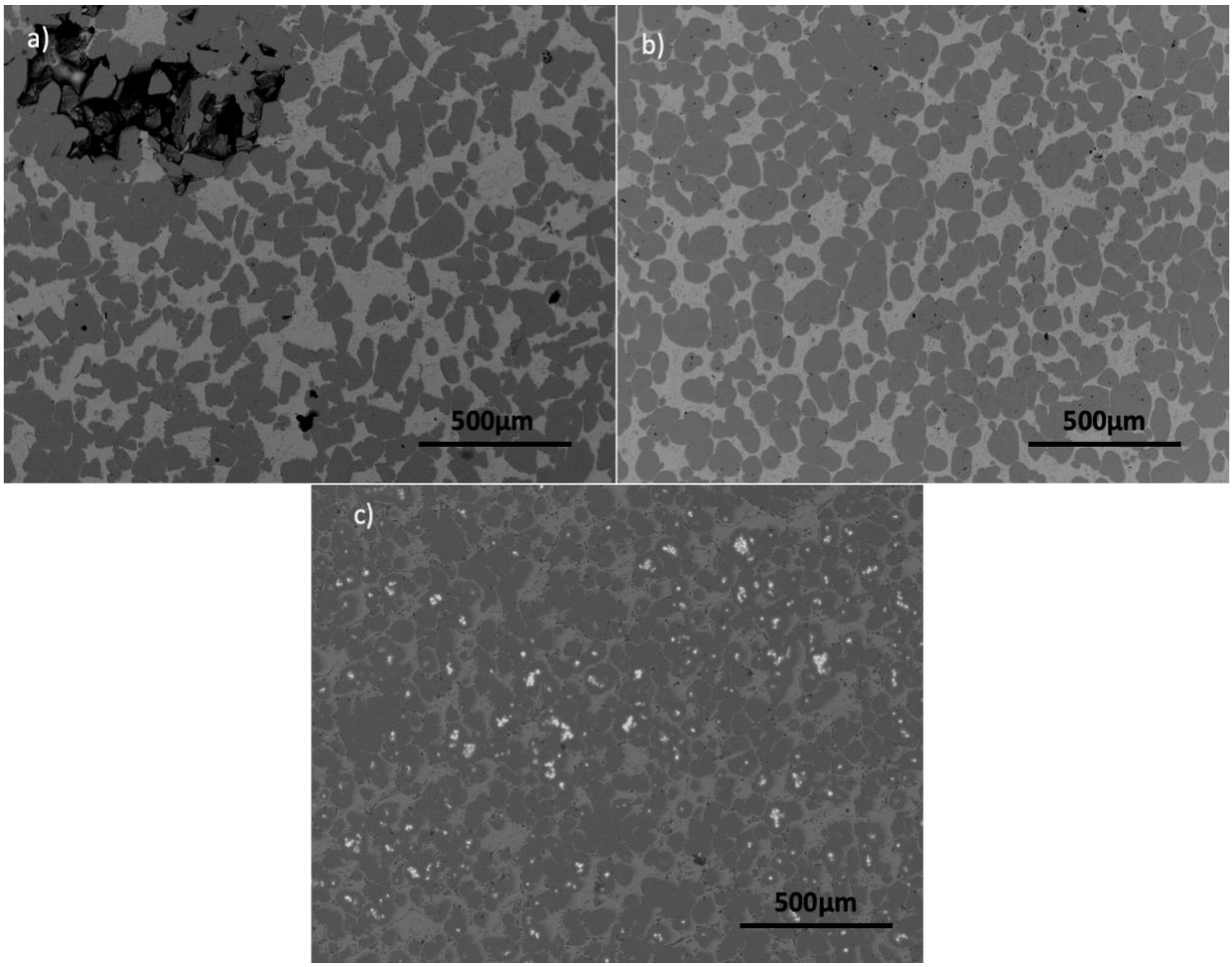

Figure 4.4 50x SEM images of a) CuCr1 b) CuCr2 c) CuCr3

by molding, the limiting value for the content of reinforcements in the final composite is given by V_S and V^*. If the composite requires higher particulate content than the preform can be produced by using compaction techniques. But for composites requiring low content of particulate phases, below V_S, forming a porous skeleton (containing>60% voids) for infiltration becomes cumbersome and inconsistent. Therefore, producing the composite by traditional infiltration techniques becomes redundant. Some techniques use a mixture of matrix materials along with

reinforcing materials to form a porous preform in order to reduce the composition of final particulate phase (<V_S) [4,6]. However, this technique produces non-uniform distributions of particulate phases in the final composite, as the breakdown of the interconnected particulate network occurs when the matrix material melts at infiltration temperatures; thereafter, the particulates are free to settle down or float depending on their density. For powder distributions used in present study yielded uniform Cr distribution without increased Cr-Cr sintering for Sp-Cr powders.

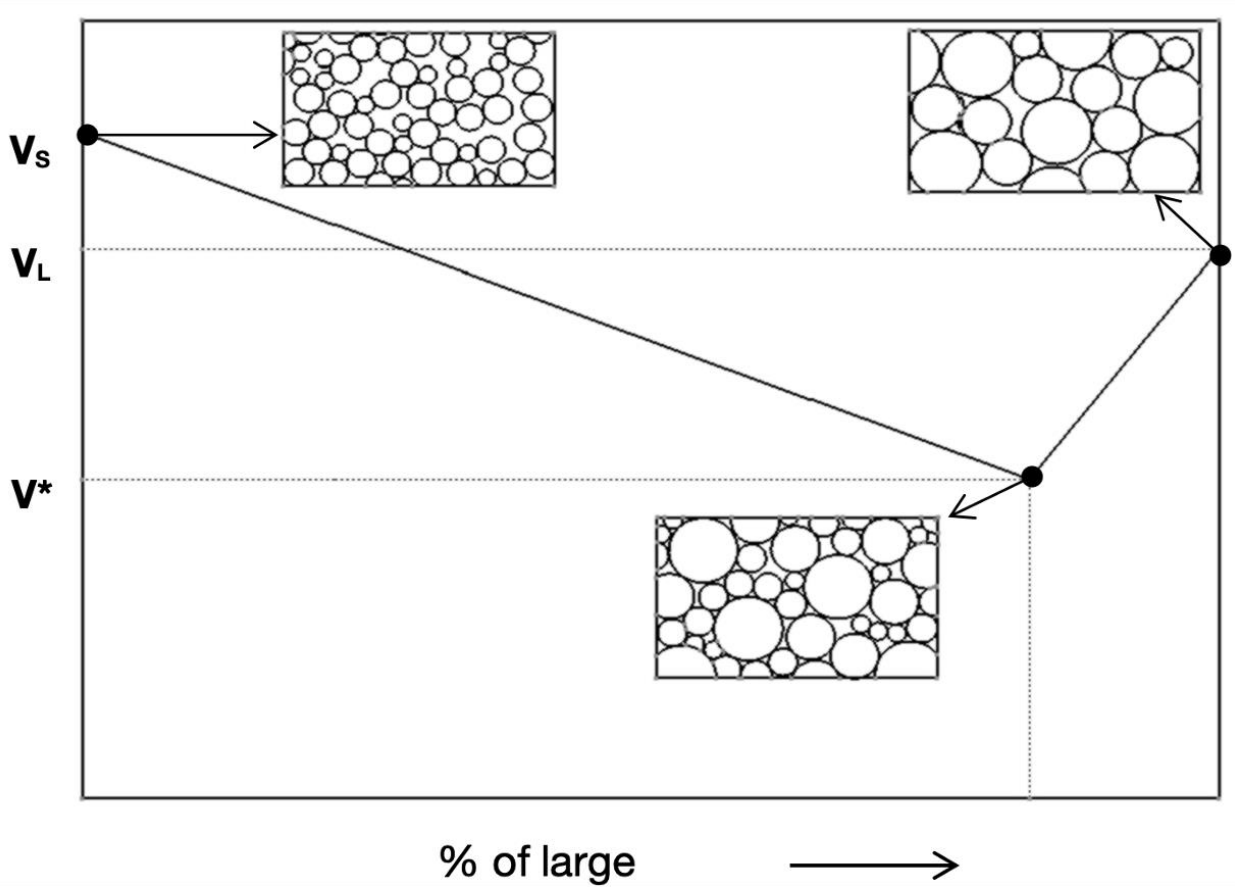

Figure 4.5 Pore volume in preform(feedstock) vs powder size ratio

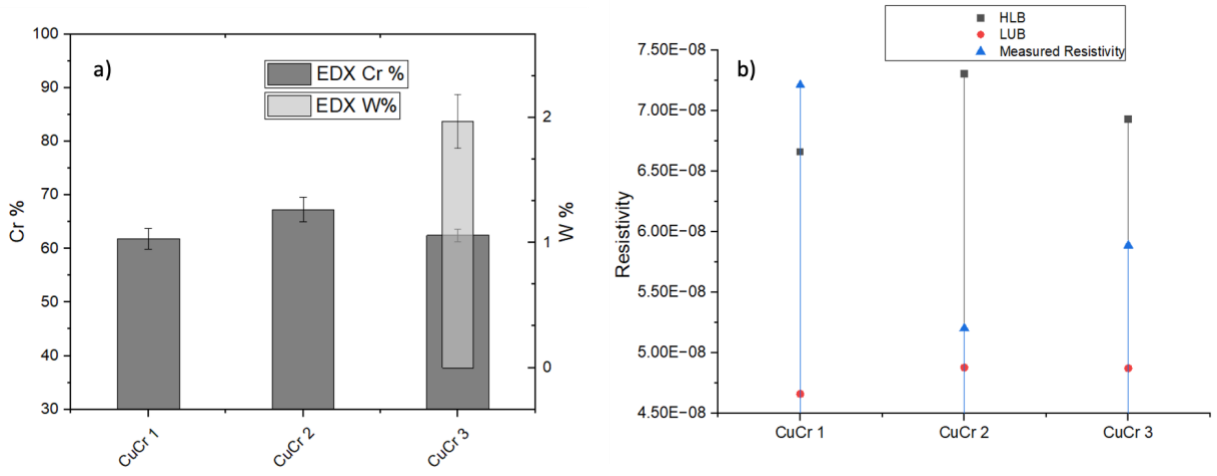

Figure 4.6 a) EDX analyses of composite compositions b) Electrical resistivity measurement using 4-point probe and predicted HLB & LUB values

Fig 4.6(a) shows the composition analysis for the targets obtained by EDX. All samples have around ~ 65% Cr and CuCr3 has 2% W. As discussed in chapter 1, Cu-Cr alloy system is characterized by a complete miscible liquid phase above melting point of Cr, a very small soluble Cr in Cu phase at temperature below melting point of Cu and a no solubility of copper in chromium. Hence, CuCr alloys are two-phase composites, usually consisting of chromium particles dispersed in a copper matrix. This system has a maximum solubility limit of 1.54wt% at 1077ºC [2,9], and it is indicative of solubility of Cr in Cu during processing of the composite. Infiltration is performed in 3 stages: In Stage 1 the powder bed of Cr and a solid Cu block is heated to a temperature above melting point of Cu and the molten Cu starts to wick into Cr powder bed filing in some of the pores formed by loosely packed powders; In Stage 2 molten Cu wets the Cr particulates and spreads further into the powder bed by dissolution of particulate edges, thereafter forming a Cu solution with up to 1.54% Cr dissolved in it; and Stage 3 after allowing sufficient processing time the infiltrated powder bed is cooled to a temperature below melting of Cu (900ºC), dendritic nucleates of Cu are formed adhering on Cr particulates and on further cooling down all of the dissolved Cr is precipitated (shown in fig 4.7 (a)). The interfacial energy balance at the

point of nucleation can be expressed in eq 4.1, where, σ_{PS} is particle/solid interfacial energy, σ_{PL} particle/liquid interfacial energy, σ_{SL} is particle/solid interfacial energy. Eq. 4.1 indicates that nucleation is favored in systems containing wetted particles, with the lowest interfacial energy corresponding to the lowest contact angle (θ). Consequently, preferential nucleation sites have lower effective interfacial energy, reducing the free energy barrier and facilitating nucleation. In the case of CuCr composites, the dissolution of Cr (~1.54wt%) during densification temperatures increases particulate wetting and decreases the interfacial energy at the Cr particulate interface, causing any Cr present to act as a preferential site upon which the first atoms of Cu initiate solidification during cooling causing improved interfacial bonding [6]. Decreased porosity, precipitation of any dissolved Cr and improved Cu/Cr interfacial bonding tends to form high conductivity composites.

$$\sigma_{PS} = \sigma_{PL} - \sigma_{SL} Cos\ \theta \tag{4.1}$$

In the CuCr3 sample, W is soluble in the particulate Cr phase but insoluble in the matrix Cu phases. To preserve high conductivity, when incorporating additional materials in CuCr composites, it is crucial that they exhibit no solubility with Cu or form any intermetallic compounds. W is completely immiscible in Cu and has marginally higher conductivity than Cr so its addition will not adversely affect the conductivities of the composites. During the initial processing, the feedstock is held at a homogenizing temperature of 1050ºC before being raised to the densification temperatures required to produce the composite. In the Cr-W system, Cr forms a solid phase intermetallic compound with W, denoted as Cr_mW_n, at temperatures below the melting point of Cu. Up to 5% by weight of W can be added to the particulate phase. During densification, all of the W is dissolved in the Cr, and it precipitates within the Cr particulate phase during cooling, as depicted in Figure 4.7(b).

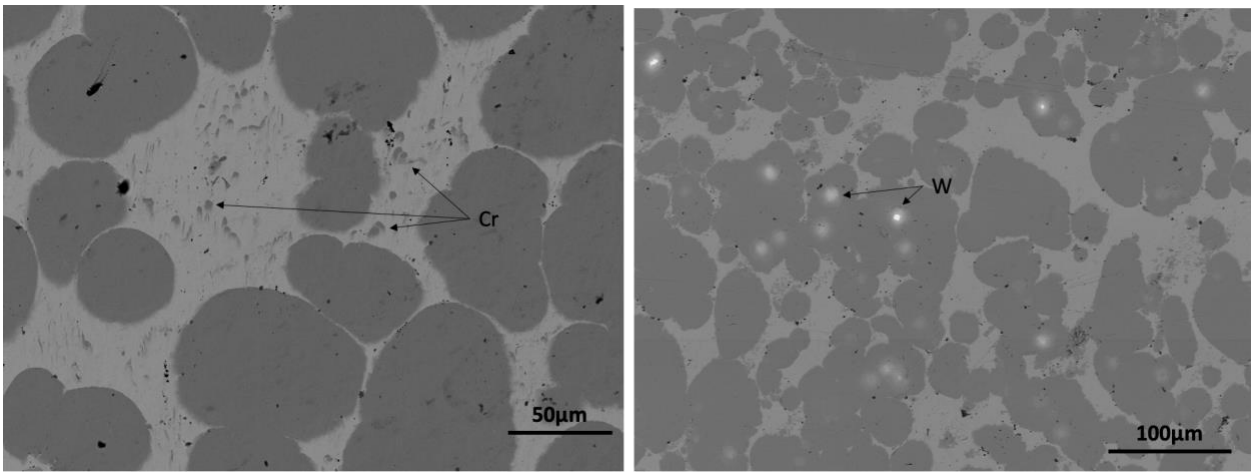

Figure 4.7 SEM images of a) CuCr2 with precipitated Cr b) CuCr3 with precipitated W

The targets used for the current VAPD are typically produced in 65x65mm cylinders, and to assess porosity, measuring the change in resistivity across various positions on the composite is considered valuable instead of performing cross-section SEM. Thus, the resistivity of the present composites is measured using the 4-point probe technique and compared with the predicted lowest-upper-bound (LUB) and highest-lower-bound (HLB) values given by equations 4.2 and 4.5 [8].

$$\sigma_{LUB} = \sigma_1 + \left({A_1}/{(1 - \alpha_1 A_1)}\right) \tag{4.2}$$

$$A_1 = \sum_{t=2}^{m} \frac{v_t}{(\sigma_t - \sigma_1)^{-1} + \alpha_1} \tag{4.3}$$

$$\alpha_1 = \frac{1}{3\sigma_1} \tag{4.4}$$

$$\sigma_{HLB} = \sigma_m + (A_m(1 - \alpha_m A_m)) \tag{4.5}$$

$$\alpha_m = \frac{1}{3\sigma_m} \tag{4.6}$$

$$A_m = \sum_{t=1}^{m-1} \frac{C}{(\sigma_t - \sigma_m)^{-1} + \alpha_m} \tag{4.7}$$

To calculate the HLB and LUB conductivities, two key parameters are required, the volume fraction (V_t) of particulate phases and the conductivities (σ_t) of the independent phases. $\sigma_1$should

always represent the phase with the highest conductivity, which is Cu, in the case of CuCr composites. The conductivities used in this study are derived from a previous investigation [7], and as shown in Figure 4.6(b), it is evident that samples with porosity exhibit higher resistivity values compared to the predicted HLB resistivity values (inverse of conductivity). However, for CuCr2 and CuCr3, the resistivity values fall within the predicted window of HLB and LUB. This suggest that CuCr2 and CuCr3 composites possess minimal porosity and can be employed as targets for VAPD coatings.

4.4 Conclusion

The primary objective of the study was to explore the influence of Cr powder shape and distribution on the porosity of CuCr composites. Specifically, two types of Cr powders, A-Cr, and Sp-Cr, were examined. It was observed that A-Cr powder resulted in higher porosity and resistivity compared to Sp-Cr, which exhibited lower porosity and resistivity. In the case of CuCr2 produced with Sp-Cr, the powder distribution used in the present study led to a uniform Cr distribution without increased Cr-Cr sintering. This uniform distribution contributed to improved conductivity in the CuCr2 composite. Resistivity measurement was found to be a valuable indicator of porosity in CuCr composites with known compositions. CuCr2, with ~Cu35Cr65 wt% will be used for producing VAPD CuCr coatings with single targets.

References

[1] Anders, A., 2022. Cathodic Arcs.

[2] Chakrabarti, D.J., Laughlin, D.E., 1984. The Cr-Cu (Chromium-Copper) system. Bulletin of Alloy Phase Diagrams 5, 59–68. https://doi.org/10.1007/BF02868727

[3] Chang, Y., Zheng, W., Zhou, Z., Zhai, Y., Wang, Y., 2016. Preparation and Performance of Cu-Cr Contact Materials for Vacuum Switches with Low Contact Pressure. J. Electron. Mater. 45, 5647–5654. https://doi.org/10.1007/s11664-016-4782-0

[4] Farzadfar, S.A., Murtagh, M.J., Venugopal, N., 2020. Impact of IN718 bimodal powder size distribution on the performance and productivity of laser powder bed fusion additive manufacturing process. Powder Technology 375, 60–80. https://doi.org/10.1016/j.powtec.2020.07.092

[5] Frey, P., Klink, N., Michal, R., Saeger, K.E., 1989. Metallurgical aspects of contact materials for vacuum switching devices. IEEE Transactions on Plasma Science 17, 734–740. https://doi.org/10.1109/27.41194

[6] German, R.M., n.d. Powder metallurgy science.

[7] Klinski-Wetzel, K. v., Kowanda, C., Heilmaier, M., Mueller, F.E.H., 2015. The influence of microstructural features on the electrical conductivity of solid phase sintered CuCr composites. Journal of Alloys and Compounds 631, 237–247. https://doi.org/10.1016/j.jallcom.2014.12.249

[8] Rossiter, P.L., 1987. The Electrical Resistivity of Metals and Alloys, Cambridge Solid State Science Series. Cambridge University Press, Cambridge. https://doi.org/10.1017/CBO9780511600289

[9] Zhou, Z.M., Gao, J., Li, F., Zhang, Y.K., Wang, Y.P., Kolbe, M., 2009. On the metastable miscibility gap in liquid Cu–Cr alloys. J Mater Sci 44, 3793–3799. https://doi.org/10.1007/s10853-009-3511-y

Chapter 5 CuCr Films Deposited Using Composite Target

Abstract

In Chapter 3, VAPD co-deposited CuCr films exhibited a sub-micron layered microstructure, which distinguished them from the nano-layered structures reported with other PVD techniques. Evolution of this microstructure was attributed to high ion energies present with VAPD, providing sufficient adatom mobility for the immiscible Cu-Cr material to grow as two independent phases. To achieve nano-scaled CuCr coatings using VAPD, a single composite target (CuCr2, detailed in Chapter 4) is employed to produce CuCr films in this chapter. The study in this chapter is divided into three parts: Part 1: Composite cathode Cu35Cr65 was used to produce films by varying the DC bias at -20V and -100V. It was observed that at negative bias of -100V, significant Cu self-sputtering occurred due to the high ion energies at higher bias power. Part 2: The same cathode was used to produce coatings, but at different DC pulsed bias voltages. The use of pulsed bias voltages provides high energy without significantly affecting the substrate temperatures, thereby increasing film density without inducing significant self-sputtering of Cu. Part 3: All the CuCr films produced were subjected to vacuum breakdown tests, using a similar setup as that used in Chapter 2, to establish the initial vacuum breakdown performance of CuCr films produced by VAPD. Finally, the breakdown performance of CuCr films was compared with the performance of bulk composite materials.

5.1 Introduction

The film growth rate and microstructural changes in VAPD coatings, with regard to process parameters like arc current and negative bias voltages, have been extensively studied using pure

metal targets. Recently, there has been increasing research on coatings produced from alloy targets. Utilizing alloy targets to create multi-phase coatings helps minimize inconsistencies in coating compositions arising from transient phase transitions during co-deposition caused by miscibility gap or diffusion. Employing alloy/composite targets simplifies the process by eliminating the need for multiple plasma sources to form the required coatings. However, coatings made from multi-phase alloys or composite targets are challenging to develop due to the possibility of preferential erosion of lower melting phase from the cathode, leading to inconsistent compositions in the final films. Some studies have reported a slight increase in the composition of the lower melting point phase in the coatings compared to the starting target compositions, indicating different evaporation rates [23-25]. Therefore, it is crucial to thoroughly study the CuCr cathode erosion behavior and film composition evolution to develop new coatings using composite targets. Most of the research on VAPD using alloy targets (AlCr, NiAl, TiSi) is focused on producing coatings with superior mechanical properties (hardness and corrosion resistance), and there has been little effort to develop highly conductive wear-resistant coatings, which is the primary objective of our current study [37,38].

Another critical parameter to consider for developing VAPD coatings is the effect of negative bias voltage applied to the substrate during deposition. The biggest advantage of VAPD is the high degree of ionization of cathode material, therefore biasing can introduce high directionality and it is very effective in VAPD to manipulate film microstructures when compared with other deposition techniques [3]. With changing negative bias voltage, the ion energies can be increased which effects the film density, deposition rates and microstructure of the coatings. Findings from previous studies on alloy targets [4,27,28] have revealed that higher substrate bias voltage leads to an increase in the content of the higher melting point phase in the coatings,

resulting in an increase in hardness. While this increase in hardness can be beneficial for enhancing arc erosion resistance of CuCr contact materials, it would significantly reduce the film's conductivity. Striking the right balance is essential, particularly for vacuum interrupter (VI) applications, where both hardness and conductivity are critical factors to consider. Therefore, careful optimization of the negative bias voltage is crucial to produce CuCr coatings with appropriate microstructure to achieve desirable properties for VI applications.

Typical, film formation on a substrate during VAPD is considered as energetic condensation, i.e accelerated ions have hyperthermal energies sufficient to promote sub-surface bonds partly from ion implantation or substrate atom sputtering. When the bonding is stronger between condensing adatoms, compared to adatom-substrate, 3-D island growth is promoted, and when condensing adatoms have high affinity towards the substrate a 2D layer by layer growth is promoted. To promote deposition the energetic ion should come to rest on the substrate surface and form a bond. However, not all ions approaching the substrate are deposited and some ions backsputter as neutral atoms. This mechanism is dictated by ion energy, ion incident angle and the temperature of the substrate [3]. High bias power increases ion-bombardment and can alter the preferred orientation of polycrystalline films, increase compressive stress leading to film delamination, and cause significant substrate temperature rise due to atomic scale heating (ASH). Continuous DC bias on the substrate aids ASH phenomena, resulting in increased substrate temperatures and self-sputtering of low melting phase elements in the films. Conversely, using low bias decreases film density and can contribute to higher resistivity. To increase film density without reducing ion bombardment, a pulsed bias supply can be employed, which causes ion bombardment only during the power-ON cycle, therefore reducing substrate heating [1,13,24,32].

This study focuses on films produced by a Cu35Cr65 single target at different substrate biasing conditions, measuring the resistivity and hardness produced CuCr films, and establishing their breakdown performance. Current investigations shed light on the potential of VAPD-produced CuCr films for applications in VI contact materials. The use of a single composite target in the VAPD process opens new avenues for achieving nano-scaled CuCr coatings with high conductivity and hardness which can also be used for various other applications.

5.2 Experimental Procedure

5.2.1 Deposition of CuCr films using single composite target

For the deposition of CuCr films, the CuCr2 composite target, which was produced using Sp-Cr powder in Chapter 4, was installed in the cathode assembly (as shown in Fig 5.1) of a similar deposition setup described in Chapter 3. The deposition parameters utilized for the current study are listed in Tables 5.1. To decouple the influence of ion-incident angle on Cu-sputtering from the films, an initial set of films was produced with substrate rotation, followed by turning off the rotation for samples produced using pulsed bias. For comparison, a repeat of the film at a continuous bias DC of -20V was produced along with pulsed bias samples.

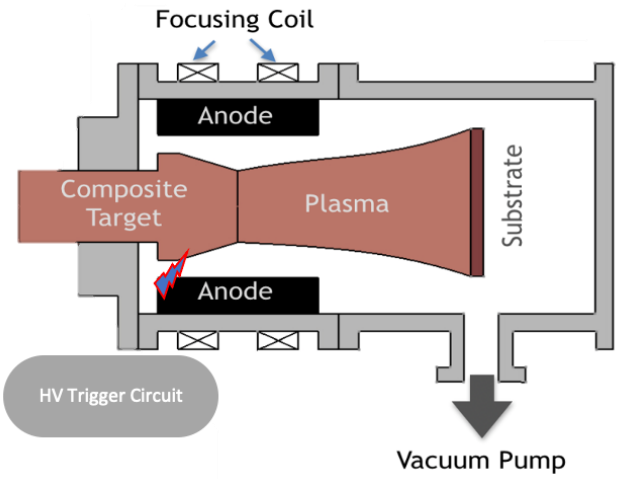

Figure 5.1 Schematic of VAPD deposition used in the study

Sample	Arc current (A)	Bias Voltage	Magnetic Coil Current (A)	Time(min)	Rotation (rpm)
CuCrX	95	-20V DC continuous	1.8	120	30
CuCrY	95	-100V DC continuous	1.8	120	30
CuCrA	95	-20V DC continuous	1.8	120	0
CuCrB	95	-200 V, pulsed DC f=10 kHz, Duty Cycle=10%	1.8	120	0
CuCrC	95	-300 V, pulsed DC f=20 kHz, Duty cycle=15 %	1.8	120	0
CuCrD (CuCr/Cu multilayer film)	CuCr2-95 Cu-90	-200 V, pulsed DC f=10 kHz, Duty Cycle=10%	1.8/1.5	140 (5 alt layers)	0

Table 5.1 Deposition parameters used for producing CuCr films

5.2.2 Microstructural Analysis

SEM, EDX, XRD and residual stress analyses procedures are followed as described in chapter 3.2. Electrical resistivity is measured for CuCr films deposited on non-conducting substrate using 4-point probe as described in chapter 2.2.8. The microstructure of the CuCr films was also investigated using a JEOL-3011 high resolution TEM. TEM-EDX was used to collect the compositional maps and to identify phases. TEM samples of the films were produced by using the cross-sectional mounts used for SEM and were prepared using a focused-ion beam lift-off method using a Helios 650 SEM/FIB.

5.2.3 Breakdown performance

For establishing the breakdown strength, the setup described in section 2.2.10 was employed. However, in contrast to moving the 'W' electrode closer to the film for initiating

breakdown, the gap between electrodes was maintained at fixed distance of 0.05mm and voltage was increased until breakdown occured. The breakdown test was conducted by incrementally increasing the voltage to the circuit by 100V, starting from 3000V, and recording the breakdown voltages for 50 continuous breakdowns after 25 conditioning cycles. Following the breakdown tests, the arc-erosion profile was captured using a Hitachi S2600N SEM. The imaging was performed on samples after 100 breaking cycles to thoroughly assess the arc-erosion profile on the film's surface.

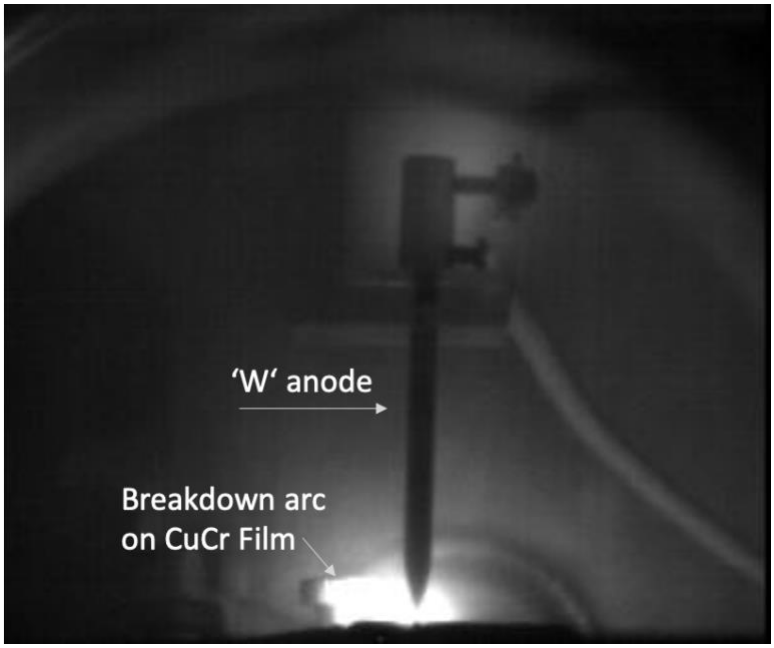

Figure 5.2 Arc generated on the CuCr film during vacuum breakdown test

5.3 Results for CuCr films deposited using continuous bias voltage by single target

Figure 5.3 displays the cross-section SEM images of CuCrX and CuCrY, deposited at -20V and -100V bias voltage, respectively. The EDX analysis of the samples revealed a composition of Cu:Cr of 30:70wt% for CuCrX and Cu:Cr of 9:91wt% for CuCrY. The thickness of CuCrX was approximately 18µm, while CuCrY was 12µm thick. A comparison of compositional analysis and

thickness revealed that at higher bias voltage, Cu retention is low. Also, there is 5% loss of Cu content compared to the target composition for CuCrX.

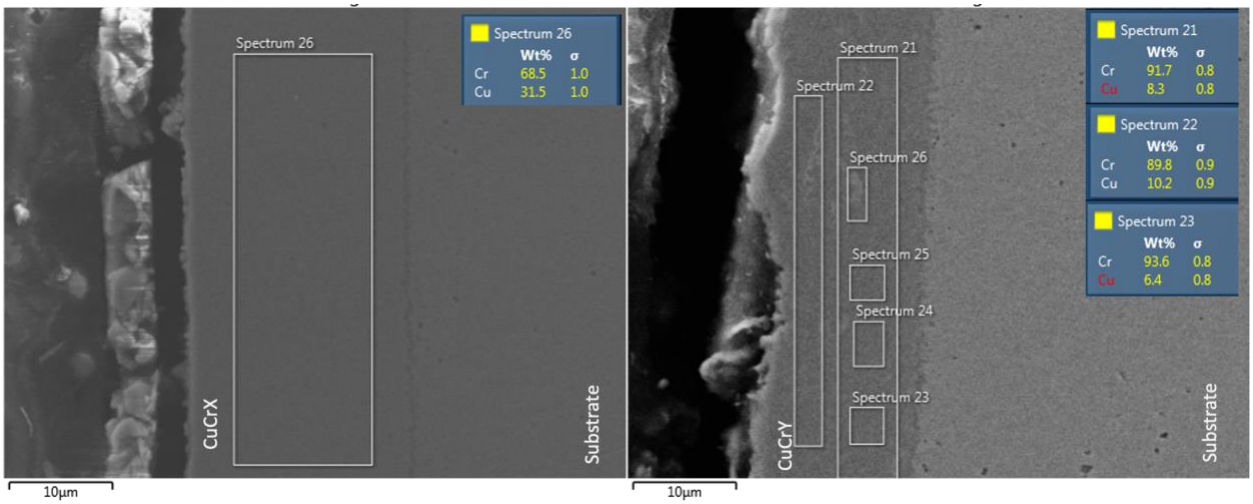

Figure 5.3 Cross-section image of a) CuCrX(-20V) b) CuCrY(-100V)

Figure 5.4 shows the XRD spectra of the deposited films, and for CuCrY, the Cu peaks are completely absent. While CuCrX exhibits small intensity Cu peaks. This observation is consistent with the literature on CuCr thin films, which often lack distinct Cu-Cr peaks due to nanoscale mixing phase separation during deposition.

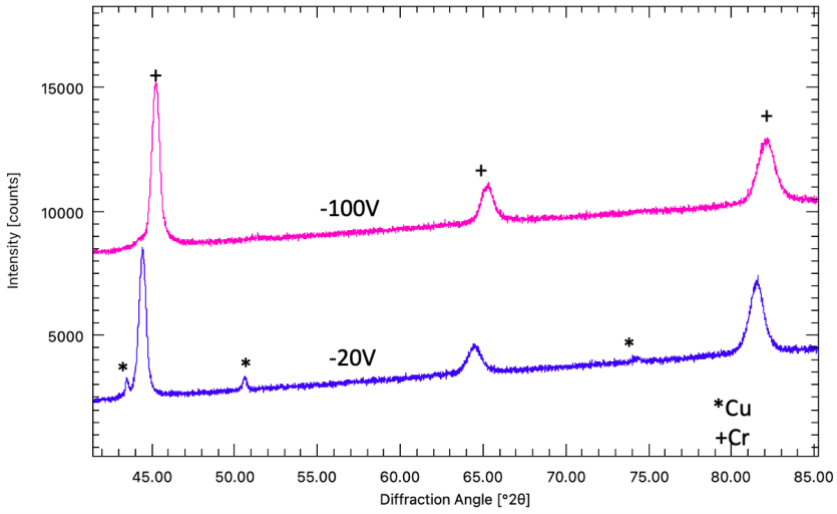

Figure 5.4 XRD pattern of the CuCr films produced at different DC bias (continuous)

The residual stresses measured for the films are presented in Figure 5.5. CuCrX exhibits tensile stresses of 2408 (±430) MPa, while CuCrY shows compressive stresses of -1784 (±189) MPa. These findings are consistent with the observations that higher continuous DC bias leads to significantly increased ion bombardment, causing compressive stresses and sputtering of the low melting point Cu [2,3]. This can be further confirmed by lower Cu content by EDX analysis, and the lower thickness observed for CuCrY. To explain the loss of Cu at high bias voltages, TIMS calculations was performed, using CuCr65 as the substrate material and ion energies of 100eV for Cr and 54eV for Cu (typical for 100A arc currents [41]). The calculations revealed that under energetic ion-bombardments, an average of 0.5 atoms/ion of Cu is sputtered from the substrate compared to <0.1 atoms/ion of Cr. Consequently, a higher amount of Cu is sputtered from the surface in comparison to Cr.

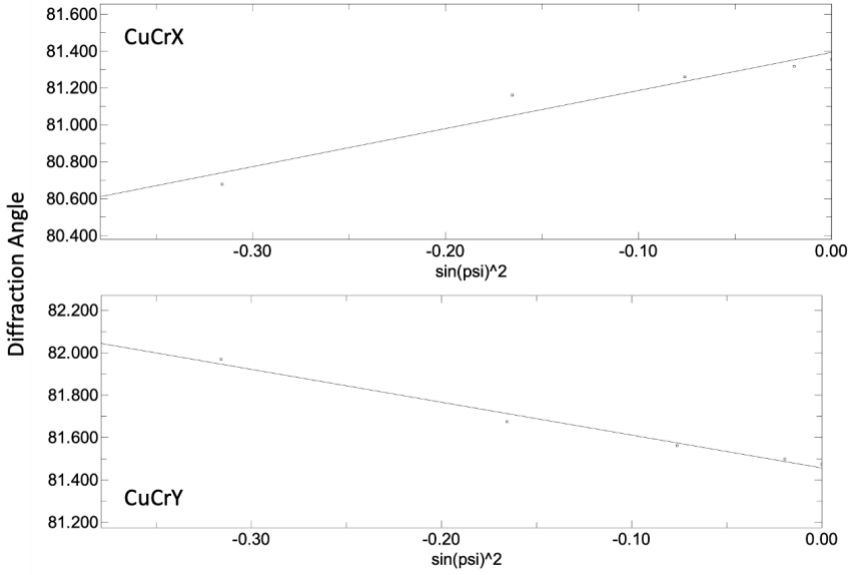

Figure 5.5 Residual stress measurements on CuCr films deposited at different DC bias (continuous)

The recoil depth for surface atoms, resulting from the energy transfer from bombarding ions is illustrated in Fig 5.6. It is evident that at high energies, the recoils are transferred to a depth of 20Å from the film surface, with recoil energies of 10eV/Å-ion. Considering that the deposition

rate for current films is approximately ~25Å/s, this is close to the recoil depth, and as a result, recoil energies are sufficient to fill any vacancies in the atomic structure caused by ion-bombardment, leading to a denser packing of the films.

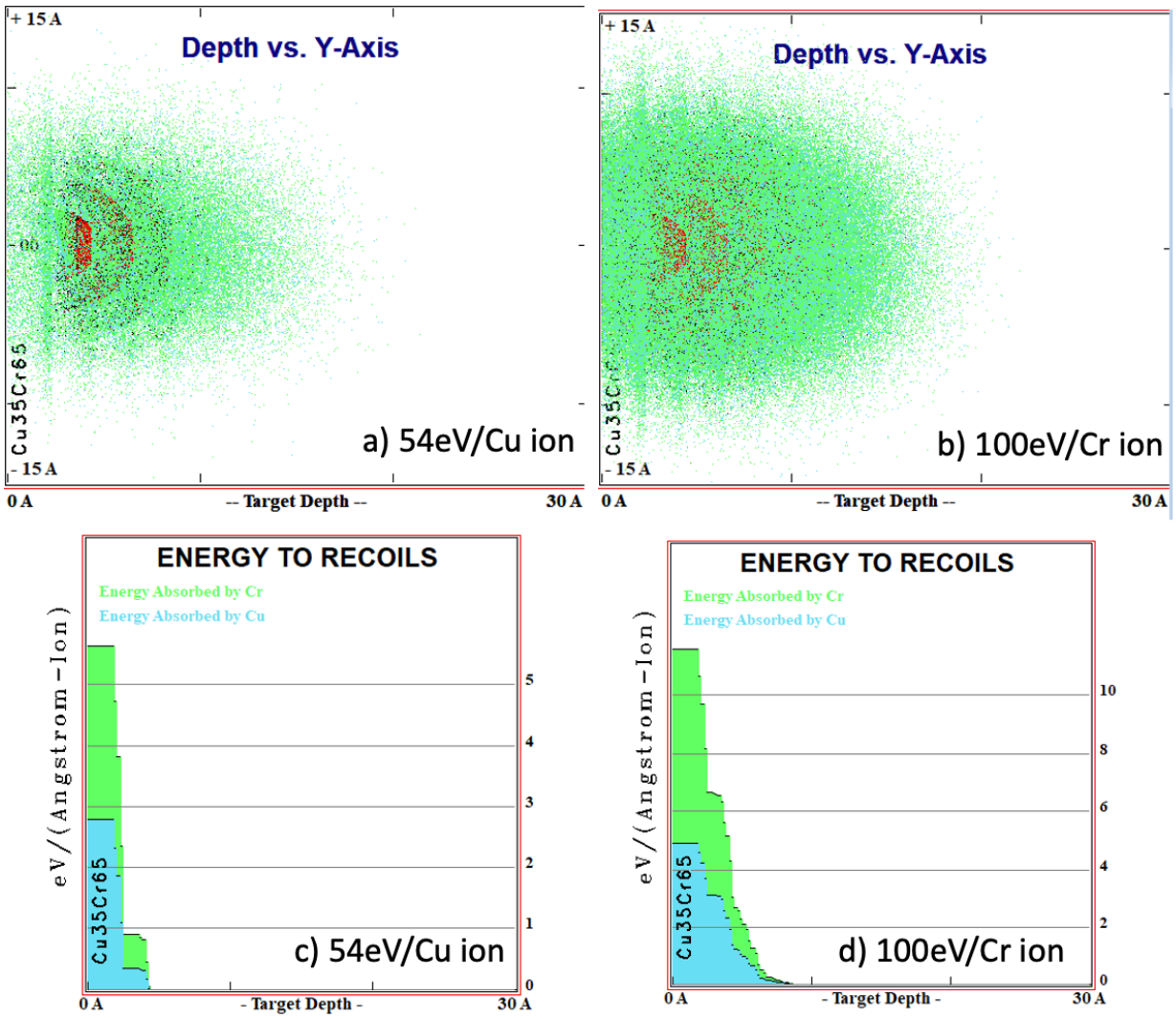

Figure 5.6 a) Map of surface atom (Cu35Cr65film) recoils by Cu ion bombardment b) Map of surface atom (Cu35Cr65film) recoils by Cr ion bombardment c) Ion energy transfer from Cu (54eV) ions to deposited CuCr film d) Ion energy transfer from Cr ions (100eV) to deposited CuCr film

5.4 Results, Comparisons and Discussion for CuCr films produced by pulsed bias

This section presents data for CuCr films deposited using a single composite target at different DC pulsed bias voltages and compares the results with a continuous DC bias voltage sample, which was re-run to achieve a composition closer to the target. All the samples were

prepared without substrate rotation. The use of pulsed bias voltages provides high energy without significantly affecting the substrate temperatures, thereby increasing film density without inducing significant self-sputtering of Cu, which was observed in films deposited at continuous DC bias of -100V.

5.4.1 Surface morphology of CuCr films deposited at different bias voltages

The surface morphology of the CuCr films obtained from a single target deposition is depicted in the figure 5.7. Droplet inclusions on the surface of the films are mostly smaller than 1 μm in size, and the sample deposited at a higher bias voltage (-200V) demonstrates slightly higher droplet inclusions. To minimize the impact on droplet production, the arc current, Ar gas flow, and magnetic coil current were kept constant throughout the experiments. It is demonstrated that by steering the arc using axial magnetic field, the droplet compositions contain both Cu and Cr phases, providing evidence that no preferential erosion is occurring under the current parameters. It is known that reducing the arc current can lead to a decrease in droplet inclusions within the coatings. This is attributed to a decrease in current density at the cathode spot, resulting in reduced thermal burden around the spot area, which results in reduced cathode erosion and improved temperature management at the arc attachment site [31,34]. Therefore, if the current film breakdown performance is unsatisfactory, reduction in arc current can be implemented. However, lowering the arc current to mitigate droplet inclusions in the coatings may also decrease the deposition rate, which may not be desirable for VI applications where higher film thickness is necessary for desired performance.

Typically, microparticulate (or droplet) inclusions are reported to decrease with increasing negative bias voltage [9,21,34]. This is attributed to the negative charge carried by the droplets in the plasma, causing electrostatic repulsion towards the negatively biased substrate. The criterion

for repulsion is described by equation 5.1, which considers parameters such as radius (R), density (ρ), velocity of the macroparticle droplet (v), electron temperature, and a process constant (β), which depends on factors such as cathode area, arc current, ionization factor, permittivity, and Boltzmann constant [3,4]. In the current study, as the same cathode area and arc current are used it is assumed that β remains constant. The average composition of the droplets in both samples is measured to be similar, with Cu27% and Cr73% for CuCrA and Cu28% and Cr72% for CuCrB. Therefore, the mass of similarly sized macroparticles should be the same.

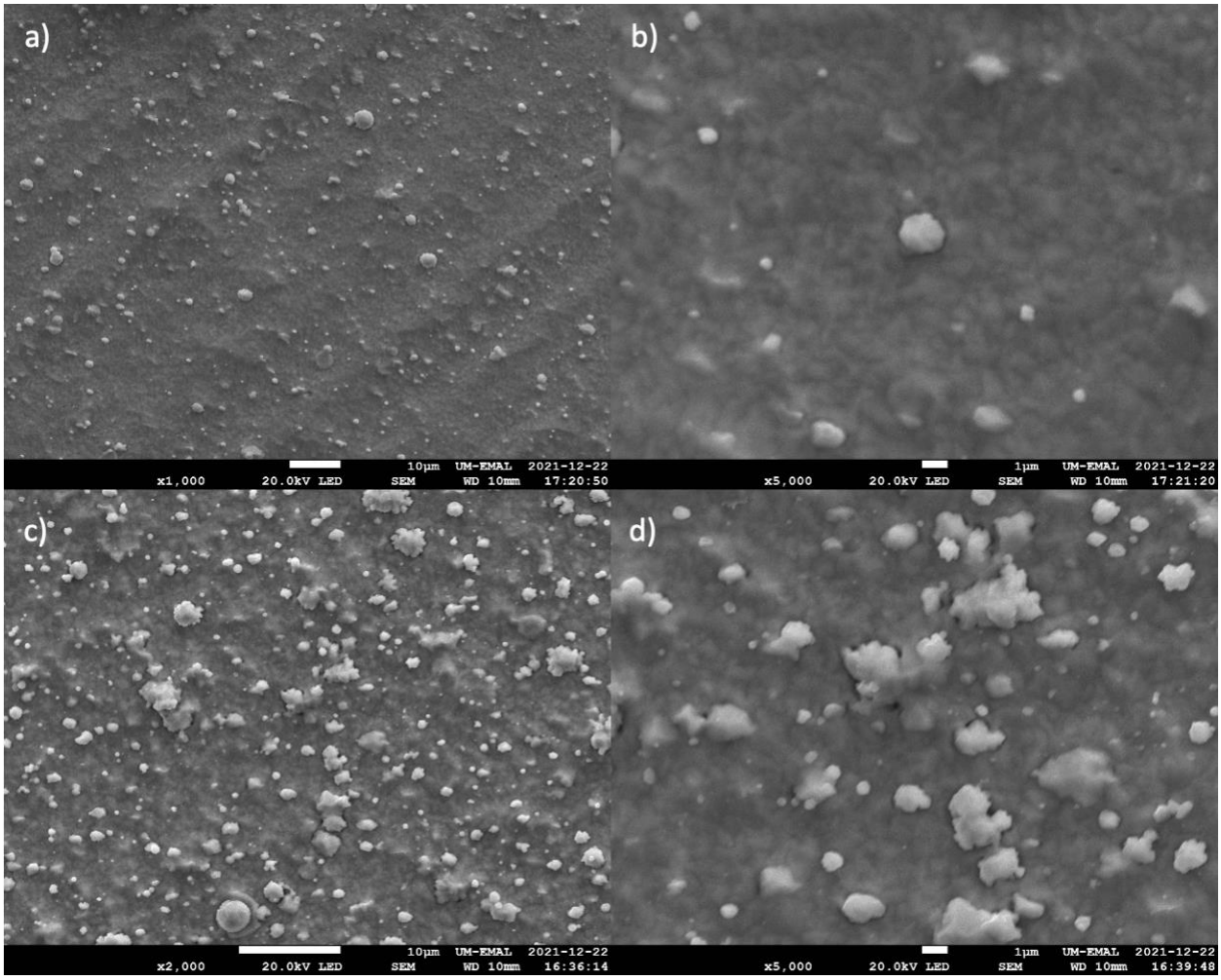

Figure 5.7 a,b) Surface morphology of CuCrA (-20V, continuous DC) at 2kx & 5kx and c,d) CuCrB (-200V, pulsed DC) at 2kx & 5x

The variation in macroparticle velocity may arise from differences in particle size, as described in equation 5.1. From image 5.7(d), it can be observed that the droplets appear more coalesced in the sample deposited at a higher bias voltage of -200V compared to the sample deposited at -20V. This suggests that at certain deposition conditions which promote coalescence behavior of the generated droplets the repulsion criterion may not be satisfied. Hence, the probability for repulsion with increased negative bias will increase only for smaller droplets in the plasma but not for the larger coalesced particles.

$$(R\rho v^2)_{macroparticle} < 3V_{bias}\left(\frac{T_e}{V_{ion}}\right)^{1/2}\left(\ln\left(\frac{{v_{ion}}^2}{T_e}\right)\right)\beta \tag{5.1}$$

Particle coalescence observed during deposition process could be attributed to the use of shorter pulse time or duty cycle for the -200V DC bias compared to the continuous -20V DC bias. It has been observed that the number of macroparticles decreases with an increase in negative bias pulse time [31,33]. Droplets are typically negatively charged due to collisions with high-temperature electrons in a plasma. As a negatively charged droplet approaches the plasma sheath, its velocity is significantly reduced due to interaction with the sheath's electric field. This interaction can last for a few 10's of μs, and if the droplet has sufficient residence time in the sheath, it can gain a positive charge and accelerate toward the negatively biased substrate surface. However, with shorter residence time in the sheath, not all of the negative charge on the droplet is lost, resulting in repulsion from the substrate. At higher bias voltages, the residence time in the sheath is insufficient to remove the negative charge and this leads to lower macroparticle density on the films. Additionally, the time required for the macroparticle to completely drop its acquired charge in a plasma, can also depend on its size, plasma velocity (v_p), and ion charge and density (n, z), as approximated by eq 5.2. In the case of a pulsed power supply, the sheath's ion currents,

and potential can vary based on the pulse frequency. If the pulse time is too long, the sheath may have higher ion currents, and the droplet will have sufficient time to completely lose its negative charge in the sheath. This can result in the attraction of other negatively charged droplets onto the positively charged droplet surface, leading to coalescence during the power-off cycle. In the present power supply setup, the pulse time for negative DC supply is 10µs, and it is possible that a higher pulse frequency is required to eliminate the inclusion of droplets at -200V bias [9,33].

$$t_r = \frac{Q_{macroparticle}}{znev_p A_{macroparticle}} \tag{5.2}$$

Sample	Cu (%)	Cr (%)	Std. Dev (%)	Ra(nm)	Rz(nm)
CuCrA	16	84	0.4	39	52
CuCrB	22	78	0.75	51	60
CuCrC	2	98	0.2	75	86
CuCrD	19	81	0.2	65	77

Table 5.2 Compositional analysis (EDX) & Surface roughness measurements (AFM) of CuCr films

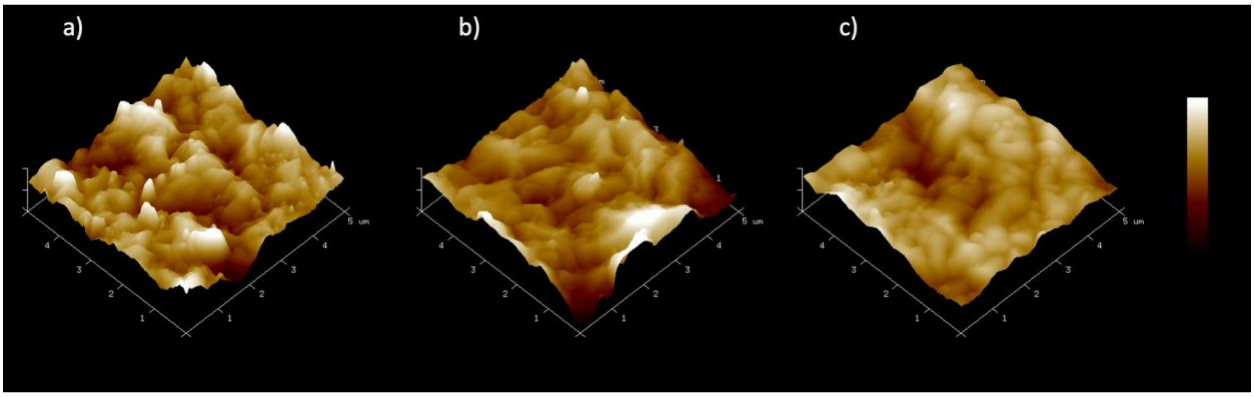

Figure 5.8 AFM images of a) CuCrA (-20V, Cont.) b) CuCrB(-200V,pulsed) c) CuCrC (-300V, pulsed)

Table 5.2 presents the film composition and surface roughness of the CuCr films obtained at different bias voltages. CuCrC sample, deposited at the highest bias voltage of -300V, exhibits the lowest Cu% in its composition. While the other samples, CuCrA and CuCrB, show comparable Cu% values ranging from ~16-22%. The reduced Cu content when compared to the composite

target can be attributed to the high self-sputtering yield of Cu, which becomes more significant at elevated ion energies and substrate temperatures. Surface roughness measurements indicate that the values are comparable among the samples and varying within a few 10's of nanometers. However, the surface features (fig 5.8) of the CuCrA sample deposited at lower bias voltage exhibit slightly smaller sharp peaks compared to the other samples. While CuCrC sample deposited at higher bias voltage show somewhat larger and more rounded surface features. This can be attributed to the combination of lower Cu% composition and higher substrate temperatures, which allow the Cr grains to grow more freely without restrictions in absence of the Cu phase.

5.4.2 Compositional Analysis of CuCr Films

Figure 5.9 displays the cross-sections of the CuCr films, and their corresponding film thicknesses are: CuCrA 18µm, CuCrB 7µm, and CuCrC 14µm. The sample deposited at lowest bias voltage exhibits higher thickness compared to other samples. Typically, as the bias voltage increases, the ion energies also increase, resulting in increased sputtering of the deposited film. Consequently, the density of the film is expected to increase and decrease in film thickness can be expected. However, it is surprising that CuCrB has 50% thickness lower than CuCrC, deposited at a higher bias voltage. This may suggest that when the droplet contamination on the surface becomes very high, it can render the surface non-conducive for further deposition. The films were analyzed using EDX and the composition was measured at various film thicknesses. For CuCrA, the surface composition was found to be Cr:Cu at 85:15 wt%, while the composition at 1 µm from the substrate was Cr:Cu at 67:33 wt%. For upto 5µm from the substrate, composition gradually changed with increasing film thickness, showing an increase in Cr% and a decrease in Cu%. Between 5-18 µm film thickness, the composition variation settled down to the surface

composition of Cr:Cu at 85:15 wt%. The average cross-sectional composition was determined to be Cr:Cu at approximately 75:25 wt%.

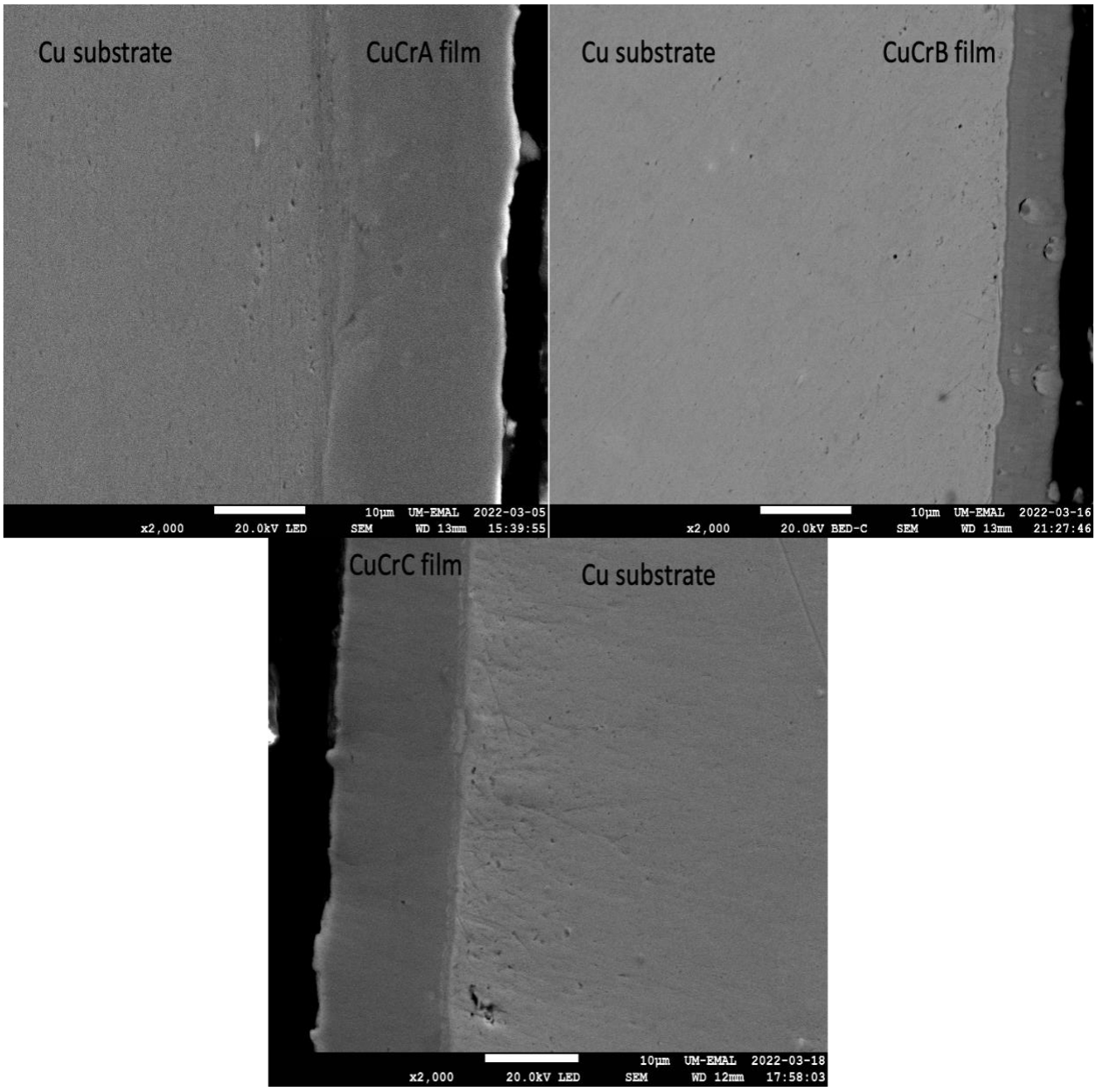

Figure 5.9 AFM images of CuCrA (-20V, Cont.), CuCrB (-200V, pulsed) & CuCrC (-300V, pulsed)

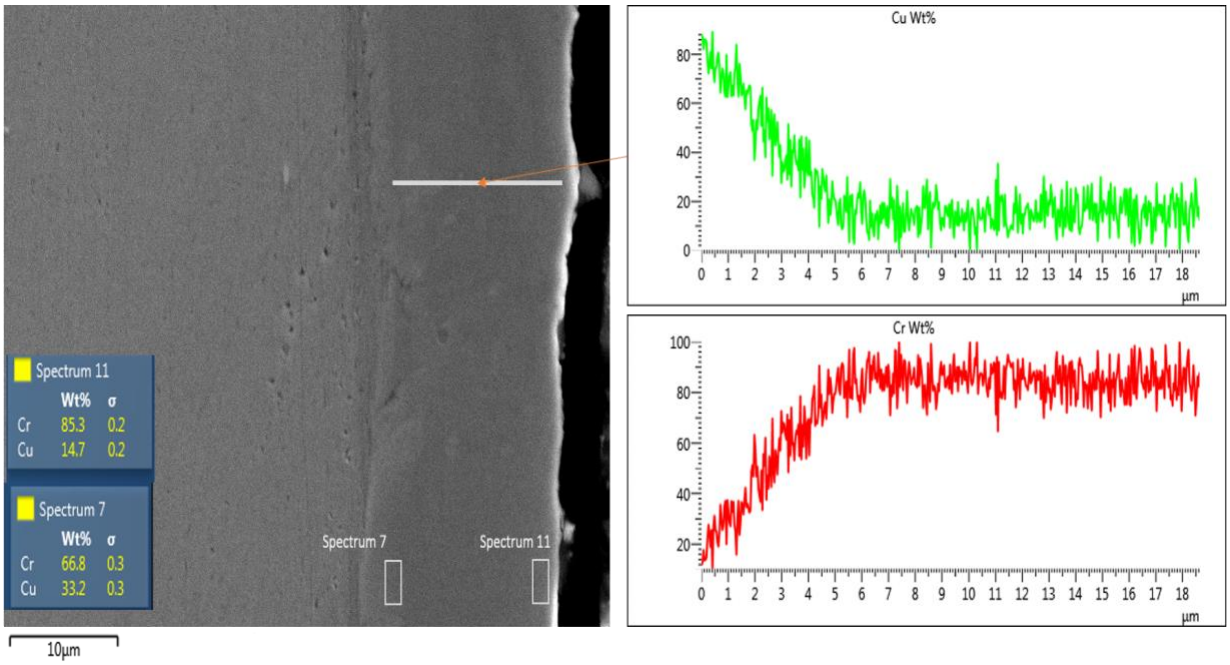

Figure 5.10 EDX analysis of CuCrA (-20V, continuous DC) with line scan shown on the right

CuCrB exhibited less compositional variation compared to CuCrA. The average cross-sectional composition for CuCrB was Cr:Cu at approximately 73:27 wt%. The composition started at Cr:Cu 70:30 wt%, at 1 µm from the substrate and varied to Cr:Cu 75:25 wt% at the surface. CuCrC, deposited at a high pulsed bias voltage of -300V, displayed a significant difference in composition compared to the other films. The average cross-sectional composition for CuCrC was Cr:Cu at approximately 93:7 wt%, stabilizing at around 3 µm from the substrate and reaching Cr:Cu 97:3 wt%. This indicates that at high pulsed negative bias, sputtering conditions increases, and the Cu retention decreases significantly. It is also noteworthy that CuCrB sample exhibited a higher droplet inclusion in cross-section compared to other samples, just as prominently observed on the film surface.

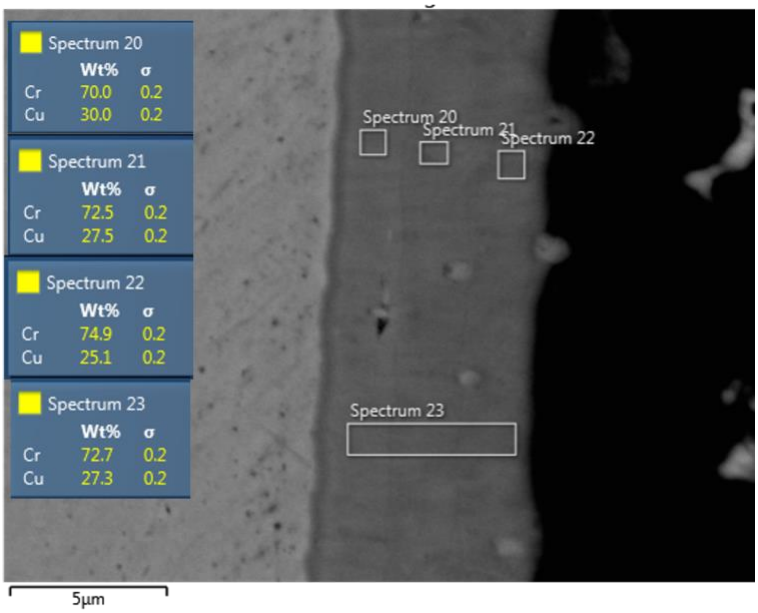

Figure 5.11 EDX analysis of CuCrB (-200V, pulsed)

In VAPD, the plasma itself condenses on a substrate to create a film. Arc-plasma contains ions that move at supersonic velocities and carry multiple charges. As a result, they impart high kinetic and potential energies to the depositing film. These ions have energies in the range of 10's eV or even higher for refractory metals, leading to atomic scale heating (ASH). ASH can cause a decrease in deposition efficiency, as the bombardment of high energy ions increases causes sputtering of depositing species. As sputtering increases, neutral atoms are ejected from the deposited film. With the increase of substrate bias voltage, the established plasma sheath characteristic also changes. Sheath region between the substrate and arc plasma establishes a potential difference, and a minor shift in sheath voltage alters condensing ion energies substantially (eq 5.3). Where, ε_i is the energy of the arriving ions, ε_i is the energy gained by the ions from cathode arc, e is the elemental charge and Q is the charge state number [3,5,9]. By increasing the negative bias on the substrate, the sheath voltage increases (eq. 5.4), leading to higher ion energies and increased sputtering due to ASH. When depositing CuCrC or CuCrY sample at high bias voltage, it experiences higher ASH and has the lowest Cu content, as Cu has a higher sputter yield

compared to Cr. It is worth noting that even at lower substrate bias voltages, such as in the case of CuCrA, the substrate temperature increases with longer deposition times due to ASH, resulting in decreased Cu retention caused by sputtering due to high substrate temperatures.

$$\varepsilon_i = \varepsilon_{io} + QeV_{sheath} \tag{5.3}$$

$$V_{sheath} = V_{Plasma} - V_{substrate} \tag{5.4}$$

From eq 5.3 & 5.4, when the biasing is switched OFF during deposition, the energy of the ions travelling out of the sheath is reduced. For the current power supply, the effect of bias is only for 10μs/1ms pulse, therefore using a pulsed supply for biasing reduces the effect of ASH and increases the Cu retention in the films (CuCrB).

5.4.3 Microstructure evolution of CuCr films

Figure 5.12 illustrates the XRD patterns of the CuCr films prepared under various bias voltages. Except for CuCrC sample, the other two samples exhibit a surface composition containing more than 15% Cu. However, the XRD patterns do not prominently display the corresponding Cu peaks. CuCrB sample, which has a higher surface Cu content, shows broadened peaks for Cu(111), Cu(200), and Cu(220). CuCrA samples displayed an elongated signal for Cu(111) peak, which combined with the adjacent Cr(110) peak. This could be an indication for presence of a non-equilibrium CuCr phase. All samples exhibit broadened peaks for Cr(110), Cr(200), and Cr(211) with moderate shifts, indicating the presence of nanocrystalline or non-equilibrium phases within the immiscible Cu-Cr system. Samples with nano-scale mixing or spinodal decomposition, diffract to a single Bragg's peak, which appears at an angle corresponding to the average lattice parameter of the two elements [ma]. CuCrC sample demonstrates very low peak intensity for the Cr(200) orientation when compared to other two samples, and for all samples, the preferred growth orientation is Cr(110), followed by the Cr(211) crystallographic

orientation. The XRD patterns agree with the previous studies performed on CuCr films using other PVD techniques [19,36].

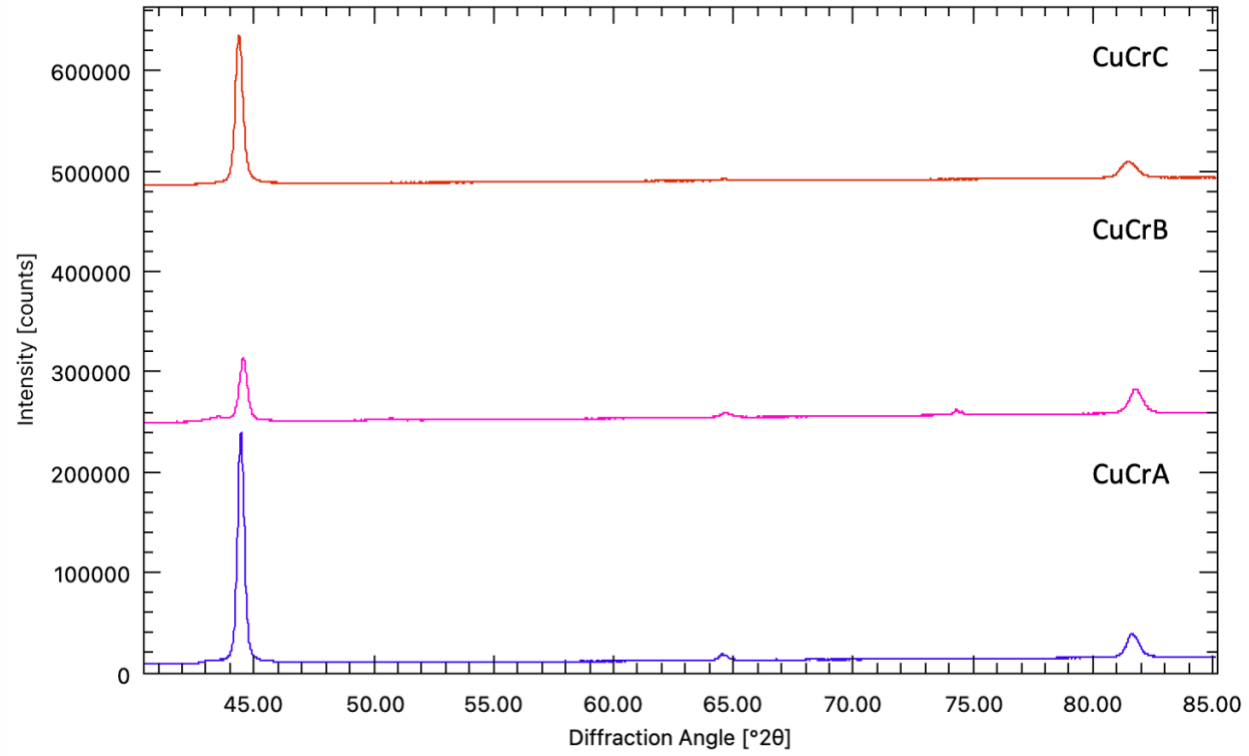

Figure 5.12 XRD patterns of CuCr films

In contrast to co-deposited CuCr films with high Cu content (from Chapter 3), for current films distinguishing between the Cu and Cr phases in SEM images becomes challenging. This is because using single target facilitates atomic scale mixing of Cu and Cr phases and produces films with grains in much smaller scale than co-deposition (shown in TEM images). Figure 5.13 & 5.14 presents the HAADF-TEM images of the films produced under different bias conditions, -20V bias for CuCrA and -200V bias for CuCrB. Notably, CuCrB exhibits a distinct multilayered structure, whereas CuCrA displays a smaller and unevenly distributed multilayered structure, which is not distinguishable in certain areas of the film. EDX mapping confirms the difference in

z-contrast arises form signals for phase separated individual Cu and Cr layers.

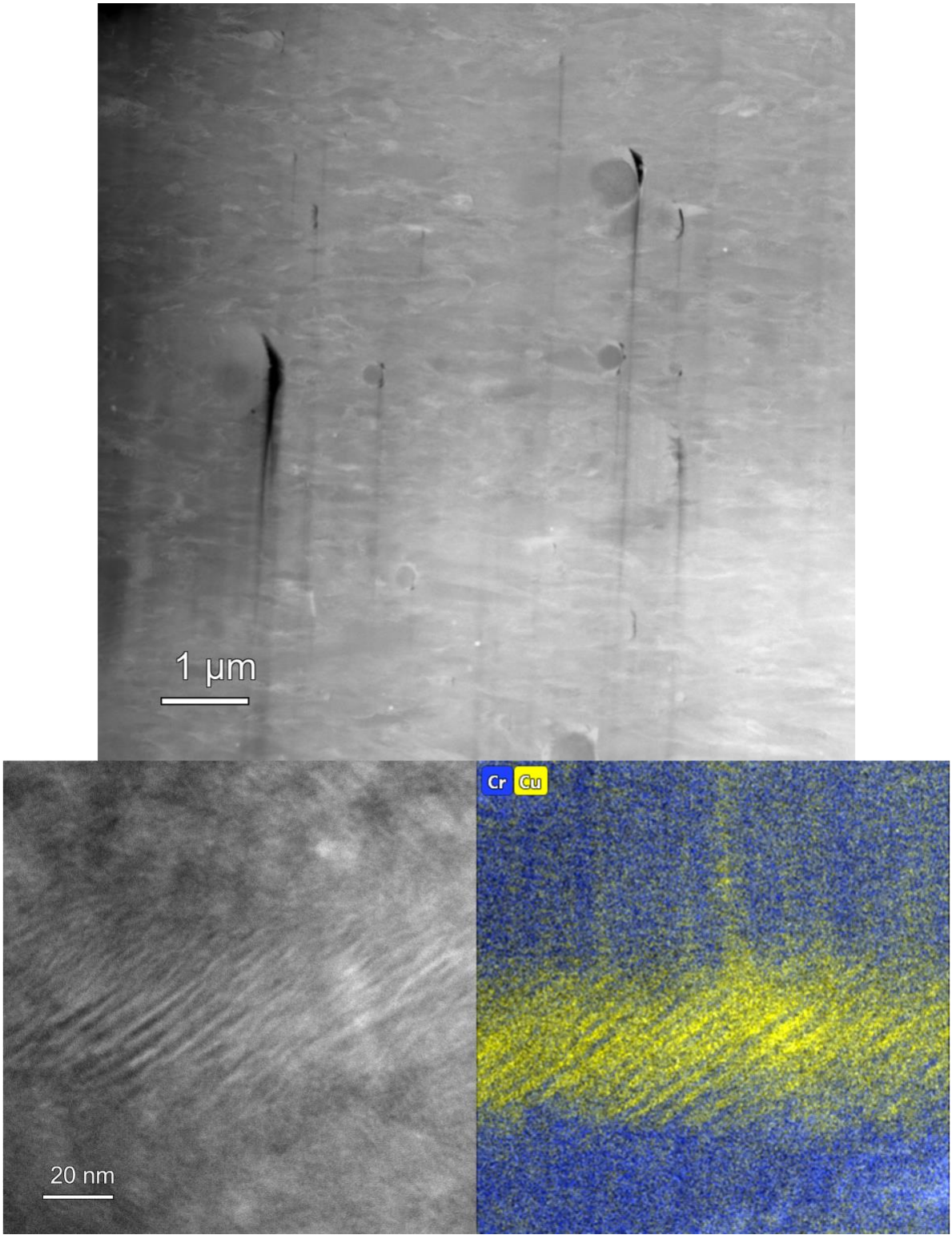

Figure 5.13 TEM-HAADF image of CuCrA

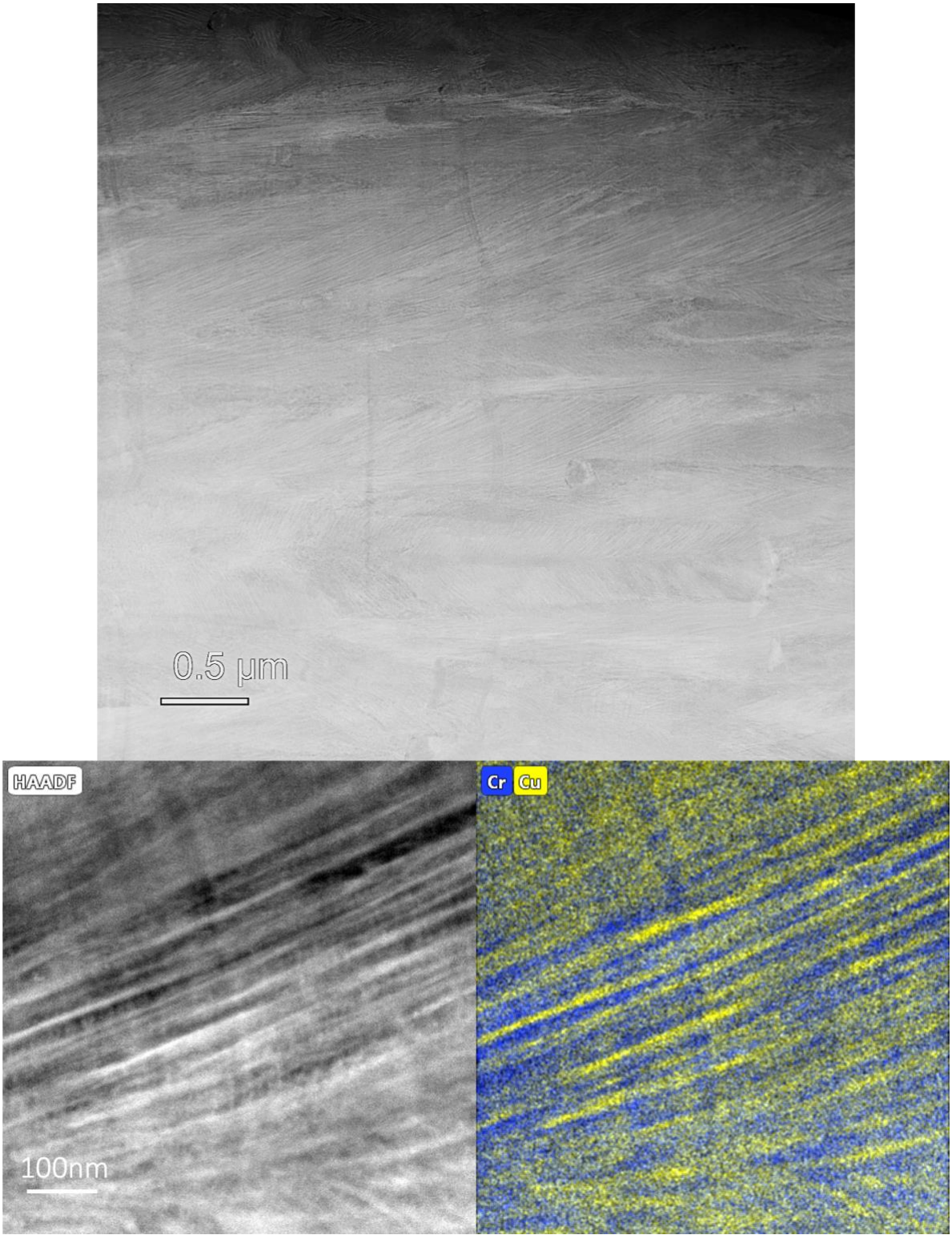

Figure 5.14 TEM-HAADF image of CuCrB

The formation of layered structures in CuX (X: Cr, W, V) systems, has been observed in various published studies utilizing sputtering or other PVD techniques [14,18,36]. CuCr systems have positive heat of mixing ($\Delta H = 12kJ/mol$) and are known to phase separate even with non-equilibrium processing techniques, because of the competition between instantaneous decomposition (spinodal-like) and strain energy reduction created my lattice mismatch. This enables the formation of self-assembled multilayers of immiscible element [25,35,37].

In VAPD, the continuous bombardment of ions on the film surface not only imparts additional energy to the condensed surface atoms but also increases defect formation. Thereafter, facilitating the diffusion of surface atoms during the deposition process. The average energy of deposited atom is given by $< E >= E_i(Ji/Jm)$, where E_i is the average ion energy and Ji/Jm is the ratio of the energetic ion flux to the flux of condensing atoms [30]. Depending on the activation energies involved, there are three potential pathways for diffusion between the surface and condensing atoms. Cu-Cr interdiffusion is known to be very slow [diffusion article] compared to the self-diffusion of either phase [6,12]. Typically, Cu self-diffusion exhibits the lowest activation energy, with values below 2eV and even below 1eV for nanocrystalline Cu phases, while Cr diffusion requires more than 3eV. If the condensed film material has a non-equilibrium composition that is bcc-rich in Cr(Cu) or fcc-rich in Cu(Cr), each phase will diffuse into its own pure phase and modulate into a layered structure. Increasing the bias voltage enhances self-diffusion (as the energy of the deposited material increases), leading to the formation of continuous layered structures, as observed in CuCrB. On the contrary, at low bias voltages, the mobility of ions and surface atoms is limited, resulting in the formation of shorter discrete layers in CuCrA. The approximate diffusion distance L of both Cu and Cr can be estimated using the following two equations:

$$L = \sqrt{2Dt} \tag{5.5}$$

$$D = D_0 e^{\left(-Q/RT\right)} \tag{5.6}$$

Where D is the diffusion co-efficient, T is the deposition temperature, R is the universal gas constant, D_0 is the pre-exponential factor, Q is the activation energy for diffusion and t is the deposition time. Towards the end of the deposition process, the substrate temperature for the sample biased at -20V DC should be approximately 300ºC, while the temperature for the -200V pulsed DC sample may be slightly higher ~350-400ºC [13,32]. The calculated diffusion distances are shown in Table 3 [12,27], indicating that the initially deposited phases can undergo short-scale diffusion throughout the process. This could explain why the CuCrB XRD peak exhibits distinct Cu peaks with longer nanoscale structures, unlike CuCrA. It is important to note that the calculated diffusion distance values have a range of values due to variations in diffusion coefficients reported in previous studies [6].

	300ºC	400ºC
Cr in Cu	~1nm	16-22nm
Cu	1-3nm	26-100nm

Table 5.3 Diffusion lengths calculated for Cr/Cu interdiffusion and Cu self-diffusion

Another explanation for the formation of layered structures can be attributed to the deposition rate of the films. Previous findings on sputtered immiscible binary systems have demonstrated that the final phase-separated morphology in systems with limited solid solubility, such as CuCr, is influenced by the competition between surface diffusion length and deposition rate. There are three prominent morphologies that can form: lateral compositional modulation (LCM), vertical compositional modulation (VCM), and random compositional modulation (RCM) [5]. The LCM morphology is typically observed when the phase-separating boundaries are

oriented perpendicular to the substrate surface or aligned with the film growth direction. In the VCM morphology, the phase-separating boundaries are oriented parallel to the substrate, in a direction perpendicular to the film growth. For CuCr films produced by VAPD, the feature domains that are Cu-rich or Cr-rich with domain boundaries aligned at an inclined angle to the flat substrate, exhibit characteristics more similar to LCM structures. When spinodal decomposition occurs more rapidly than the film deposition rates, the concentration variations of the two phases cannot develop parallel to the film growth direction. As a result, the CuCr condensing material phase-separates in the vertical direction (perpendicular to the film surface), forming LCM structures. The new condensing layers are always in contact with decomposed LCM layers, in which the Cu-rich and Cr-rich regions have already reached concentrations outside the spinodal region. Therefore, there is no uphill diffusion between the freshly deposited layers and the existing layers. The morphological pattern developed in the existing layers serves as a template, guiding the decomposition of the fresh layers.

5.4.4 Properties of CuCr Films

The figures 5.15 & 5.16 illustrate the measured resistivity, residual stresses, and microhardness of the films. It is evident that all films exhibit residual tensile stresses and repeating the repeat tests of the samples yielded similar results. The CuCrC sample, which has a higher Cr% (~97%), demonstrates the highest average tensile stress of 1830 MPa (±380). This value is higher than the tensile stress observed in pure Cr films [14]. High residual stresses have been observed in both MBE and sputtered films of Cr, and these stresses have been attributed to the low atomic mobility and long columnar grains. The inability to transition from columnar growth in predominantly Cr films at a -300V pulsed bias voltage results in the retention of a columnar microstructure, as indicated by the structure zone diagram. Columnar grains typically exhibit low

density and higher intergranular porosity, leading to elevated tensile stresses [17,28]. In comparison, the tensile stresses are reduced in CuCrB (466±120 MPa) compared to CuCrA (1331±194 MPa), despite both samples having similar average compositions. This lowered stresses in CuCrB, can be attributed to the higher ion bombardment at the -200V pulsed bias voltage, which increases the density of the CuCrB film. The enhanced density contributes to a reduction in tensile stresses compared to CuCrA. Overall, the reported stress values are comparable to those reported for CuCr films with similar compositions [17].

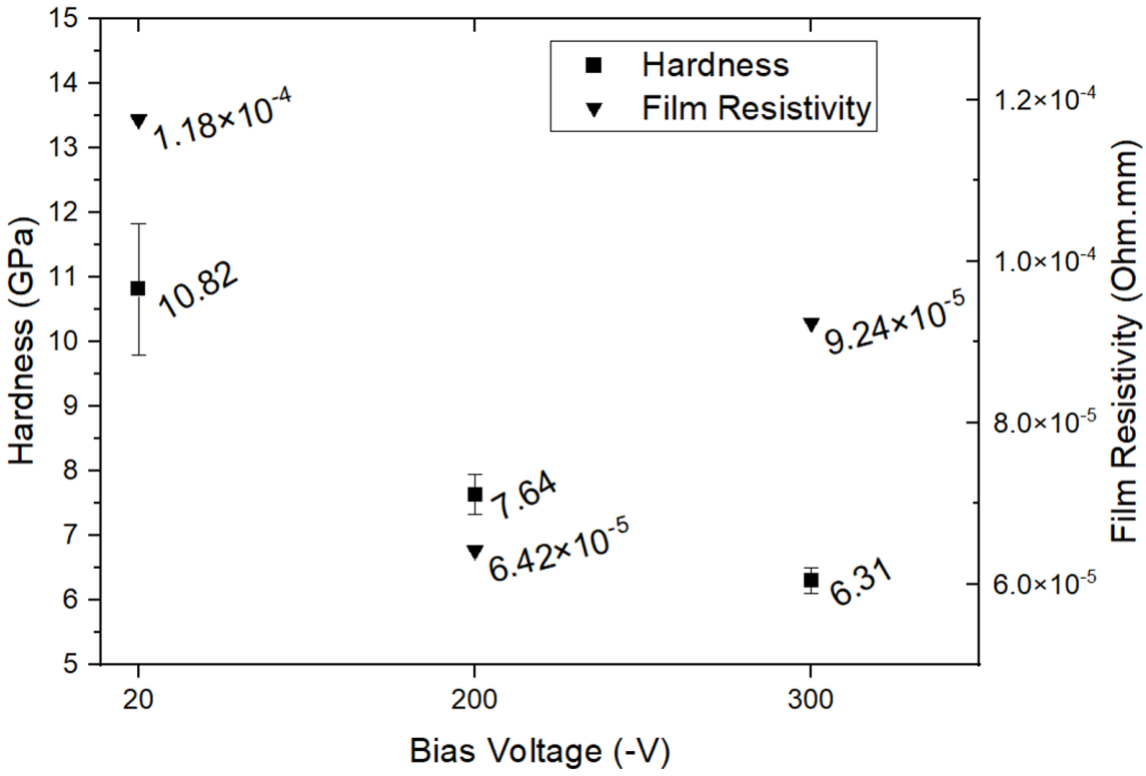

Figure 5.15 Hardness and Resistivity measurements of CuCr films

Hardness measurements were taken on the cross-section of the thin films, with at least 10 readings taken at distances approximately 1µm away from the substrate and top surface. 8mN load was selected to minimize the width of the tip indentation to around 1µm. The CuCrA sample exhibited the highest hardness of 10.9±0.3 GPa, followed by CuCrB with 7.6±1 GPa, and CuCrC

with 6.3±0.2 GPa. The resistivity of the films followed a different trend, with the CuCrB sample demonstrating the lowest resistivity, followed by CuCrC and then CuCrA.

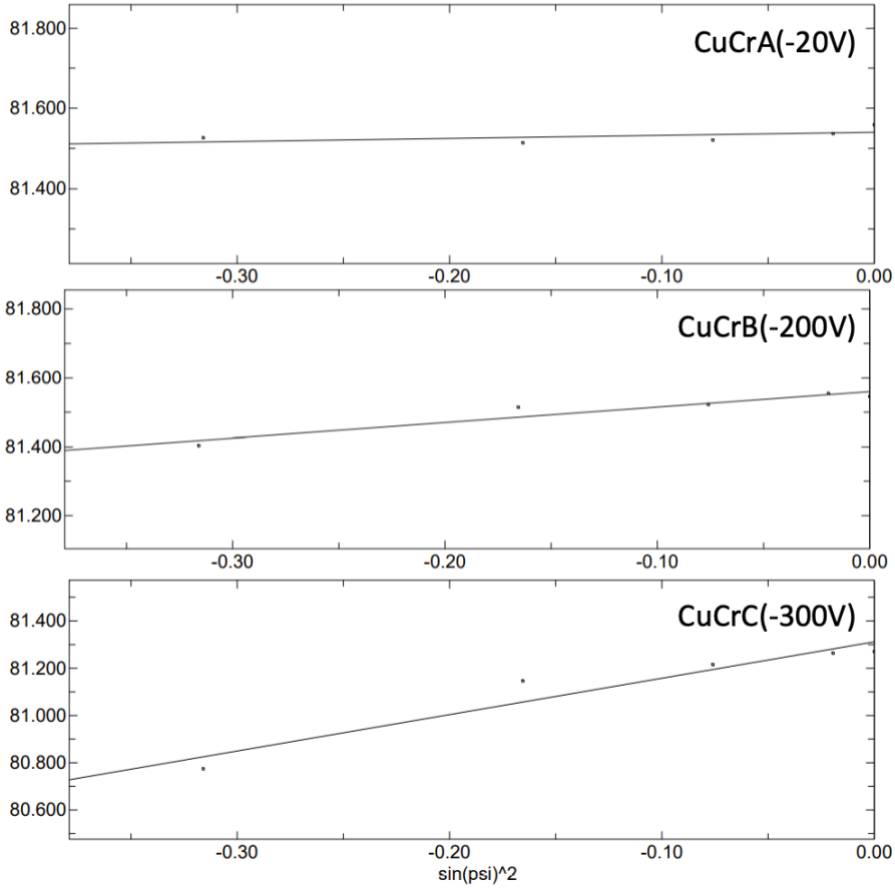

Figure 5.16 Residual stresses for CuCr films

The observed differences in the film properties can be explained using the structure zone diagram, which considers both thermal and ion-bombardment induced mobility [3,19]. Figure 5.17 illustrates that at lower levels of ion bombardment, the transition zone T is small or even nonexistent. However, as the ion bombardment energy increases, the width of zone T expands while zone 1, characterized by fibrous grains with low film density and high voids, decreases. Zone 1 is particularly prevalent at lower homologous temperatures T* ($T_{substrate}/T_{melting\ point}$). By applying a bias voltage, the introduction of ion bombardment on the surface increases, consequently raising the substrate temperature due to atomic surface heating (ASH). It should be

noted that using a continuous DC bias voltage will have a greater impact on the substrate temperature compared to a pulsed DC bias voltage of the same magnitude. Previous studies suggest estimated substrate temperatures of ~300ºC for CuCrA, 400ºC for CuCrB, and 450ºC for CuCrC. Considering T* for Cu, with its lower melting point, is >0.4 even at a lower deposition temperature of 300ºC, and for Cr, T* is <0.4 even at a higher deposition temperature of 450ºC, the energy level for the present films is expected to fall within zone T, with energies on the order of 10's of eV. The CuCrA sample, deposited at a lower bias voltage, formed shorter grains compared to CuCrB, which was deposited at a higher voltage (Fig 5.13 & 5.14).

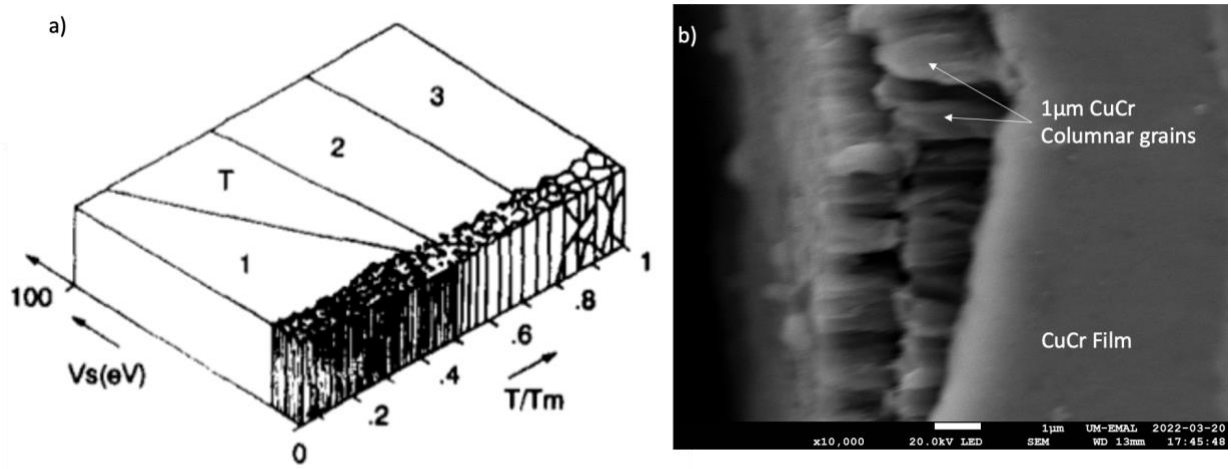

Figure 5.17 a) Structure zone diagram [3] b) Columnar grains obtained for CuCr films

CuCrC sample, predominantly composed of Cr, is also within zone T, resulting in lower hardness for Cr films. As discussed earlier, the CuCrA sample exhibits a finer-grained structure due to lower adatom diffusion at a lower temperature. XRD and TEM images indicate higher non-equilibrium compositions of Cr-Cu in CuCrA, leading to higher hardness. Simultaneously, these non-equilibrium compositions contribute to higher resistivity due to the presence of a larger number of impeding grain boundaries for electron motion. On the other hand, CuCrB displays

higher diffusion and longer grain structures, resulting in lower hardness and lower resistivity. It is also interesting that CuCrC with 98% Cr content has lower resistivity than CuCrA with 84% avg Cr content. This further validates the higher film density and lower grain boundary are for films deposited at higher pulsed bias voltages. The hardness of the CuCr films falls within the range produced by sputtering methods. For CuCrC, the hardness is comparable to pure Cr films produced with less ion bombardment [27,32].

5.5 Producing multilayer CuCr Coatings

PVD coatings offer the opportunity to produce multilayer films, which can enhance the performance of monolithic layers for various reasons, such as impeding dislocation movement and crack propagation. This assists in building thicker bulk coatings. In the case of VI applications, alternating layers of CuCr/pure Cu structures can help reduce bulk resistivity, thus improving VI performance. However, the high coefficient of thermal expansion (CTE) of Cu layers can lead to delamination at low CTE CuCr layers, thereby limiting the number of layers that can be deposited without causing bulk defects such as cracking. An initial assessment of the multilayer structure was attempted in this study. A multilayer sample was deposited using a composite target containing 65:35 wt% Cr:Cu ratio assembled on cathode 1 (the same target composition used for CuCr A, B, C samples) and a pure Cu target on cathode 2 of the setup. The sample was prepared by alternately depositing layers from cathode 1 and cathode 2 for a total of 9 runs (n=5 for CuCr and n=4 for Cu), with the deposition parameters listed in the table 5.1. Figure 5.18 presents the SEM and EDX images for CuCrD sample, which had a thickness of approximately 12µm. The average composition of the sample was found to be Cr:Cu 73:27 wt%. Individual CuCr layer had a thickness of around 3µm, while the Cu layer had a thickness of approximately 350nm.

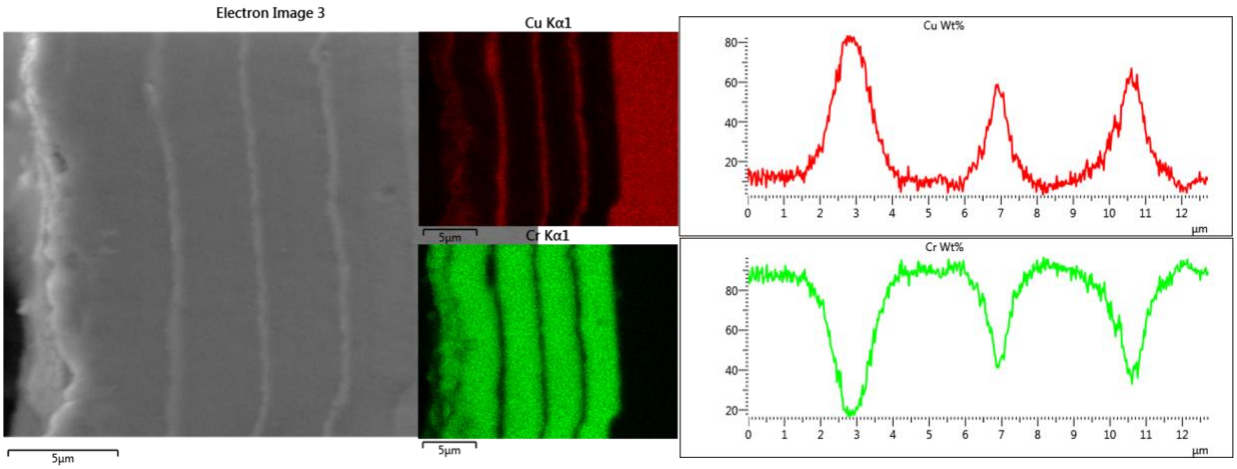

Figure 5.18 Multilayer CuCr/Cu film cross-section and EDX mapping data on the right

Surprisingly, the Cu sandwich-layers exhibited a composition with around 19% Cr, while the CuCr layers showed a deficit in Cu compared to the target composition. Although some Cu depletion from self-sputtering is expected in the top layers, a consistently low Cu composition is observed throughout all film layers, with the top CuCr layer having a Cu composition of 16% and the bottom layer close to the substrate having a Cu composition of 10%. This is suspected to be a result of uphill Cu diffusion from the CuCr layer to the pure Cu layer.

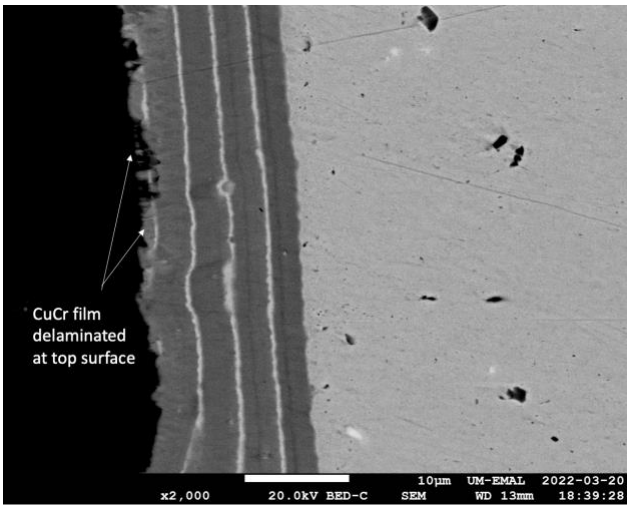

Figure 5.19 CuCr film delaminated at top surface

When the CuCr layer is deposited on top of the Cu layer, due to the high sputter yield of Cu (approximately 0.4 atoms/ion with Cu ion bombardment and approximately 0.6 atoms/ion of

Cr ion bombardment), some of the Cu surface layer up to around 2-3nm depth creates a significant number of vacancies and allowing some Cr ions to be implanted into the Cu sublayers. This promotes Cu diffusion from the underlying CuCr layer, creating a chemical gradient that further enhances Cu diffusion through the bulk of CuCr layer. At a pulsed bias of -200V, the substrate temperatures are expected to be around 400ºC, and the Cu diffusion can extend up to approximately 100nm. It is important to note that the 5th (top) CuCr layer is observed to be delaminated at the 4th Cu layer, as shown in Figure 5.19. This delamination is due to very high tensile residual stress, exceeding 4500 ± 400 MPa. The hardness and electrical resistivity of the CuCrD samples are marginally higher compared to CuCrB (deposited under similar bias voltage conditions), indicating no significant improvement in terms of bulk resistivity with the multilayers.

	Hardness (GPa)	Resistivity (ohm.mm)
CuCrB	7.6	$6.4x10^{-05}$
CuCrD	8.1	$7.0x10^{-05}$

Table 5.4 Comparison of multilayer CuCr film properties

5.6 Breakdown performance of CuCr films

The breakdown test setup detailed in the previous chapter (Chapter 2) was also used in this study. Bulk CuCr65 composite (same composition as the target material) was used as a reference to compare the performance of the CuCr thin films. Figure 5.20 illustrates the normal distribution and average breakdown strength measured for the CuCr films. CuCrB, CuCrC, and CuCrD exhibited similar or higher breakdown strength compared to the bulk CuCr65 sample. On the other hand, CuCrA had lower breakdown strength compared to the reference sample. Overall, the samples deposited at higher bias voltages exhibited improved breakdown performance. CuCrB displayed lower arc life compared to the reference sample, while CuCrC and CuCrD had comparable arc life to the reference. Whereas CuCrA demonstrated much higher arc life compared to the reference samples. In general, the trend of arc life matches the trend observed for electrical

resistivity, as also seen in cold spray samples. This implies that arc life tends to decrease for samples with lower electrical resistivity thin films just as in case of bulk composite samples.

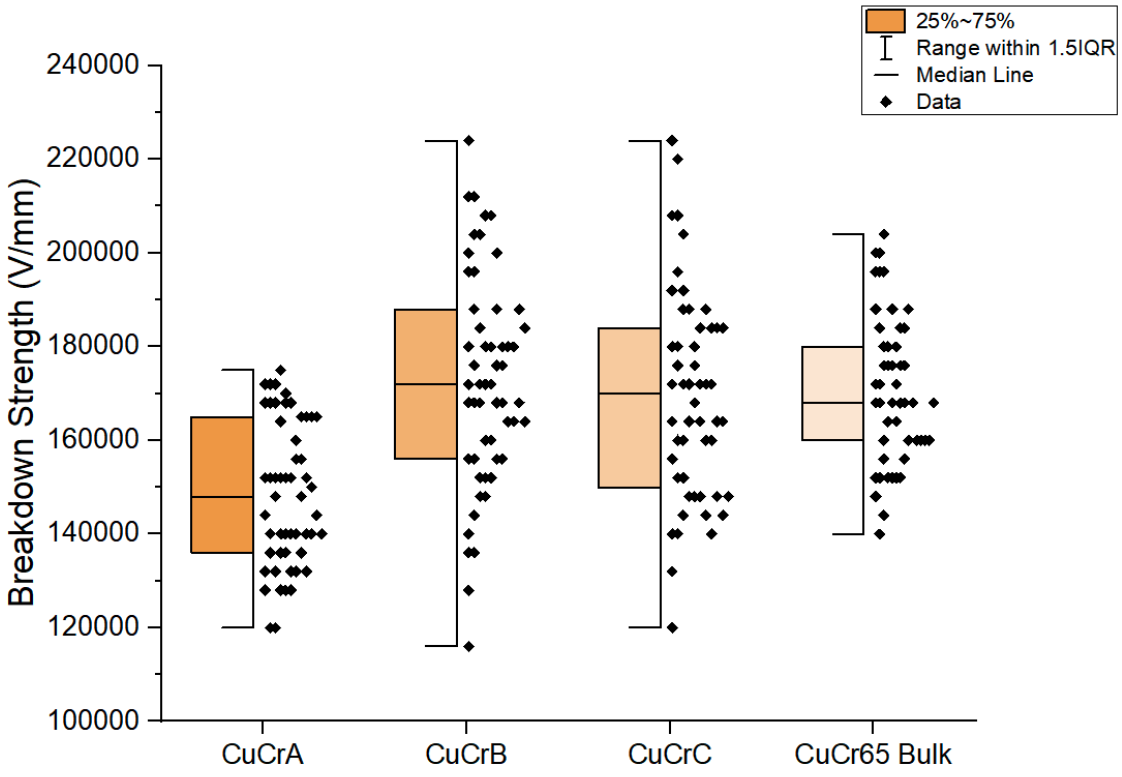

Figure 5.20 Breakdown strength of CuCr films

In Chapter 2, it was discussed that the breakdown strength can be influenced by the Cr content in bulk coatings and composites. In the case of CuCr materials, both Cu and Cr have closely matching work functions, slightly lower for Cr, making it a possible phase for arc initiation. When the circuit current exceeds a certain threshold value and the potential difference across the contacts reaches a minimum value, an arc is initiated between them. The erosion of the arc depends on the vapor pressure and thermal conductivity of the contact material, and the arc is always initiated from the metal vapor emitted by the contacts themselves. During a breakdown event, multiple cathode spots are formed on the surface, and move in retrograde motion repelling each other. The number of spots depends on the material. Each spot evolves into a new spot when the

spot threshold current is reached. Typically, the threshold current for Cu is around 100A/spot, while for Cr it is approximately 40A/spot. Therefore, for a similar breakdown current between contacts, a greater number of spots evolve on the Cr phase compared to the Cu phase. However, the erosion rate of Cu is higher at 120 (μgC^{-1}) compared to Cr at 40 (μgC^{-1}) [3]. This means that for each spot, more erosion occurs on the Cu phase compared to the Cr phase (fig 5.22). Therefore, if the Cr phase is dispersed within the Cu phase, the erosion will be reduced. Previous research has shown that the presence of Cr improves the breakdown strength of the electrodes. Further improvement is achieved by having two phases in nano-sized dispersions.

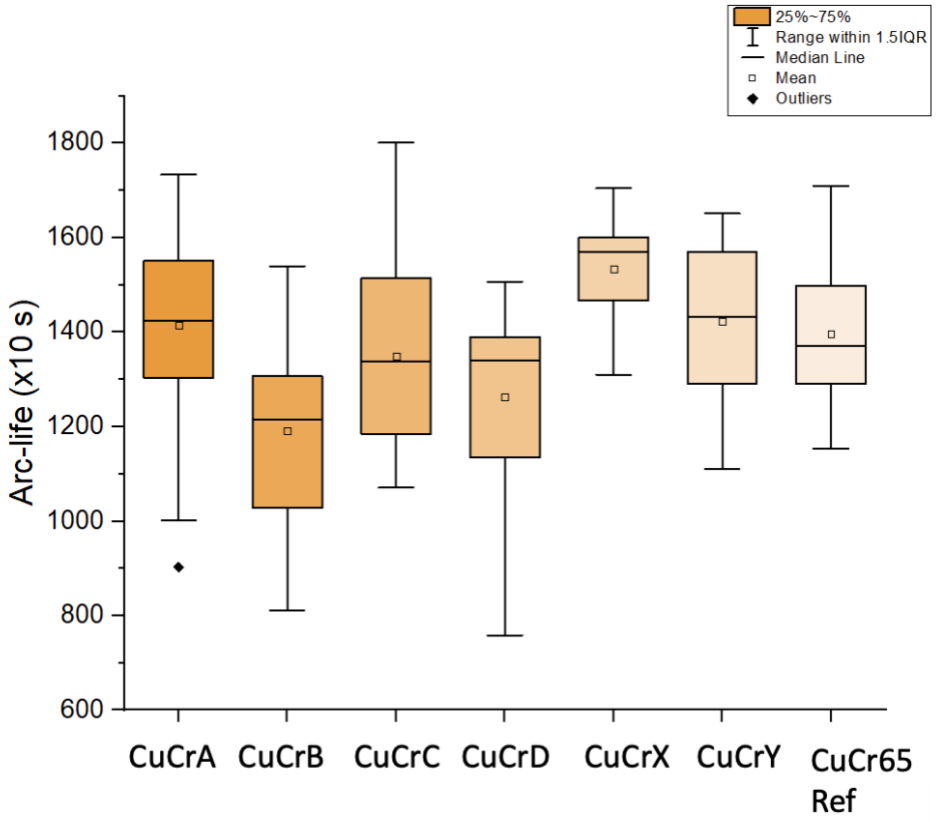

Figure 5.21 Average arc-life on CuCr films

The breakdown strength of CuCr thin films does not exhibit a strong correlation with the Cr content in the coatings, like bulk composites. For example, samples CuCrX with a composition of 70% Cr and 30% Cu, and CuCrA with a surface composition of 84% Cr and 16% Cu, displayed

similar breakdown strengths. Similarly, sample CuCrB with a composition of 75% Cr and 25% Cu, and CuCrC with a composition of 2% Cr and 98% Cu, also exhibited similar breakdown strengths. Similarly, higher Cr content CuCrY with 6%Cu and 94%Cr had comparable breakdown strength as CuCrX sample.

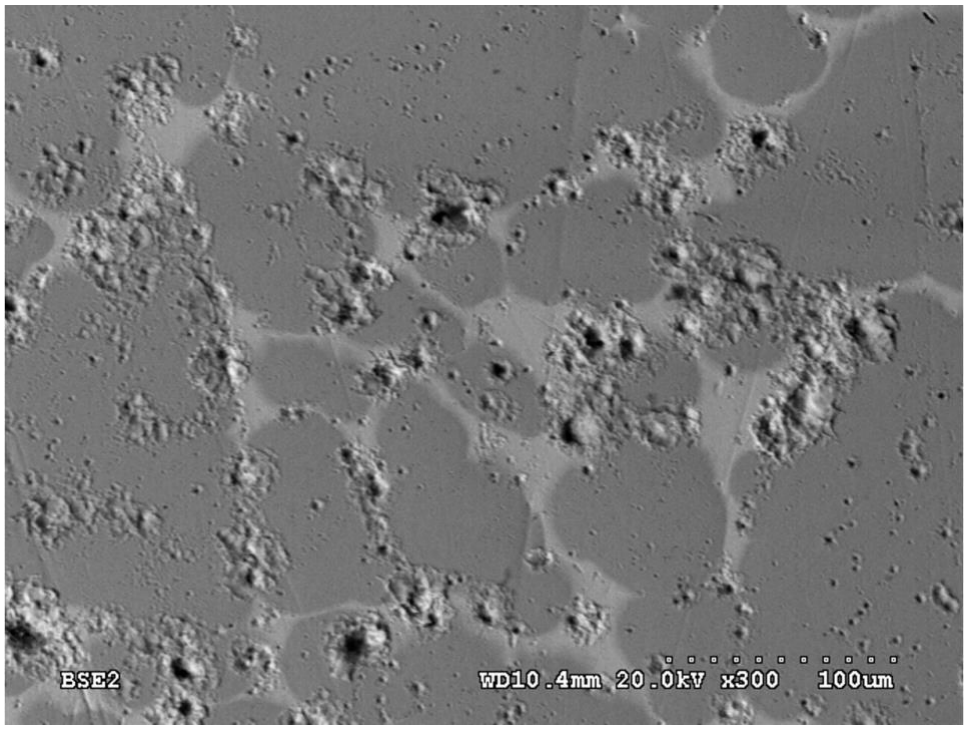

Figure 5.22 Image illustrating higher arc-erosion on Cu-matrix phase compared to Cr particulates

To understand this observation, let's revisit the Fowler-Nordheim equation discussed in Chapter 2. The predicts the current density at an electron emission site. The emission current density is influenced by the surface enhancement factor (ß) and the work function (Ø). The enhancement factor is affected by factors such as surface roughness, grain boundaries at the surface, adsorbed gases, surface porosity, and micro-particles. In the studied CuCr films, the surface roughness is comparable, and the contribution from macro-particles can be considered negligible since CuCrB with higher surface particles exhibited higher breakdown strength. Therefore, the contributing factors for the differences in breakdown strength are likely the grain

boundary area and film porosity. TEM images and material properties measured, reveal that CuCrA and CuCrX (-20V cont. DC) samples have smaller-sized grains compared to CuCrB (-200V pulsed DC), which is deposited with higher ion bombardment due to a higher substrate bias. The higher ion bombardment promotes greater adatom mobility, leading to the filling of surface vacancies and an increase in film density for CuCrB compared to CuCrA or CuCrX. In some studies, electron field emission sites have been found to preferentially arise from grain boundaries, independent of the surrounding surface morphology. Therefore, films formed with lower ion bombardment at a low bias voltage tend to have a larger grain boundary area and lower density, which increases electron emission and reduces the breakdown strength. The observed trend here is that increased ion bombardment enhances the breakdown strength.

The arc-life observed during the breakdown tests can be used as an indicator for comparing the arc-erosion performance of CuCr thin films. From fig. 5.22, it is evident that the erosion area of CuCrA and CuCrB is smaller than that of the reference sample. Figure 5.23, generated using ImageJ software, illustrates the wear profile plot, and it can be observed that the width of the wear zone for CuCrB is smaller compared to CuCrA, while the reference sample exhibits a wider erosion zone compared to the CuCr films. The differences in the arc erosion zone between the CuCr films and the reference bulk CuCr composite can be attributed to: 1) differences in the types of arcs on the two surfaces and 2) differences in bulk resistivity. The arcs on the reference sample appear more scattered compared to the arc zones on the CuCr films. This difference could be due to the distributed Cr phase present in the reference sample and the uniform bulk resistivity across the sample volume aids in movement of the arc across the sample surface. Whereas the arc zone in CuCr films is more constricted by the higher resistivity of the film compared to the reference due to nanosized structures within the surface of the film.

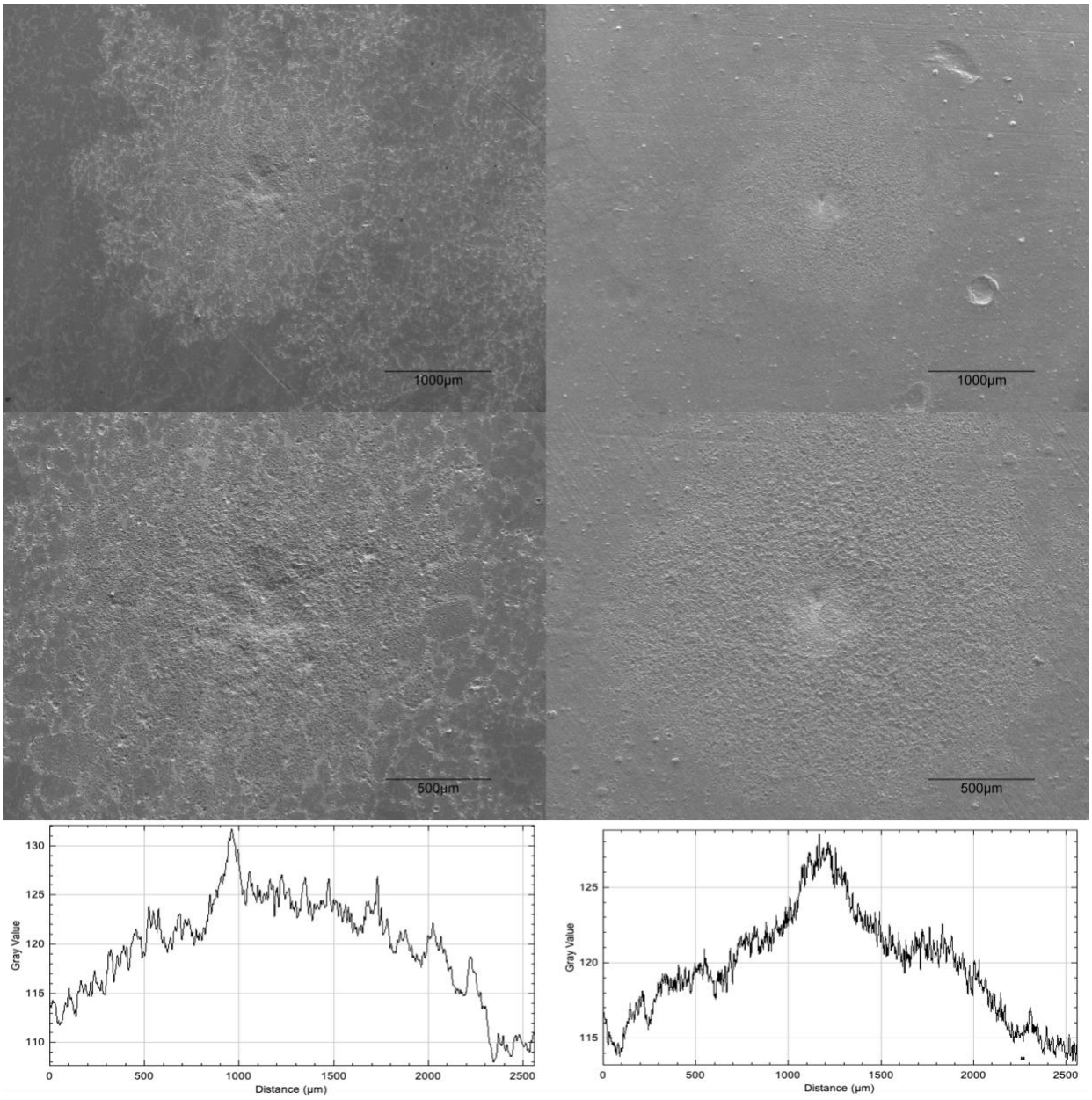

Figure 5.23 Arc-erosion profile on CuCr65 bulk composite on left vs CuCr film on the right

Also, the films are coated on a Cu substrate, and if the interfacial resistivity is low the thermal conductivity can be higher in the Z-direction (across the film thickness) compared to XY-surface direction, thereby restricting the arc motion across the surface. Obtaining reliable readings for erosion depth using a profilometer, as done for CuCr cold spray samples, was challenging for CuCr films. This is due to the restricted erosion zone being less than the thickness of the coating,

which means we needed to obtain reliable readings at scales less than 10µm, which is a limitation of the measurement device. The use of CT scan methods can be very helpful for accurately measuring the wear zones. Another approach could involve using current measurements from an oscilloscope to monitor the signal intensity, integrating it over the time period of the arc, and repeating this measurement for all arc cycles. This data could then be used to calculate wear in terms of mass loss per charge. However, such measurements would require repeated readings, which were not performed in this study as it was primarily focused on an initial assessment CuCr film breakdown voltage determination. To increase the confidence in breakdown strength established for the CuCr films the tests were repeated on CuCrB and CuCrX, the films with high Cu content and Fig 5.24 shows the repeat test data is consistently repeatable.

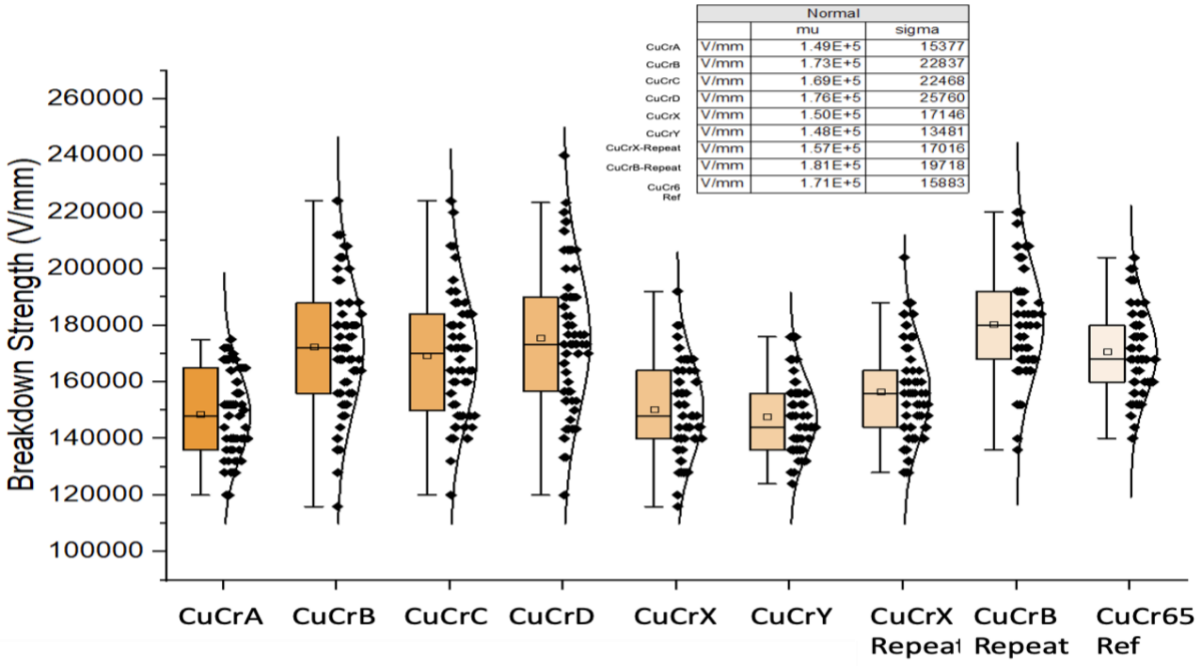

Figure 5.24 Comparison of breakdown performance of CuCr films

5.7 Conclusions

The primary objective of this study is to achieve nano-layered CuCr films, which was not obtainable by co-deposition technique To accomplish this, CuCr films were produced using a

composite CuCr target, and the effect of bias voltage was studied on the microstructure of CuCr films produced by single targets. Electrical resistivity and nano-hardness were measured, and breakdown performance was established.

The following conclusions are drawn from the current study:

- Continuous DC substrate bias at high voltages causes higher sputtering of Cu from the films. The highest Cu retention was observed at -20V bias and -200V pulsed bias voltages. Increasing continuous bias to -100V or pulsed bias to -300V increases Cu sputtering from the CuCr films, leading to low Cu content that can adversely affect the breakdown performance. The high Cu-sputter rates associated with high bias voltages contribute to compositional non-uniformity across the film.
- A bias voltage of -200V in pulse mode created a high droplet number density on the film surface, and increasing the duty cycle should be explored to mitigate this issue. Films deposited at lower voltages exhibit a nano-scale layered structure, which increases the hardness of the films but adversely affects the conductivity. Conversely, higher bias voltages increase conductivity but marginally lower the hardness. Multilayered CuCr/Cu coatings did not improve the electrical conductivity compared to bulk CuCr film deposited at the same deposition parameters.
- Increasing the continuous bias voltage to -100V transformed film stress from tensile to compressive, which was observed at -20V. However, using high pulsed bias voltages of -200V and -300V still showed tensile stresses but with lower magnitudes when compared to -20V contiuous bias. CuCr film properties are highly

influenced by film density, and microstructure. CuCr films tend to have nano-layered Cu-Cr structures that grow with an increase in ion bombardment.

- Breakdown strength and arc-life of CuCr coatings produced at high bias voltages were comparable to bulk CuCr composite. The Cr content in the films did not show as much effect on the breakdown performance as film density. The arc-life followed the electrical resistivity trend, with higher resistivity resulting in higher arc life on the sample surface, which can be undesirable for contact applications.

References

[1] Ali, M., Hamzah, E., Hamid, M.A., Hashim, A.H., 2023. Whether macro-droplets generate or develop in depositing hard coatings by cathodic arc evaporation technique. International Journal of Refractory Metals and Hard Materials 115, 106296. https://doi.org/10.1016/j.ijrmhm.2023.106296

[2] Allas, R.G., Knudson, A.R., Lambert, J.M., Treado, P.A., Reynolds, G.W., 1982. Self-ion sputtering yields for copper, nickel, and aluminum. Nuclear Instruments and Methods in Physics Research 194, 615–619. https://doi.org/10.1016/0029-554X(82)90592-4

[3] Anders, A., 2022. Cathodic Arcs.

[4] Anders, A., Andersson, J., Horwat, D., Ehiasarian, A., n.d. Physics of High Power Impulse Magnetron Sputtering.

[5] Ankit, K., Derby, B., Raghavan, R., Misra, A., Demkowicz, M.J., 2019. 3-D phase-field simulations of self-organized composite morphologies in physical vapor deposited phase-separating binary alloys. Journal of Applied Physics 126, 075306. https://doi.org/10.1063/1.5110410

[6] Askill, J., Tomlin, D.H., 1965. Self-diffusion in chromium. The Philosophical Magazine: A Journal of Theoretical Experimental and Applied Physics 11, 467–474. https://doi.org/10.1080/14786436508224234

[7] Baker, I., Liu(Lee Louis), L., Mandal, D., 1995. The effect of grain size on the stored energy of cold work as a function of strain for polycrystalline nickel. Scripta Metallurgica et Materialia 32, 167–171. https://doi.org/10.1016/S0956-716X(99)80031-4

[8] Baker, M.A., Kench, P.J., Joseph, M.C., Tsotsos, C., Leyland, A., Matthews, A., 2003. The nanostructure and mechanical properties of PVD CrCu (N) coatings. Surface and Coatings Technology 162, 222–227. https://doi.org/10.1016/S0257-8972(02)00571-6

[9] Boxman, R.L., Goldsmith, S., 1992. Macroparticle contamination in cathodic arc coatings: generation, transport and control. Surface and Coatings Technology 52, 39–50. https://doi.org/10.1016/0257-8972(92)90369-L

[10] Cathodic-Arc and Thermal-Evaporation Deposition – ScienceDirect https://www.sciencedirect.com/science/article/pii/B978008096532100409X

[11] Davidson, J.L., Kang, W.P., Subramanian, K., Wong, Y.M., 2008. Forms and behaviour of vacuum emission electronic devices comprising diamond or other carbon cold cathode emitters. Philosophical Transactions of the Royal Society A: Mathematical, Physical and Engineering Sciences 366, 281–293. https://doi.org/10.1098/rsta.2007.2154

[12] Diffusion of vanadium, chromium, and manganese in copper | SpringerLink https://link.springer.com/article/10.1007/bf02661758?utm_source=getftr&utm_medium=getftr&utm_campaign=getftr_pilot (accessed 7.4.23).

[13] Fessmann, J., Olbrich, W., Kampschulte, G., Ebberink, J., 1991. Cathodic arc deposition of TiN and Zr(C, N) at low substrate temperature using a pulsed bias voltage. Materials Science and Engineering: A, Second International Conference on Plasma Surface Engineering 140, 830–837. https://doi.org/10.1016/0921-5093(91)90521-N

[14] Ganji, R.S., Sai Karthik, P., Bhanu Sankara Rao, K., Rajulapati, K.V., 2017. Strengthening mechanisms in equiatomic ultrafine grained AlCoCrCuFeNi high-entropy alloy studied by micro- and nanoindentation methods. Acta Materialia 125, 58–68. https://doi.org/10.1016/j.actamat.2016.11.046

[15] Gudmundsson, Jon Tomas, Anders, A., Keudell, A. von, 2022. Foundations of physical vapor deposition with plasma assistance. Plasma Sources Sci. Technol. 31, 083001. https://doi.org/10.1088/1361-6595/ac7f53

[16] Gudmundsson, J. T., Fischer, J., Hinriksson, B.P., Rudolph, M., Lundin, D., 2022. Ionization region model of high power impulse magnetron sputtering of copper. Surface and Coatings Technology, Special Issue of Surface and Coatings Technology celebrating the pioneering research career of Professor Allan Matthews in the field of “Plasma-based Surface Engineering” 442, 128189. https://doi.org/10.1016/j.surfcoat.2022.128189

[17] Harniman, R., May, P.W., Fox, O.J.L., 2017. Direct observation of electron emission from CVD diamond grain boundaries by tunnelling atomic force microscopy independent of surface morphology. Diamond and Related Materials 80, 147–152. https://doi.org/10.1016/j.diamond.2017.09.009

[18] Harzer, T.P., Djaziri, S., Raghavan, R., Dehm, G., 2015. Nanostructure and mechanical behavior of metastable Cu–Cr thin films grown by molecular beam epitaxy. Acta Materialia 83, 318–332. https://doi.org/10.1016/j.actamat.2014.10.013

[19] Kai, L., Xiaojun, M., Dan, Q., Li, Y., Yu, M., Yajuan, P., Bo, Y., Yanhuai, L., Liucheng, H., Yanyan, F., Zhongxiao, S., 2021. Arc erosion resistance of CuCrMo films deposited via magnetron sputtering. Mater. Res. Express 8, 066402. https://doi.org/10.1088/2053-1591/ac0179

[20] Kuskov, K.V., Rogachev, A.S., Vadchenko, S.G., Shkodich, N.F., Rouvimov, S., Shchukin, A.S., Illarionova, E.V., Kudryashov, V.A., Mukasyan, A.S., 2018. Resistance of microcrystalline and nanocrystalline Cu/Cr pseudo-alloys to vacuum discharge. Journal of Alloys and Compounds 750, 811–818. https://doi.org/10.1016/j.jallcom.2018.04.049

[21] Layered structure enhances the hardness of Cu-48at.%Cr film prepared by co-sputtering deposition technique - ScienceDirect [WWW Document], n.d. URL https://www.sciencedirect.com/science/article/pii/S0042207X2100292X

[22] Li, X.G., Cao, L.F., Zhang, J.Y., Li, J., Zhao, J.T., Feng, X.B., Wang, Y.Q., Wu, K., Zhang, P., Liu, G., Sun, J., 2018. Tuning the microstructure and mechanical properties of magnetron sputtered

Cu-Cr thin films: The optimal Cr addition. Acta Materialia 151, 87–99. https://doi.org/10.1016/j.actamat.2018.03.044

[23] Lu, Y., Wang, C., Gao, Y., Shi, R., Liu, X., Wang, Y., 2012. Microstructure Map for Self-Organized Phase Separation during Film Deposition. Phys. Rev. Lett. 109, 086101. https://doi.org/10.1103/PhysRevLett.109.086101

[24] Lugscheider, E., Knotek, O., Löffler, F., Barimani, C., Guerreiro, S., Zimmermann, H., 1995. Deposition of arc TiAlN coatings with pulsed bias. Surface and Coatings Technology, International Conference on Metallurgical Coatings and Thin Films 76–77, 700–705. https://doi.org/10.1016/0257-8972(96)80009-0

[25] Ma, E., 2005. Alloys created between immiscible elements. Progress in Materials Science 50, 413–509. https://doi.org/10.1016/j.pmatsci.2004.07.001

[26] Mahan, J.E., 2000. Physical Vapor Deposition of Thin Films, Physical Vapor Deposition of Thin Films.

[27] Maier, K., 1977. Self-diffusion in copper at “low” temperatures. physica status solidi (a) 44, 567–576. https://doi.org/10.1002/pssa.2210440220

[28] Misra, A., Nastasi, M., 1999. Evolution of tensile residual stress in thin metal films during energetic particle deposition. Journal of Materials Research 14, 4466–4469. https://doi.org/10.1557/JMR.1999.0605

[29] Olbrich, W., Kampschulte, G., 1993. Additional ion bombardment in PVD processes generated by a superimposed pulse bias voltage. Surface and Coatings Technology 61, 262–267. https://doi.org/10.1016/0257-8972(93)90236-H

[30] Petrov, I., Adibi, F., Greene, J.E., Hultman, L., Sundgren, J. -E., 1993. Average energy deposited per atom: A universal parameter for describing ion-assisted film growth? Applied Physics Letters 63, 36–38. https://doi.org/10.1063/1.109742

[31] Ryabchikov, A.I., Ananin, P.S., Sivin, D.O., Dektyarev, S.V., Bumagina, A.I., Shevelev, A.E., Andriyashin, D.A., 2016. Influence of negative bias pulse parameters on accumulation of macroparticles on the substrate immersed in titanium vacuum arc plasma. Surface and Coatings Technology, The 19th International Conference on Surface Modification of Materials by Ion Beams [SMMIB2015] 306, 251–256. https://doi.org/10.1016/j.surfcoat.2016.06.026

[32] Salamania, J., Johnson, L.J.S., Schramm, I.C., Calamba, K.M., Boyd, R., Bakhit, B., Rogström, L., Odén, M., 2021. Influence of pulsed-substrate bias duty cycle on the microstructure and defects of cathodic arc-deposited Ti1-xAlxN coatings. Surface and Coatings Technology 419, 127295. https://doi.org/10.1016/j.surfcoat.2021.127295

[33] Swift, P.D., 1996. Macroparticles in films deposited by steered cathodic arc. J. Phys. D: Appl. Phys. 29, 2025. https://doi.org/10.1088/0022-3727/29/7/041

[34] Tai, C.N., Koh, E.S., Akari, K., 1990. MACROPARTICLES ON TiN FILMS PREPARED BY THE ARC ION PLATING PROCESS, in: Sartwell, B.D., Zemel, J.N., McGUIRE, G.E., Bresnock, F.N. (Eds.), Metallurgical Coatings and Thin Films 1990. Elsevier, pp. 324–335. https://doi.org/10.1016/B978-1-85166-813-7.50039-5

[35] Xie, T., Fu, L., Cao, X., Zhu, J., Yang, W., Li, D., Zhou, L., 2020. Self-assembled binary immiscible Cu-transition metal multilayers prepared by co-sputtering deposition. Thin Solid Films 705, 138037. https://doi.org/10.1016/j.tsf.2020.138037

[36] Zhang, Z., Guo, J., Dehm, G., Pippan, R., 2017. In-situ tracking the structural and chemical evolution of nanostructured CuCr alloys. Acta Materialia 138, 42–51. https://doi.org/10.1016/j.actamat.2017.07.039

[37] Farid Movassagh-Alanagh, Meisam Mahdavi, “Improving wear and corrosion resistance of AISI 304 stainless steel by a multilayered nanocomposite Ti/TiN/TiSiN coating”, Surfaces and Interfaces, Volume 18, 2020, 100428.

[38] B.D. Beake, V.M. Vishnyakov, A.J. Harris, “Relationship between mechanical properties of thin nitride-based films and their behavior in nano-scratch tests”, Tribology International, Volume 44, Issue 4, 2011, Pages 468-475.

[39] Andersen, H.H. and Bay, H.L., 1981. Sputtering by ion bombardment. ed. R. Berisch, Springer–verlag, Berlin Heidelberg New York, 145.

[40] J. F. Ziegler and J. Biersack, Monte Carlo code SRIM2006.02, downloadable from http://srim.org/,” 2006.

Chapter 6 Summary and Future Work on CuCr Coatings & Thin Films

In this study, successful production of CuCr coatings using Cold-Spray deposition and CuCr thin films via VAPD techniques was achieved. The CuCr coatings produced by Cold-Spray deposition demonstrated improved conductivity, comparable to bulk composites after annealing, leading to enhanced overall breakdown performance. However, the post-deposition annealing step in an inert atmosphere (to control surface oxides) adds an additional manufacturing step. This is against the intended purpose of the study, which is aimed at improving the efficiency by eliminating unwanted high temperature processing steps. To overcome this, an in-situ laser Cold-Spray deposition technique can be investigated. The addition of laser to Cold-Spray deposition has shown promise in providing annealing effects and improving deposition efficiencies. The additional energy supplied to the deforming material softens it and enhances the chances for Cr retention in the coatings. Another approach to enhance Cold-Spray CuCr coatings is by controlling the Cr size in the initial feedstock, to ensure that Cr particles do not lead Cu particles during deposition and create unwanted Cr-Cr interactions at the depositing fronts which reduce the Cr retention. Reduced Cr-Cr interaction can also be achieved by injecting Cr further down in the Cold-Spray nozzle near the exit to reduce its velocities, allowing them to stream with Cu particles which promotes Cr engulfment by other deforming Cu material without undesirable interactions. Currently, arc-erosion rates and chopping current data for Cold-Sprayed CuCr coatings are not determined by this study, and a complete functional test has not been performed which emulates tests by CuCr contact manufacturers. Investigating these aspects would further provide evidence

for performance improvements and durability of Cold-Sprayed CuCr coatings in vacuum interrupter technology.

The pressure-less infiltration technique employed for this study has been successfully demonstrated to produce high Cr content CuCr composite targets for CuCr deposition. This technique has been validated on a large scale using an industrial furnace, to produce high Cr content materials with additional elements like W. These composite materials, some of which are depicted in the images below, can be directly utilized as contact materials in Vacuum Interrupters (VI).

Figure 6.1 CuCr and CuCrW contact materials produced using developed pressure-less infiltration method

The existing literature on CuCr films deposited by the VAPD process is limited, and this study contributes valuable insights into the microstructural evolution and achievable properties through both co-deposition and single target deposition techniques. Co-deposition resulted in CuCr films, while single target deposition yielded nano-layered CuCr films. These methods achieved CuCr films up to 20μm in thickness and demonstrated comparable breakdown performance to bulk composites. However, a major challenge in developing CuCr films was achieving compositional

uniformity of Cu within the films. The high sputter-yield of Cu led to decreased Cu content in the coatings under unoptimized deposition conditions. To improve compositional uniformity without compromising film density, strategies such as implementing substrate temperature control or optimizing pulsed substrate bias power supply parameters to minimize temperature variations can be explored. The effect of deposition pressure can also be investigated to enhance the compositional uniformity of CuCr films. Depositing CuCr films at higher chamber pressures can lead to decreased ion energies because of increased neutral atom collisions.

Further investigations can focus on other cathode variations, such as CuCrW with varying W content, which have not been thoroughly explored yet. Even CuCr50 targets were developed but remain uninvestigated. Additionally, testing breakdown performance with films as both anode and cathode can be conducted to better assess breakdown performance.

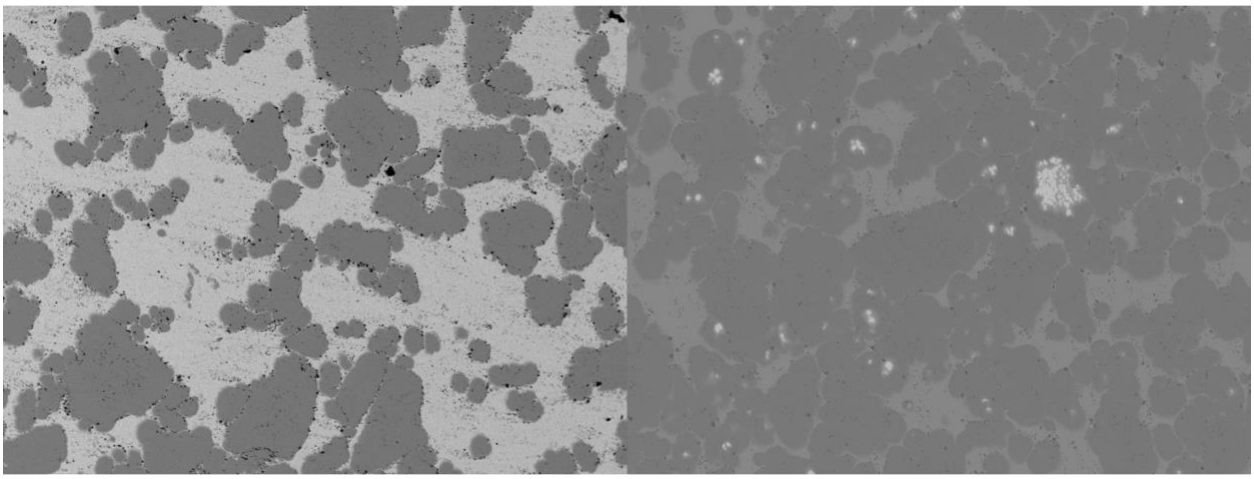

Figure 6.2 Microstructure of CuCr50 and CuCr60W5 cathodes developed for VAPD

Although multilayer structures did not significantly improve resistivity, the design of materials can be refined by incorporating a diffusion barrier layer, such as W, or increasing the thickness of Cu interlayer between CuCr/Cu layers. Alternately, combining a cold-sprayed base CuCr layer (predominantly Cu-rich with high conductivity) with a top CuCr layer from VAPD (Cr-rich to improve arc erosion/weld resistance) shows promise as an alternative coating. This

approach has the potential to enhance bulk conductivity and surface erosion properties of contacts, presenting a viable alternative for improved performance.

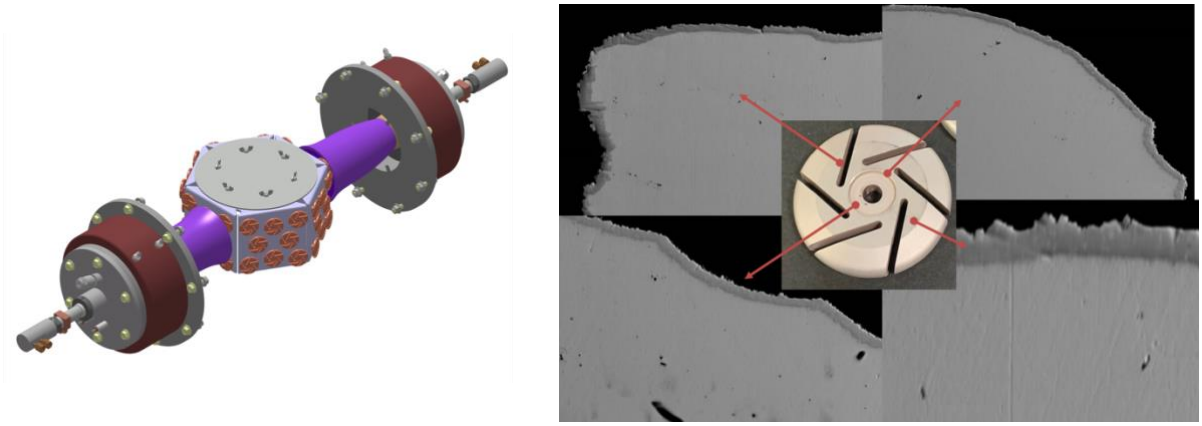

Figure 6.3 Setup designed and tested for producing CuCr films on Cu contacts

The current VAPD technique has been successfully scaled to produce 48 contacts/hour, as demonstrated in the figure below. To assess the conformality of films produced by this setup, CuCr films were deposited on machined Cu contacts, and their cross-sections were examined using SEM (Fig below). The results indicate excellent conformal CuCr coatings can be produced using VAPD, providing evidence that VAPD coatings can be applied after machining to enhance surface erosion behavior. This opens opportunities for further improvements in contact materials manufacturing technologies.

Present research study addresses few gaps in the field of coating technology and electrical contact applications. There is no prior literature on structure property evolution of CuCr films by VAPD. By studying the process-property evolution of CuCr films, this study has provided insights into the behavior of nanophase CuCr coatings, particularly in wear-resistant electrical contact applications. It was also demonstrated that the breakdown strength and arc-erosion resistance of the thin film coatings can be comparable to bulk CuCr composites. This understanding can have practical implications for improving the performance and durability of contact materials used in VI applications.

Furthermore, through this study the breakdown strength characteristics of cold-sprayed CuCr coatings is established, which have remained relatively unexplored. Through comprehensive process investigations of cold-spray and VAPD, this study introduces an innovative approach involving the deposition of CuCr bulk coatings with lower Cr content (upto25%) onto Cu electrodes, followed by the application of a conformal CuCr thin film having very high Cr content (fig 6.4). This dual-layer configuration of CuCr coatings offers the advantage of combining a high conductivity base layer with a top layer that exhibits superior arc-erosion resistance. Such material design holds significant promise for developing superior contact materials.

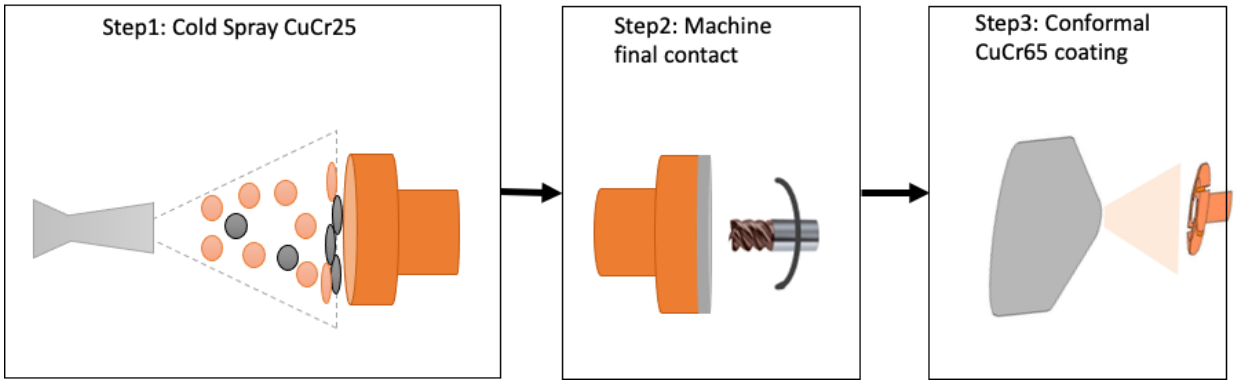

Figure 6.4 Novel 2-step CuCr deposition approach to produce highly conductive base layer with highly arc-erosion resistant top layer

This dissertation contributes to the scientific community through the following studies:

- Paper1: Microstructure evolution and vacuum breakdown performance of CuCr thin films produced at various substrate bias conditions

  In this paper the effect of ion bombardment energies on microstructure and electrical resistivity of high Cr content CuCr films is reported. The breakdown performance in terms of breakdown strength and arc-life is measured and compared to bulk CuCr composites.

- Paper2: Characterization of CuCr thin films produced by vacuum arc plasma deposition

In this paper the CuCr films produced by VAP-codeposition are investigate for compositional uniformity and the mechanism of Cu self-sputtering during deposition is explained using Mote Carlo code simulations.

- Paper3: Evaluation of cold-sprayed CuCr coatings as contact materials for VIs

  In this paper the breakdown strength of CuCr coatings is established and compared to bulk CuCr composites. The effect of annealing on properties of cold-sprayed CuCr coatings is also reported. Finally, it is demonstrated that annealed CuCr coatings have similar breakdown strength as bulk composites.

Overall, this study contributes to a comprehensive understanding of CuCr coatings and films, especially on various sub-micron and nanoscale CuCr microstructures that can be obtained, their corresponding properties, and breakdown performance. The findings hold promise for advancements in producing high-performance contact materials.

Study	Summary	Future Work
Cold-Sprayed CuCr Coatings • Effect of deposition pressures • Establishing breakdown performance	• CuCr coatings deposited at higher pressures can result in lower Cr retention • CuCr coatings deposited at lower pressures have higher porosity and weaker interface between Cu/Cr leading to higher electrical resistivity • Breakdown performance of as sprayed CuCr coatings is inferior to bulk composites • CuCr coatings annealed at 425ºC showed improved breakdown performance	• Investigation of CuCr coatings by laser-assisted cold spray system to perform in-situ annealing • Study using controlled Cr powder distributions to improve Cr retention in the coatings • Measuring the arc erosion rates of CuCr coatings and comparing to bulk composites
VAPD CuCr films by Co-Deposition • Effect of varying Cr/Cu Arc-current ratios is studied	• CuCr films deposited at high Cr/Cu arc currents showed significant Cu-sputtering from the deposited films • Films deposited at Cr/Cu <1 current ratio had a 1:1 Cu:Cr wt% composition • CuCr films exhibited a layered structure in sub-micron scale and all co-deposited films exhibited tensile residual stresses	• Effect of bias voltage on films produced at lower Cr/Cu arc-current ratios needs to be investigated • Electrical properties and breakdown performance has not been studied
VAPD CuCr films by single composite target • Microstructure evolution with different biasing conditions studied • Breakdown performance is established	• CuCr films produced at low bias voltages have higher Cu retention & a loss of ~5% Cu when compared to target composition • At high continuous DC bias voltage increases Cu self-sputtering due ASH • CuCr films deposited at low DC bias voltage produce nano-scale fibrous grains with a partial layered structure and exhibit higher hardness • Using pulsed DC bias voltage transforms the fibrous grains to longer columnar grains and improves electrical conductivity • Breakdown strength & of CuCr films are comparable to bulk composites • Erosion profile on CuCr films is more constricted compared to scattered profile on bulk composites	• Investigation of CuCr films produced by lower Cr content targets • Effect of substrate temperature control on compositional uniformity of CuCr films • Effect of chamber pressure on microstructure and compositional uniformity • Erosion rates of CuCr films needs to be established • Improving multi-layered structures by using a diffusion barrier layers to improve bulk resistivity of the samples

Table 6.1 Summary of preset research study